KINEMATICS STUDY OF M81 AND M82 GALAXIES

Dissertation
zur
Erlangung des Doktorgrades (Dr. rer. nat.)
der
Mathematisch-Naturwissenschaftlichen Fakultät
der
Rheinischen Friedrich-Wilhelms-Universität Bonn

vorgelegt von

Naftali Kagiri Kimani
aus
Kenya

Bonn, 2016

Dieser Forschungsbericht wurde als Dissertation von der Mathematisch-Naturwissenschaftlichen Fakultät der Universität Bonn angenommen und ist auf dem Hochschulschriftenserver der ULB Bonn http://hss.ulb.uni-bonn.de/diss_online elektronisch publiziert.

1. Gutachter: Prof. Dr. Karl M. Menten
2. Gutachter: Prof. Dr. Pavel Kroupa

Tag der Promotion: 22.11.2016
Erscheinungsjahr: 2016

Abstract

The measurement of proper motion combined with the radial velocities, is an important tool for our understanding of the dynamics and evolution of galaxies in a group environment. One of the nearest group is the M 81 group at a distance of ∼3.63±0.34 Mpc (Freedman et al., 1994). It is a fascinating interacting galaxy system consisting of the galaxies M 81, M 82 and NGC 3077. In the first part of this work, we present the proper motions of M 81 and M 82 galaxies, derived from Very Long Baseline Interferometry (VLBI) radio observations. The observations were conducted in three epochs between 2007 and 2009 at X- (8.4 GHz) and U-band (15.3 GHz), and four epochs between 2007 and 2015 at K-band (22.2 GHz). On the one hand, the proper motion of M 81 relative to Milky Way was derived from background quasars (0945+6924, 0948+6848, 1004+6936). This was done by fitting a rectilinear motion to the position offsets of the quasars. The positions offsets of quasar 0948+6848 were found to be contaminated from its jet motion. We averaged the observed proper motion of the other two quasars to obtain the proper motion relative to the Sun of M 81 as $\mu_\alpha = 0 \pm 5.7\,\mu\mathrm{as\,yr}^{-1}$ and $\mu_\delta = -22.5 \pm 2.1\,\mu\mathrm{as\,yr}^{-1}$ at 22.2 GHz. Correcting for the peculiar motion of the Sun and the rotation of the Milky Way, this measurement yields a proper motion relative to the Milky Way of $10.2\pm5.7\,\mu\mathrm{as\,yr}^{-1}$ ($\sim179\pm100\,\mathrm{km\,s}^{-1}$) towards the East and $-24.5\pm2.2\,\mu\mathrm{as\,yr}^{-1}$ ($\sim-429\pm39\,\mathrm{km\,s}^{-1}$) towards the North. With the total radial motion of M 81 towards the Milky Way reported as $73\pm6\,\mathrm{km\,s}^{-1}$, we derive the total space velocity of M 81 relative to the MW as $471\pm108\,\mathrm{km\,s}^{-1}$. On the other hand, the proper motion of M 82 is derived from observations of three H_2O masers located at opposite sides of its dynamic center. After correcting for the internal rotation of M 82, the average observed proper motion of the three maser features yields a proper motion relative to M81 of $\mu_\alpha = 8.3\pm5.5\,\mu\mathrm{as\,yr}^{-1}$ ($143\pm95\,\mathrm{km\,s}^{-1}$) towards the East and $\mu_\delta = 10.6\pm4.3\,\mu\mathrm{as\,yr}^{-1}$($182\pm74\,\mathrm{km\,s}^{-1}$) towards the North. With a derived radial motion of $237\pm6\,\mathrm{km\,s}^{-1}$ towards M81, we obtain its total space velocity to be $331\pm120\,\mathrm{km\,s}^{-1}$ relative to M 81 galaxy. Moreover, with a separation distance between the centers being 38 kpc, M 82 is embedded in the dark matter halo of M 81, and can be considered bound. We therefore derive a lower limit of the mass of M 81 to be $(4.8\pm0.6)\times10^{11}\mathrm{M}_\odot$.

In the second epoch of the observations of the water masers in M 82, a bright new radio source was discovered (Brunthaler et al., 2009a), which turned out to be a new supernova. This led to a follow up program with the Very Large Array (VLA) and VLBI, which represents the second part of this thesis. We fit two models to the data, a simple power-law, $S \propto t^{\beta}$, and a simplified Weiler model, yielding decline indices, β, of $-1.22{\pm}0.07$ (days 100 –1500) and $-1.41{\pm}0.02$ (days 76–2167), respectively. The late time radio light curve evolution shows flux-density flares at $\sim$970 and $\sim$1400 days which are a factor of $\sim$2 and $\sim$4 higher than the expected flux, respectively. We derive the spectral index, α, $S_{\nu} \propto \nu^{\alpha}$, for frequencies 1.4 to 43 GHz for SN 2008iz during the period from $\sim$430 to 2167 days after the supernova explosion. The value of α shows no signs of evolution and it remains steep (≈ -1) throughout the period, unlike that of the well-studied SN 1993J which started flattening at $\sim$day 970. From the 4.8 and 8.4 GHz VLBI images, the supernova expansion is seen to start with a shell like structure that gets more and more asymmetric, then breaks up in the later epochs with bright structures dominating the southern part of the ring. This structural evolution differs significantly from that of SN 1993J which had remained circularly symmetric over 4000 days after the explosion. The VLBI 4.8 and 8.4 GHz images are used to derive a deceleration index, m, for SN 2008iz, of $0.86{\pm}0.02$, and the average expansion velocity between days 73 and 1400 as $(12.1{\pm}0.2){\times}10^{3}\,\mathrm{km\,s^{-1}}$. From the energy equipartition between magnetic fields and particles, we estimate the minimum total energy in relativistic particles and the magnetic fields during the supernova expansion and also find the magnetic field amplification factor for SN 2008iz to be in the range of 55 to 400.

Contents

List of Figures

List of Tables

1. Introduction

The main intent of this thesis is to study extragalactic proper motions, in particular the motions of the M 81/M 82 interacting galaxy system. It forms part of a broader effort that is aimed at measuring the 3-dimensional velocities of galaxies in the Local Group and in the nearby groups out to the Virgo Cluster. The first successful microarcsecond proper motion measurements of galaxies in the Local Group was conducted on M 33 and IC 10 (Brunthaler et al., 2005b, 2007). Being a success, the next target was the nearest galaxy group (M 81 group). Therefore, the results of this work is the first-ever proper motion measurement of galaxies outside of the Local Group. Such proper motion measurements besides being important for our understanding of the dynamics and evolution of galaxies in a group environment, they form a necessary step towards a better kinematics model of the local volume.

The growing interest in interacting galaxy systems is motivated by multi-wavelength galaxy surveys (e.g. SDSS, FIRST, NVSS, COSMOS, GOODS, VVDS) that have established that galaxies are not isolated objects, but rather found in groups or clusters. This unveils a striking connection between galaxy formation and large scale structures formation topics. Galaxy interaction in a group environment allows the hierarchical growth in mass of a massive galaxy by accretion of less massive galaxies, a process often referred to as galactic cannibalism. This cosmic cannibalism results from the in-falling of less massive galaxies into the gravitational potential of the more massive galaxy, experiencing strong tidal disruptions. This results in either total destruction of the smaller galaxies, or if they survive, tidal arms and bridges are formed that provide future evidence to the interaction. This implies that by determining the morphological structure and kinematic information of an interacting system, we can derive crucial information about the interaction scenario, which is key in understanding galaxy formation and evolution.

The interest in galaxy interactions, coupled with the recent advances in computing power, have made numerical simulation a powerful tool to investigate the formation and evolution of galaxies (Steinmetz, 1996). A direct way to obtain the set of initial parameters to the model would be through multiple observations of the system at different times and stages of interaction. However, given the enormous time scales involved in galactic interactions, this approach is completely unfeasible. Therefore, the numerical simulations are faced with the challenge of getting a set of right initial conditions as the inputs to the model and the right interaction time that results in the current observed configuration. The basic input parameters to an N-body galaxy interaction model include: the distances between the galaxy and its companions, the radial velocity, the transverse velocities (proper motions), the inclination angles, the position angles, the total masses of the galaxies and the total time of interaction (e.g. Yun, 1999 and Gomez et al., 2004). From this set of input parameters, only the line-of-sight velocities, position angle and the inclination angle are often known to a high precision. This leaves statistical approaches as the only way to constrain the rest of the input parameters.

For instance, the accuracy of the distances in the line-of-sight between the galaxy and its companions in an interacting system, is dependent on the accuracy of the distance from us to those galaxies. Currently, the calibration of most standard candles used for extragalactic distances, are tied in one way or another to the distance of the Large Magellanic Cloud (LMC) (e.g., Freedman 2000, Mould et al. 2000). However, the distance to LMC has been very hard to estimate due to unreliability of distance estimators such as Cepheids and RR Lyrae, because they suffer from uncertainties in extinction and metallicity, both of which are difficult to determine accurately for extragalactic systems. Fortunately, the distance to LMC has finally been precisely determined from the observation of 8 eclipsing binary systems to an accuracy of 2.2% as 49.97 ± 0.19(statistical) ± 1.11(systematic) kiloparsecs (Pietrzyński et al., 2013).

The total mass of galaxies and their associated dark matter halos are equally poorly known. The challenge in estimating a group's gravitational potential persists because usually only radial velocities of its members are known. In an effort to circumvent this challenge, Kulessa and Lynden-Bell (1992) devised a maximum likelihood method to derive galaxy mass where only the line-of-sight velocities are required. Using this technique, they determined the Milky Way galaxy's mass. The technique is however based on some serious assumptions, which include orbital eccentricities and equipartition. Given the uncertainties introduced by these assumptions, it is evident that the most reliable way of deriving masses is by using orbits, which requires the knowledge of three-dimensional velocity vectors, obtained from proper motion measurements. The importance of full space motions has been demonstrated by Wilkinson and Evans (1999). They have shown that the use of proper motions, in conjunction with the line-of-sight velocities of six objects, yields an improved mass estimate of the Milky Way.

1.1. Extragalactic proper motion

The process of measuring the proper motion is difficult and time consuming, but astronomers have been trying it for almost a century. Amongst the initial attempts to measure proper motion was van Maanen in 1923, who made claim to have measured the angular rotation motion as $20\pm1\,\mathrm{mas\,yr^{-1}}$ for the Triangulum Galaxy (M 33) using optical photographic plates separated by 12 years. This was later proven wrong by Hubble through the discovery of Cepheids in M 33 that reveal large distances (about 263 kpc, Hubble, 1926). The distance estimate (although 3 times lower than today's number), meant that the detection of proper motion was beyond the capabilities of optical instruments for such distances. About 80 years after van Maanen's claim, thanks to the developments in the astrometric VLBI technique and the discovery of water masers on opposite sides of M 33's nucleus, Brunthaler and his collaborators finally obtained accurate values for the proper motion and angular rotation of M 33 (Brunthaler et al., 2005a). From their rotation model, the angular rotation motion is estimated to be $-18.5\pm6\,\mu\mathrm{as\,yr^{-1}}$ in right ascension and $-21.6\pm6\,\mu\mathrm{as\,yr^{-1}}$ in declination, while the absolute proper motion is $29.9\pm2\,\mu\mathrm{as\,y^{-1}}$.

Other examples of derived proper motions from photographic plates include the work of Jones et al. (1994) who made the claim to measure the proper motion of LMC as $1.2\pm0.28\,\mathrm{mas\,yr^{-1}}$ from comparing photographic plates over a timespan of 14 years. Schweitzer et al. (1995) also claimed a proper motion of $0.56\pm0.25\,\mathrm{mas\,yr^{-1}}$ for the Sculptor dwarf spheroidal galaxy from 26 plates spanning a time of 53 years. Scholz and Irwin (1994) made a claim of measuring the proper motion of dwarf spheroidal galaxies in Draco and Ursa Minor using plates that spread about 35 years and reported a $1.28\pm0.8\,\mathrm{mas\,yr^{-1}}$ for Ursa Minor dSph and $1.34\pm\,0.5\,\mathrm{mas\,yr^{-1}}$ for Draco dSph.

In recent years, especially due to the high angular resolution and stability of the Hubble Space Telescope (HST) (van der Marel et al., 2014) and other ground based optical telescopes, proper motions have now been reliably measured for a number of galaxies in the Local group i.e. the LMC (Kallivayalil et al., 2006, Pedreros et al., 2006), the SMC (Kallivayalil et al., 2006) the Sculptor dwarf spheroidal galaxy (dShp) (Piatek et al., 2006) the Canis Major dwarf galaxy (Dinescu et al., 2005a), the Ursa Minor dSph (Piatek et al., 2005), the Sagittarius dSph (Dinescu et al., 2005b), the Fornax dSph (Piatek et al., 2002, Dinescu et al., 2004), and the Carina dSph (Piatek et al., 2003).

On the other hand, the expected proper motion for galaxies within the Local group and neighboring groups, ranging from $1\,\mathrm{mas\,yr^{-1}}$ to $20\,\mu\mathrm{as\,yr^{-1}}$, are detectable with the VLBI using phase-referencing technique (Brunthaler et al., 2005b). With the accuracy obtained with the

VLBI, one could in principle measure very accurate proper motions for most of the neighboring members within less than a decade. For instance, this technique has been used to measure the proper motion of Sgr A* with respect to extragalactic radio sources over a span of 8 years, yielding a proper motion of 6.37±0.02 mas yr^{-1} at a distance of 8.0±0.5 kpc, which translates to 241±15 km s^{-1} (Reid and Brunthaler, 2005). It has also been used in the observations of two water masers on opposite sides of Andromeda's satellite M 33, resulting in the determination of its geometric distance as 730± 168 kpc, and its total velocity as 190±59 km s^{-1} relative to the Milky Way (Brunthaler et al., 2005b). The proper motion of IC 10 was also measured using the position of water masers relative to two-background quasars over 4.3 years. This resulted to a motion of $-39\pm9\,\mu$as yr^{-1} towards the east and $31\pm8\,\mu$as yr^{-1} towards north at a distance of 660±66 kpc, which correspond to a space velocity of 215±42 km s^{-1} relative to Milky Way (Brunthaler et al., 2007). For the edge-on galaxy NGC 4258, the VLBI measurements of water masers spanning over three years are used to determine its geometric distance of 7.3±0.3 Mpc (Herrnstein et al., 1997). A major challenge of the VLBI technique is to find appropriate radio sources, such as compact radio cores or strong maser emissions for a given galaxy.

1.2. M 81 Group.

The M 81 group at a distance of ≈3.63±0.34 Mpc (Freedman et al., 1994) and a mass estimate of $(1.03\pm0.17)\times10^{12}\,\mathrm{M}_{\odot}$ (Karachentsev and Kashibadze, 2006) is one of the nearest galaxy group. It features a fascinating interacting galaxy system comprising M 81, M 82 and NGC 3077. The observations of the 21 cm line of atomic hydrogen (HI) with the Very Large Array have resulted in a very well defined interaction scenario (see Figure 1.2.1, Yun et al., 1994). Its biggest galaxy, M 81, sits in the core of the group, together with its two nearby companions M 82 (in the upper part of the image in Figure 1.2.1) and NGC 3077 (in the lower-right part of the image in Figure 1.2.1). A more distant member NGC 2976 also show evidence of tidal interaction within the group (Appleton et al., 1981).

Due to the proximity of this group, multi-wavelength observations (e.g. Sollima et al., 2010, Mayya and Carrasco, 2009, de Mello et al., 2008) and numerical simulations (e.g. Sofue, 1998, Yun, 1999, Gomez et al., 2004) have lead to a comprehensive understanding of its dynamics and provided crucial information on the consequences of tidal interactions in a group environment. Based on the modeling of the M 81-M 82-NGC 3077 interaction, Sofue (1998) postulates that M82 was a larger and more massive spiral galaxy, containing HI gas in the outer disk and dense molecular gas in the central region. During the close encounter, M 82 penetrated the disk of M 81 and as a result, the outer disk of M 82 was tidally truncated, while the bulge and nuclear disk have survived the tidal disruption. The truncated disk is believed to have provided the HI envelope, tidal tails and bridges in the M 81-M 82 system. The central gas disk of M 82 was dense enough to strip the gas disk of M 81 away by ram pressure, which accumulated in the center of M 82. This has caused the high-density molecular disk, a starburst, and the dark matter halo loss in M 82. In contrast, M 81 evolved into a galaxy that contains little gas in the center.

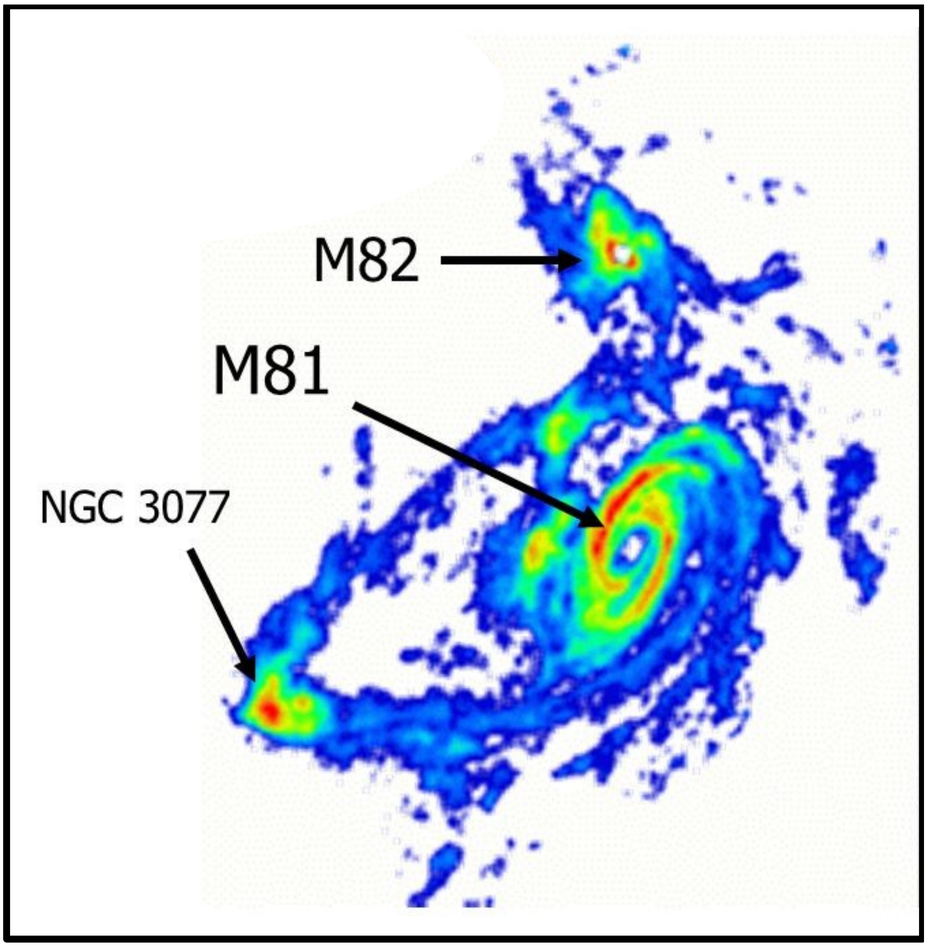

Figure 1.2.1.: The 21 cm HI line emission of the interacting galaxies M 81 (center), M 82 (top) and NGC 3077 (bottom right) in the M 81 group. The group contains remnants of tidal bridges connecting the three galaxies visible in the HI line. (Image courtesy of M. Yun, NRAO)

One of the key parameters that has to be known, for an accurate modeling of the history and evolution of the M 81 group, is their present spatial velocity vectors. If these were known, they could be used as initial conditions in the calculations of reconstruction and prediction of their past and future motion histories. Additionally, the most reliable way of deriving masses is using orbits, which require the knowledge of three-dimensional velocity vectors. The direct way to find the spatial velocity is to determine the proper motion of the these galaxies through observations.

For successful astrometric VLBI phase-referencing, we require either a compact extragalactic radio source or strong maser emission in the target source and, additionally, compact extragalactic radio sources serving as ideal reference frame (see section 2.3.1). M 81 is known to harbour an extremely compact radio source at its nucleus (M 81*), measuring 0.18×0.07 mas at 22 GHz (Bietenholz et al., 1996), with a mean flux of 127 mJy at 8.4 GHz (Bietenholz et al., 2000). M 82 is known to host several strong water maser sources, within a range of 70 to 363 $\mathrm{km\,s^{-1}}$ (Hagiwara, 2007, Baudry et al., 1994, Henkel et al., 1984) that have persisted for over three decades. However, NGC 3077 does not host any known maser emission, nor a compact radio source at its nucleus (Baudry et al., 1994). This disqualifies NGC 3077 as a candidate for the VLBI phase-referencing experiment. This work therefore, focuses on M 81 and M 82, which are the most suitable candidate for our VLBI phase-referencing observations.

1.3. Supernova SN 2008iz

The first three epochs of the M 81-M 82 proper motion observations, were between 2007 and 2009 at 8.4, 15.3 and 22.2 GHz. The VLBI network used comprised the VLBA, the Green Bank 100 m telescope, the Effelsberg 100 m telescope, and the phased[1] 27 VLA antennas. In the course of the observations a bright radio transient object (11 mJy) was observed at 22 GHz in M 82's central region from the VLA observations of 2009 April 8 by sheer chance, while the water masers were monitored in that region (Brunthaler et al., 2009a). The reported location of the radio transient source was given as R. A = $9^{\mathrm{h}}55^{\mathrm{m}}51^{\mathrm{s}}.55$, Dec. = $+69^{\circ}40'45''.8$ (J2000), which is $2.5''$ ($\sim$43 pc) south west of the photometric center of M 82 based on the 2.2 μm infrared emission peak (Weiß et al., 2001). Looking at the earlier observations, the same source was found to have brightened to a flux density of 90 mJy on 2008 May 03, and 104 mJy on 2008 March 24. Going back in time, the VLA observation on 2007 October 29 did not show the bright radio source. However, in the VLBA sub-milliarcsec resolution images made from data taken on 2008 May 3 and 2009 April 8 at 22 GHz, the same radio source was identified.

---

[1] Phasing means aligning the received signals from antennas in the array, which ensure the signal is in phase and can be added constructively, thereby increasing the sensitivity and the field of view.

It exhibited a ring-like structure, indicative of a shock wave, plunging through the interstellar medium with an expansion velocity of roughly 23000 km s^{-1} (see Fig. 1.3.1; Brunthaler et al., 2010). These results confirm the supernova nature of this source which was assigned the name SN 2008iz.

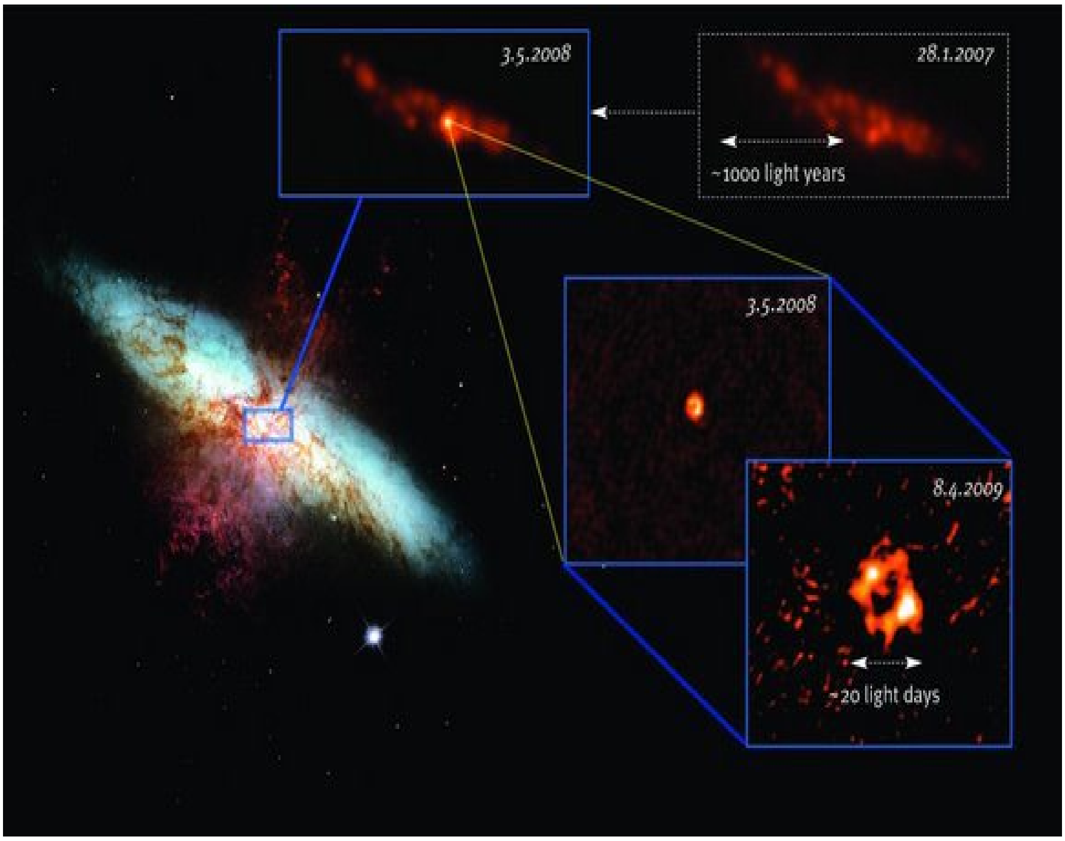

Figure 1.3.1.: SN 2008iz in the M 82 galaxy: A Hubble Space Telescope image (left) of M 82 shows hydrogen gas (red) breaking out from the central starburst (box), a region of intense star formation. A 2008 May VLA image of the star-burst region (top left) clearly shows the supernova (SN 2008iz), which exploded in 2008 February. The two high-resolution VLBA images (lower right) show an expanding shell at the scale of a few light days and proves that the transient source, was the result of a supernova. (Image coutersy of A. Brunthaler, MPIfR)

The presence of the supernova was also confirmed from the very well sampled data obtained with the Urumqi telescope at 5 GHz (see Fig. 1.3.2). At the time of the detection of SN 2008iz, the Urumqi telescope was monitoring Intra-Day Variable (IDV) sources, with an occasional observation of M82 as one of the amplitude calibrators (Marchili et al., 2010). The observations with MERLIN at 5 GHz (Muxlow et al., 2009, Beswick et al., 2009) also confirmed the presence of the supernova. Endeavors to make detections in other astronomical windows were not successful. For instance, there are no detections in visible light and X-Ray (Brunthaler et al., 2009b). Varenius et al. (2015) also report the LOFAR non-detection at 154 MHz. However, Mattila et al. (2013) reported a detection of a near-IR counterpart for SN 2008iz at ~480 days after the explosion. These non-detection indicate that the supernova must have exploded behind a large dusty molecular cloud along the line-of-sight.

From the VLBA measured expansion rate and extrapolating backward in time, the explosion date of SN 2008iz is estimated to have been around late January 2008 (Brunthaler et al., 2009b). This explosion date was also confirmed from the Urumqi telescope observations to be 2008 February 18±6 days (Marchili et al., 2010). Soon after the discovery and confirmation of SN 2008iz, a monitoring campaign was started with the VLA at 1.4, 4.8, 8.4, 22 and 43 GHz and also VLBA telescopes at 1.4, 4.8 and 8.4 GHz to trace its radio evolution. In the second part of this thesis, I will describe the use of VLA and VLBA data to study the evolution and the environment around SN 2008iz as the shock wave expansion continues.

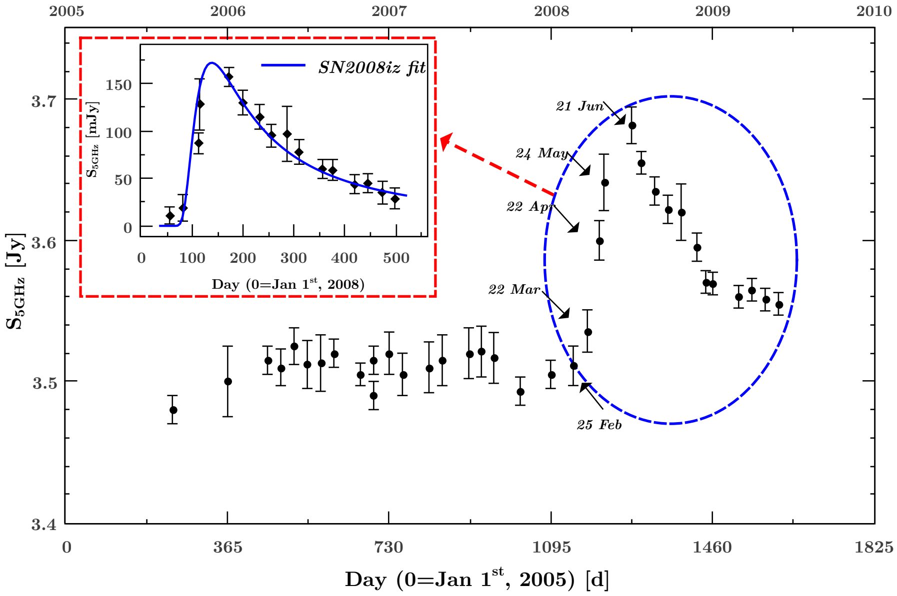

Figure 1.3.2.: 5 GHz variability curve of M 82 from Urumqi observations obtained between August 2005 and May 2009. The radio emission is nearly constant until February 2008 after which the flux density increase steeply coinciding with the expected explosion date of SN 2008iz. The inset shows the light curve fit to the supernova with the data extracted from the M 82 variability curve by subtracting the average contribution of diffuse emission in M 82 of 3.51 Jy. (Data courtesy of Marchili et al., 2010).

1.4. Aim and structure of the Dissertation

The aims of the study are:

1. To obtain the proper motion of M 81 relative to Milky Way galaxy, using the background quasars 0945+6924, 0948+6848 and 1004+6936.
2. To obtain the proper motion of M 82 relative to M 81, using two water masers on the opposite sides of M 82's kinematic center.
3. To derive orbital lower mass estimate to the mass of M 81.
4. To study the evolution and environment around the radio supernova SN 2008iz in M82.

The organization of the thesis is as follows: After an introduction to the concept of Very Long Baseline Interferometry in chapter 2, in chapter 3 we describe the observations and data reduction process. The results on the M 81 proper motion and the morphology of the continuum sources is presented in chapter 4. In chapter 5, we describe the results on the H_2O maser in M 82, present the proper motion of M 82 relative to M 81 and derive a lower mass estimate to the mass of M 81. Chapter 6 we describe the evolution of radio supernova SN 2008iz. Finally, a short summary of the work is presented in Chapter 7.

2. Radio Interferometry and Astrometry

The angular resolution and the sensitivity of a telescope increase with the angular diameter, D, of its aperture at a given frequency. This implies that, as the telescope gets larger, its resolution becomes better. However, constructing telescopes of ever increasing size is prohibitive for both technical and financial reasons. For instance, manufacturing irregularities make the accuracy of the shape of reflecting surface to decrease with increase in the size of a telescope's dish, the effects of wind load increase with telescope size, thermal deformations which cause differential expansion and contractions increase with the size of its structure, deflections due to changes in the gravitational force as the antenna is pointed to the different parts of the sky increase with dish size, and lastly, the building and maintenance costs are higher for larger telescopes. Confronted with all these challenges, taking advantage of interferometry and aperture synthesis techniques becomes a necessity. The techniques involve combining signals from two or more telescopes to mimic a single telescope whose angular resolution (but of course not sensitivity) would equal that of a single dish with a diameter equal to the largest separation between any two of the telescopes in the array. This observing technique is called Very Long Baseline Interferometry (VLBI). For a ground based VLBI array, the largest possible separation distance (or baseline) between any two telescopes is $\mathbf{D}\approx 10000\,\mathrm{km}$. The technique of interferometry is currently being used in a large number of radio astronomy instruments (e.g. JVLA, VLBA, ALMA, LOFAR, SKA). In this chapter we give an introduction into its fundamentals and describe the calibration and astrometric applications of interferometric data.

2.1. Principles of Very Long Baseline Interferometry

As mentioned above, interferometry is a technique used to obtain the resolution of a large telescope by using multiple smaller telescopes. As a matter of fact, the next generation of radio interferometer arrays will consist of very large number of telescopes. However, despite the increase in telescope numbers, the basic observables from such observations are the responses of individual baselines. In this section, we show the main steps of deriving the response of a simple connected interferometer. For a full description see, e.g., Thompson (1999).

In order to understand the principles of radio interferometry, let us consider two antennas separated by a baseline $\mathbf{b}$, receiving a signal from a distance extragalactic source in the direction of $\mathbf{s}$. In this derivation, we assume that the electromagnetic waves emerge from a far-field source (i.e. extragalactic) and can therefore be approximated to be plane waves. The schematic view of the two-element interferometer is shown in Fig.2.1.1. The time of arrival of a wave front at one antenna lags behind in comparison to that of the other antenna by the geometric time delay τ_{g} because of a simple difference in path length expressed as

$$\tau_{\mathrm{g}} = \frac{\mathbf{b}.\mathbf{s}}{\mathrm{c}} \tag{2.1.1}$$

where c is the speed of light. If the source is assumed to be monochromatic and the noise from both the receiver and the background is neglected, the received signals at the two antennas can be represented as

$$\mathrm{V}_1(\mathrm{t}) = \mathrm{V}_1 \cos(2\pi\nu\,\mathrm{t})$$

and

$$\mathrm{V}_2(\mathrm{t}) = \mathrm{V}_2 \cos(2\pi\nu\,[\mathrm{t} - \tau_{\mathrm{g}}]),$$

where V_1,V_2 represent the strength of the received signals at antennas 1 and 2 respectively; τ_g is the time delay, which is typically a slowly varying function of time due to the earth's rotation in the reception of a given wavefront at antenna 2 relative to antenna 1.

The combination of the two signals is performed via cross-correlation which first multiplies the two voltages to yield a product and then takes a time averaging long enough ($\triangle\mathrm{t} \gg (2\pi\nu)^{-1}$) to remove the high frequency term, such that,

$$\mathrm{V}_1(\mathrm{t}).\mathrm{V}_2(\mathrm{t}) = \mathrm{V}_1\cos(2\pi\nu\,\mathrm{t}) \times \mathrm{V}_2\cos(2\pi\nu\,[\mathrm{t} - \tau_{\mathrm{g}}]).$$

Hence,

$$\mathrm{V}_1(\mathrm{t}).\mathrm{V}_2(\mathrm{t}) = \mathrm{V}_1\mathrm{V}_2\cos(2\pi\nu\,\mathrm{t})\cos(2\pi\nu\,[\mathrm{t} - \tau_{\mathrm{g}}])$$

$$= \mathrm{V}_1\mathrm{V}_2[\cos(2\pi\nu\,\mathrm{t} - 2\pi\nu\,\tau_{\mathrm{g}}) + \cos(2\pi\nu\,\tau_{\mathrm{g}})]$$

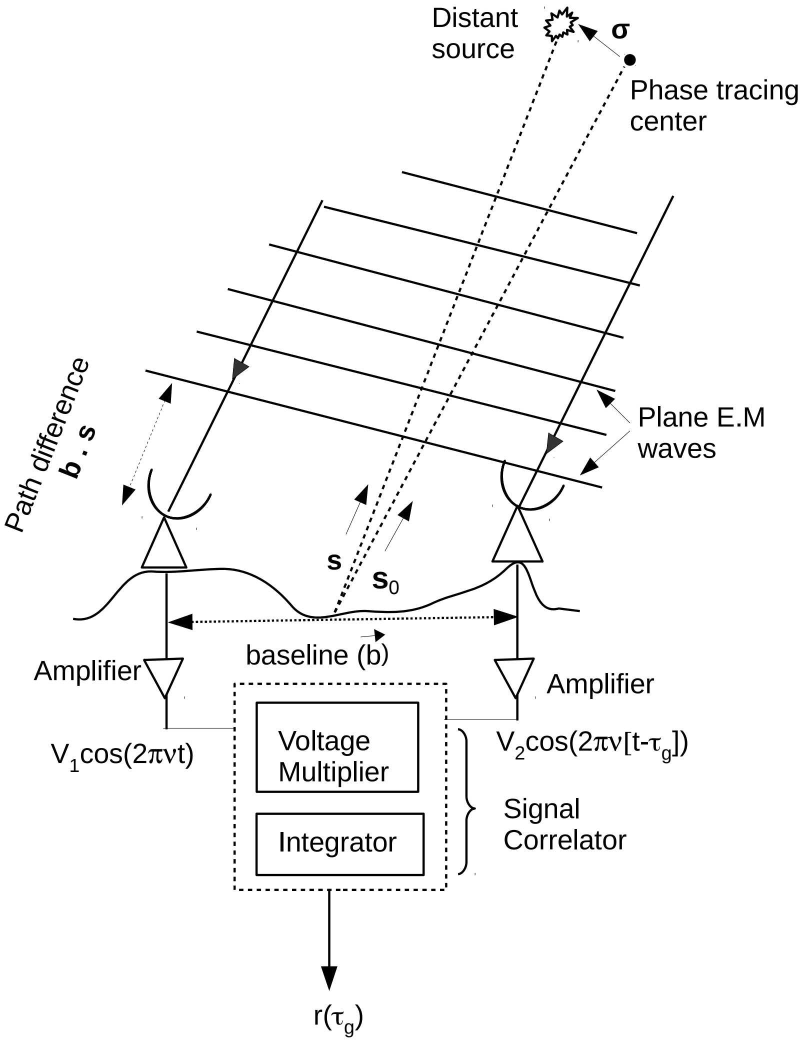

Figure 2.1.1.: A two-element interferometer schematic diagram illustrating an observation of a far field source (modified from Thompson 1999).

The output power $\mathbf{R}(\tau_g)$ of this correlator is thus

$$\mathrm{R}(\tau_\mathrm{g}) = < \mathrm{V}_1(\mathrm{t})\,\mathrm{V}_2(\mathrm{t}) > = \mathrm{V}_1\,\mathrm{V}_2\cos(2\pi\nu\,\tau_\mathrm{g}) \tag{2.1.2}$$

The product of the amplitudes V_1 and $\mathbf{V}_2$ is a representation of the total power received from the source and depends on:

(i) the specifications of the array .i.e. the effective collecting area A(s)=$\sqrt{\mathrm{A_1(s)\,.\,A_2(s)}}$ and the bandwidth of the receiver system $\Delta\nu$ and

(ii) the source properties .i.e. the specific surface brightness $\mathbf{I}_{(s)}$ and the two dimensional angular extent **s**.

Hence, the output power **R** can be described by the following integral over the solid angle dΩ as

$$\mathrm{R} = \Delta\nu \int_{\mathrm{s}} \mathrm{A(s)\,I(s)\,\cos(2\pi\nu\,\tau_g)\,d\Omega}. \qquad (2.1.3)$$

The correlation of the data from the individual telescopes is always performed for one particular position within the field of view (FOV), which is typically the pointing center of all telescopes. The pointing center is therefore referred to as the phase-tracking center which points in the direction of the unit vector $\mathbf{s_0}$ such that $\mathbf{s} = \mathbf{s}_0 + \sigma$ (Fig. 2.1.1). Rewriting Eqn2.1.3 in terms of **s** yields:

$$\mathrm{R} = \Delta\nu\cos\left(\frac{2\pi\nu\,\mathrm{b}.\hat{\mathrm{s}}_0}{\mathrm{c}}\right)\int_{\mathrm{s}} \mathrm{A}(\sigma)\,\mathrm{I}(\sigma)\cos\left(\frac{2\pi\nu\,\mathrm{b}.\sigma}{\mathrm{c}}\right)\mathrm{d}\Omega -$$

$$\Delta\nu\sin\left(\frac{2\pi\nu\,\mathrm{b}.\hat{\mathrm{s}}_0}{\mathrm{c}}\right).\int_{\mathrm{s}} \mathrm{A}(\sigma)\,\mathrm{I}(\sigma)\sin(\frac{2\pi\nu\,\mathrm{b}.\sigma}{\mathrm{c}})\,\mathrm{d}\Omega$$

$$\mathrm{R} = \mathrm{A_0}|\mathrm{V}|\Delta\nu\cos\left(\frac{2\pi\nu\,\mathrm{b}.\hat{\mathrm{s}}_0}{\mathrm{c}} - \phi_\upsilon\right). \qquad (2.1.4)$$

The relation 2.1.4 show that the amplitude |V| and the phase ϕ_υ of the correlator output are a measure for the visibility amplitude and visibility phase respectively. $\mathrm{A_0}$ denotes the maximal response of the antenna. A successful data calibration allows us to determine the visibility. However, the total visibility is given by a complex visibility function as

$$\mathrm{V} = |\mathrm{V}|.\mathrm{e}^{\mathrm{i}\phi_\upsilon} = \int_{\mathrm{s}} \mathrm{A_r}(\sigma)\,\mathrm{I}(\sigma)\,\mathrm{e}^{(-\mathrm{i}2\pi\nu\,\mathrm{b}.\sigma)/\mathrm{c}}\mathrm{d}\Omega \qquad (2.1.5)$$

Where the parameter $\mathrm{A_r}(\sigma) = \mathrm{A}(\sigma)/\mathrm{A_0}$ denotes the antenna response relative to its maximal value $\mathrm{A_0}$ when the source position falls directly into the beam center of the antenna. The Eqn2.1.5 shows that the visibility phase carries the information about the position of the source relative to the phase tracking center. Hence, $\phi_\upsilon = 0$ implies that $\sigma = 0$, meaning the source is located in the direction of $\mathbf{s}_0$.

So far we have assumed monochromatic radiation, but practically, observations are conducted with as large a bandwidth $\Delta\nu$ as possible to achieve maximal sensitivity (for continuum radiation). To properly account for this fact, Eqn 2.1.4 needs to be integrated over the bandwidth $\Delta\nu$. For a rectangular bandpass with a central frequency ν_0 the integration yields:

$$\mathrm{R} = \mathrm{A}_0|\mathrm{V}| \int_{\Delta\nu} \cos(2\pi\nu\,\tau_\mathrm{g} - \phi_\upsilon)\,\mathrm{d}\nu$$

$$= \mathrm{A}_0|\mathrm{V}|\Delta\nu\,\mathrm{sinc}(\Delta\nu\,\tau_\mathrm{g})\cos(2\pi\nu_0\,\tau_\mathrm{g} - \phi_\upsilon) \tag{2.1.6}$$

Due to the finite bandwidth and the geometric time delay, a dampening term called the delay beam appears. For $\Delta\nu\,\tau_\mathrm{g} > 1$ the signal will be attenuated considerably if not accounted for. Therefore, to counteract this effect, the geometric delay at the phase tracking center is being compensated for by introducing an instrumental delay, τ_i, just before correlation. In the ideal case $\tau_\mathrm{g} - \tau_\mathrm{i} \ll 1$ such that

$$\mathrm{R} \approx \mathrm{A}_0|\mathrm{V}|\Delta\nu\cos(\phi_\upsilon). \tag{2.1.7}$$

The phase tracking center and the pointing center of the individual antennas should coincide since this is where the response of each antenna is maximum. However, the instrumental delay can also be used to steer the beam of the interferometer throughout the FOV of the array such that

$$\mathrm{R} = \mathrm{A}_0|\mathrm{V}|\Delta\nu\cos(\delta_{\nu 0} - \phi_\upsilon) \tag{2.1.8}$$

where the phase term $\delta_{\nu 0} = 2\pi\nu_0(\tau_g - \tau_i)$ describes the location relative to which, positions of sources within the FOV are measured.

The ultimate goal of measuring |V| and ϕ_υ is to recover the intensity distribution of the source on the plane of the sky as it enters the visibility function in Eqn 2.1.5. In order to so, one defines the uvw-coordinate system which relates the coordinates of the antennas with those of the celestial objects, a shown in Fig. 2.1.2.

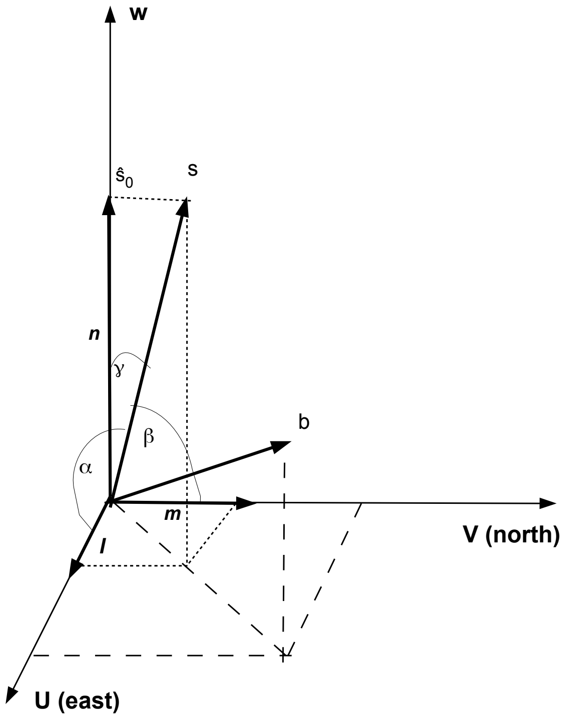

Figure 2.1.2.: Coordinate system used to relate the location of radio telescopes on Earth (baseline **b**) with those of celestial objects (in direction of **s**). The u- and v-axes point towards East and North, respectively, while w points towards the phase tracking center $\mathbf{s}_0$ (image courtesy of Kirsten, 2014).

In this scheme, the source vector, **s**, is given by the direction cosines

$$\mathrm{s} = (\cos\alpha,\, \cos\beta,\, \cos\gamma) = (\mathrm{l},\, \mathrm{m},\, \sqrt{1-\mathrm{l}^2-\mathrm{m}^2}), \qquad (2.1.9)$$

while the baseline vector, **b**, has components (u, v, w) and is measured in wavelength $\lambda = \mathrm{c}/\nu$:

$$\mathrm{b} = \lambda(\mathrm{u},\mathrm{v},\mathrm{w}). \qquad (2.1.10)$$

With this definition of coordinates, the visibility function can be rewritten to read

$$\mathrm{V}(\mathrm{u},\mathrm{v}) = \int_{-\infty}^{\infty}\int_{-\infty}^{\infty} \mathrm{A_r}(\mathrm{l},\mathrm{m})\,\mathrm{I}(\mathrm{l},\mathrm{m})\,\mathrm{e}^{(-2\pi \mathrm{i}[\mathrm{ul}+\mathrm{vm}+\mathrm{w}(\sqrt{1-\mathrm{l}^2-\mathrm{m}^2}-1)])}\,\frac{\mathrm{dl}\,\mathrm{dm}}{1-\mathrm{l}^2-\mathrm{m}^2}$$

$$\approx \int_{-\infty}^{\infty} \mathrm{I}(\mathrm{l},\mathrm{m})\, \mathrm{e}^{-2\pi \mathrm{i}(\mathrm{ul}+\mathrm{vm})}\, \mathrm{dl}\, \mathrm{dm} \tag{2.1.11}$$

where in the final step it is assumed that the correlation is performed at, or at least close to, the pointing center such that $\mathrm{A_r}(0,0) \approx 1$. Furthermore, the sources observed in interferometric observations are located at small angular distances from the phase tracking center, such that $|\mathrm{l}|, |\mathrm{m}| \ll 1$. Hence, the visibility function as derived in Eqn 2.1.11, is simply the Fourier transform of the intensity distribution of the source.

In order to reconstruct $\mathrm{I}(\mathrm{l},\mathrm{m})$, the visibility function needs to be sampled at as many points in the uv-plane as possible. This is achieved by:

1. Making use of a large number of antennas at varying distances from each other to increase the number of individual baselines. This is achievable because the total number of baselines formed by an array of N antennas is given by N(N-1)/2,
2. Observing at a large bandwidth that is sampled at a large number of individual frequencies (channels) and thereby mimicking different baselines (Eqn. 2.1.10); and
3. Observing for long periods of time and employing what is known as Earth rotation synthesis. Earth rotation synthesis takes advantage of the fact that the baseline (**b**) changes constantly during the Earth's rotation. Therefore, each integration time t_i yields a new sample of the visibility function and, hence, the intensity distribution $\mathrm{I}\,(\mathrm{l},\mathrm{m})$.

The recovery of $\mathrm{I}(\mathrm{l},\mathrm{m})$ is performed through Fourier inversion and deconvolution in a process called imaging. Since the visibility function is sampled discretely at individual integration times t_i and frequency channels ν_i, equation 2.1.11 becomes a sum over the $2n$ visibilities which after inversion reads

$$\mathrm{I^D}(\mathrm{l_s},\mathrm{m_s}) = \mathrm{K}.\sum_{\mathrm{k}=0}^{2\mathrm{n}} \mathrm{V}(\mathrm{u},\mathrm{v}).\,\mathrm{S}(\mathrm{u},\mathrm{v}).\,\mathrm{e}^{2\pi \mathrm{i}(\mathrm{u_k l_2}+\mathrm{v_k m_s})} \tag{2.1.12}$$

Where $\mathrm{K} = (2\mathrm{n}+1)^{-1}$ is a normalization factor. The superscript **D** in the above equation indicates that at this stage the intensity distribution is a convolution of the real intensity distribution with the point spread function of the array, which is also termed as the dirty beam

$$\mathrm{B}(\mathrm{l_s},\mathrm{m_s}) = \sum_{\mathrm{k}=0}^{2\mathrm{n}} \mathrm{S}(\mathrm{u},\mathrm{v}).\,\mathrm{e}^{2\pi \mathrm{i}(\mathrm{u_k l_2}+\mathrm{v_k m_s})} \tag{2.1.13}$$

where

$$\mathrm{S(u,v)} = \sum_{\mathrm{k=0}}^{\mathrm{2n}} \mathrm{W_k}\delta^2(\mathrm{u - u_k,\ v - v_k}) \tag{2.1.14}$$

is the weighted (weights W_k) sampling function discretizing V(u,v). Hence, to reconstruct the real intensity distribution, the dirty image (Eqn.2.1.12) needs to be deconvolved from the dirty beam. This is typically done by employing the CLEAN algorithm (Högbom, 1974) and variants thereof. In Eqn. 2.1.14, the weights W_k can be chosen to emphasize certain visibilities more than others influencing the shape of the interferometer beam. For instance, if visibilities representing shorter baselines have the highest weights, the weighting scheme is called natural weighting. On the other hand, emphasis on longer baselines is achieved through uniform weighting. Since a typical VLBI array consists of more short than long baselines (see Fig.2.1.3), the weighting schemes are achieved by either; assigning the same weight to each point in the uv-plane (natural, focus on sensitivity), or the same weight to each grid-cell in the uv-plane (uniform, focus on high angular resolution). At this point, it is important to note that the longer the smallest baseline $\mathrm{D_{min}}$ of an interferometer is, the smaller will the angular scale be at which the array is sensitive to emission. This results to the resolving out of the extended sources whose size is larger than the full-width-half-maxium (FWHM) $\theta = 1.22\frac{\lambda}{\mathrm{D_{min}}}$.

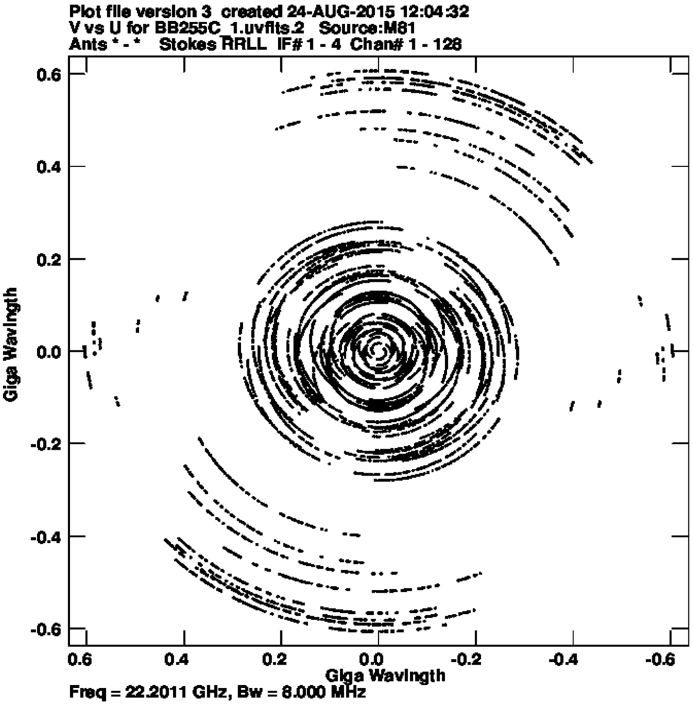

Figure 2.1.3.: Example of the (u,v)-coverage of one of our VLBI 10 hour observations at K-band.

2.2. Calibration of Interferometric Data

This section focuses on the phase calibration procedure, because our astrometric observations of quasars and water masers were aimed at the accurate measurement of positions. Of course the information on the flux density is also obtained, but it is of minor interest in astrometry. For a detailed description of the VLBI amplitude calibration procedure, the reader is referred to, e.g. Fomalont and Perley (1999).

As mentioned in the previous section, for the correlation of data from radio interferometric observations often a specific location is chosen in the FOV referred to as phase tracking center, by introducing an instrumental time delay τ_i. In the ideal case, τ_i is chosen to compensate for the geometric time delay τ_g such that the fringe phase ϕ_ν is equal to zero at the phase tracking center for all individual frequency channels ν_i at all integration times t_i. However, the geometric model that computes τ_g and, hence, τ_i, is often not very accurate, which results in a residual phase error. As expected, there are other factors that can cause phase errors such as different receiver back-ends, time offsets between the individual telescopes, time delay due to propagation through the atmosphere.

The greatest challenge is trying to deal with the unpredictable temporal changes in the Earth's ionosphere and troposphere. The troposphere is the atmospheric layer between Earth's surface and an altitude of about 60 km, while the ionosphere ranges from about 60 km to an altitude of 1000 km. The atmospheric changes are known to introduce a dispersive ($\propto \nu^{-1}$) and a non-dispersive ($\propto \nu$) phase error for the ionosphere and troposphere respectively (e.g. Chatterjee et al., 2004).

This challenge dominates the VLBI observations, during which unlike for the smaller-connected radio interferometers like the JVLA, each antenna of the array looks through very different parts of the constantly changing atmosphere (Fig. 2.2.1). As a result, fringe phase offsets ($\Delta\phi_\nu(\mathrm{t})$), fringe rates ($\mathrm{d}\phi_\nu \mathrm{dt}$), and phase slopes ($\mathrm{d}\phi_\nu \mathrm{d}\nu$) affect the correlated data leading to complete de-correlation in the worst cases. As mentioned earlier, these phase errors can be modeled and accounted for provided the phase tracking center coincides with the position of a strong point source. In such a case, $\phi_\nu = \mathrm{d}\phi_\nu\,\mathrm{dt} = \mathrm{d}\phi_\nu\,\mathrm{d}\nu = 0$ for all telescope pairs by definition (Eqn. 2.1.12), which makes it possible to compensate for any offsets, unless they have a $2\mathrm{n}\pi$ ambiguity. This calibration step is commonly referred to as *fringe fitting*. Finally, the positions of sources within the FOV of the array are measured relative to the position of this strong point source. This type of calibration is referred to as in-beam calibration because the calibrator source lies within the beam observing the target source. Practically, for high frequency observations, the number of suitable calibrator sources is limited making it highly improbable for the target object and the calibrator to lie within the same beam. However, the in-beam calibration has been quite successful for low frequency observations.

Ordinarily, the source of interest is either rather faint, or it is not a point source, or its position is not accurately known, and/or it might be located far from the phase tracking center. In these cases, radio interferometric observations always include the observations of at least one nearby, often within a few degrees calibrator (point) source with an accurately known position and morphology [1]. Phase-referencing observations are conducted in such a way that, the antennas quickly move back and forth between calibrator and target source every few minutes (or even more frequently) depending of the frequency to maintain phase connection. After correlation, the phases of all antennas are referenced to one antenna of the array, to synchronize the time of arrival of individual wave fronts. The phase solutions found in this step are then applied to the data of the target source. The last step cannot however, account for differences in the atmosphere along the slightly different lines-of-sight to calibrator and target (Fig.2.2.1) resulting in residual phase errors. To keep such errors small, it is essential for the calibrator source to be as close to the target source as possible.

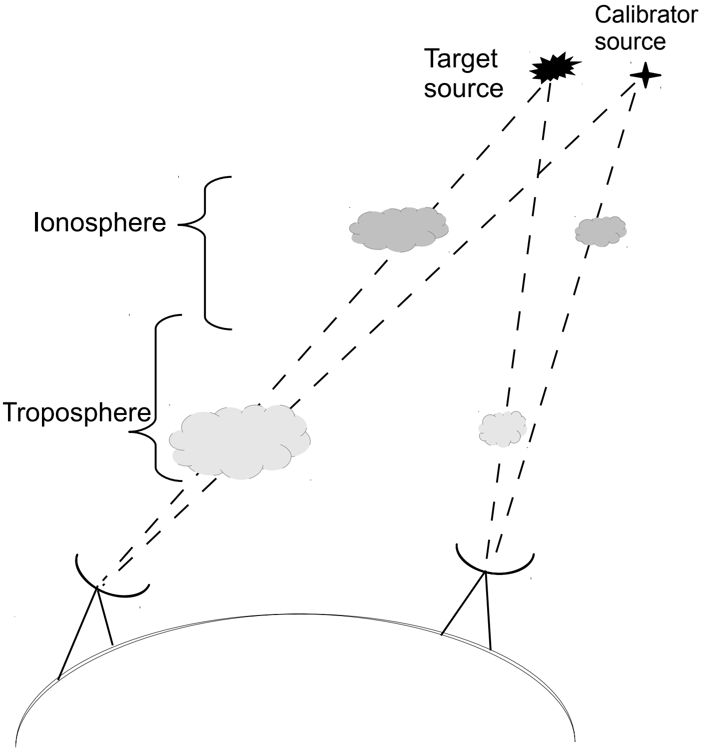

Figure 2.2.1.: Lines of sight crossing different parts of the atmosphere towards calibrator source and target for two different telescopes (image courtesy of Kirsten, 2014).

---

[1] A list of suitable calibrator sources can, e.g., be found at http://www.vlba.nrao.edu/astro/calib/

However, regardless of how close the calibrator source is, some residual delays caused by the differential atmosphere remain, influencing the accuracy of position measurements. The only way to take care of this effect is to have a strong compact source which is, ideally, also of extragalactic origin within the beam observing the target source.

Once the calibration solutions from the phase referencing source have been applied, further refinement of the phase solution can be obtained in a process known as self-calibration. For that, a first model of the source is constructed by, e.g., imaging. The observed visibilities V_{ij}^{obs} of any pair of antennas (i,j) are then compared with the theoretical ones, V_{ij}^{mod}, for this model. The true visibilities $\mathrm{V_{ij}^{true}}$ are distorted by the complex gains $\mathrm{G_j = G_j\, e^{i\phi_j}}$ of the individual telescopes such that

$$\mathrm{V_{ij}^{obs} = G_i G_j^{\star} V_{ij}^{true}}. \tag{2.2.1}$$

Inserting Eqn. 2.1.5 yields

$$\mathrm{|V_{ij}^{obs}| e^{i\phi_{ij}^{obs}} = |G_i||G_j||V_{ij}| e^{i(\phi_i - \phi_j + \phi_{ij}^{true})}}. \tag{2.2.2}$$

If the product of the observed visibilities as given above obtained from the three baselines of any three telescopes (i, j, k) of an interferometric array is considered, comparison of the phase terms in Eqn. 2.2.2 yields the so-called closure phase $\phi^{closure}$

$$\begin{aligned}\phi_{\mathrm{ijk}}^{\mathrm{closure}} &= \phi_{\mathrm{ij}}^{\mathrm{obs}} + \phi_{\mathrm{jk}}^{\mathrm{obs}} + \phi_{\mathrm{ki}}^{\mathrm{obs}} \\ &= \phi_{\mathrm{ij}}^{\mathrm{true}} + \phi_{\mathrm{jk}}^{\mathrm{true}} + \phi_{\mathrm{ki}}^{\mathrm{true}}.\end{aligned} \tag{2.2.3}$$

In this expression, the closure phase is independent of the antenna based gains. Therefore, given the known setup of the array and the previously obtained model, the true visibilities can be predicted. Any offsets between the closure phase given by the observed visibilities and those as predicted by the model must then be related to the antenna based gains. The latter can then be adjusted until the observations match the model.

The above calibration steps are typically performed using astronomical software packages such as the *Common Astronomy Software Application* (CASA[2]) or the *Astronomical Image Processing System* (AIPS[3]). For global VLBI observations, as are discussed in this thesis,

---

[2] http://casa.nrao.edu/

[3] http://www.aips.nrao.edu/index.shtml

AIPS is often preferred because unlike CASA, it contains routines to perform fringe fitting. In AIPS, all calibration solutions are stored in so-called *tables* that contain the computed modifications to amplitudes and phases. The solutions from individual calibration steps are typically stored in the SN-tables, all of which are eventually combined in a CL-table. The CL-table, together with the BP-table which contain calibration of the bandpass response of the individual telescopes, are applied to the uncalibrated data before imaging.

2.3. Astrometry

Radio interferometric observations, in particular with VLBI, are one of the best way to obtain precise measurement of the absolute and relative positions of celestial objects. The position measurement activity is known as astrometry. The measured visibility phase contains all information about the position of a source. Therefore, the phase calibration has to be done very carefully in astrometric observations. Here we will follow the descriptions by Beasley and Conway (1995) and Fomalont (1999).

2.3.1. Phase-Referencing

Astrometric accuracy is limited by offsets and fluctuations of the observed delays, which are caused by (i) the priori geometrical delay model error, (ii) the delay due to passage through air and ionospheres (i.e. atmospheric and ionospheric phase errors) and (iii) the delay due to signal passage through the electronics in each antenna (instrumental phase errors which includes cable delays, local oscillator phase, instability of the independent frequency standards, and time mis-synchronization). In phase referencing, the calibrator scans (single on-source duration) are normally interleaved and has a total duration T_s, as shown in Fig.2.3.1. An observation period from a beginning of a calibrator scan, then a target scan, and to the beginning of a calibrator scan again is referred to a switching cycle. Keeping T_s short, a scientifically interesting target can be observed with an adjacent reference calibrator almost simultaneously by fast antenna pointing change (antenna switching). This is to compensate for the rapid target fringe phase fluctuations due to atmosphere which affect the calibrator fringe phase. Phase referencing can also remove the long-term phase drifts due to the baseline errors and atmospheric delay errors.

One of the functions of a correlator is to remove the effects of total delay using a delay model. However, inevitably, this model has a limited accuracy. As a result, the visibilities generated by a correlator contain phase errors.

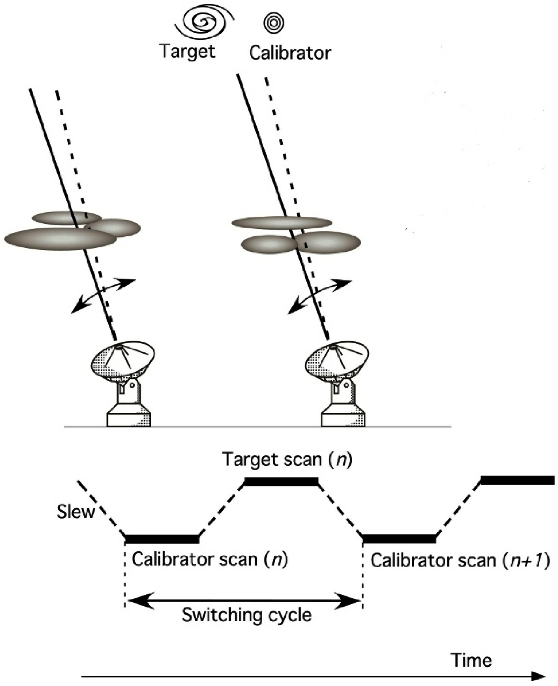

Figure 2.3.1.: Schematic drawing of a typical phase referencing observation. Courtesy of Asaki et al. (2007).

2.3.2. Total phase delay

As shown in Eqn. 2.1.3, the output of an interferometer is a quasi-sinusoidal response

$$\mathrm{R} = \mathrm{A}.\cos(\phi_{\mathrm{T}}) \tag{2.3.1}$$

where ϕ_T is the total phase delay. It is given by the path-length difference of the signals from the two telescopes as well as the visibility phase and has various contributions:

$$\phi_{\mathrm{T}} = 2\pi\nu\left(\tau_{\mathrm{g}} + \tau_{\mathrm{n}}\right) + \phi_{\mathrm{d}} + \phi_{\upsilon} \tag{2.3.2}$$

Here τ_g is the geometric delay defined in Eqn. 2.1.1. It depends only on the relative positions of the telescopes, i.e. the baseline $\mathbf{b}$ and the source position $\mathbf{s}_0$. The term τ_n includes all non-dispersive delays which are not frequency dependent. The non-dispersive delays include tropospheric refraction, clock errors at the telescopes and path length changes in the telescope electronics. The dispersive phase changes which are caused by effects that do not depend linearly on frequency are represented by ϕ_d. One example of such a phase change is the effect of the ionosphere on the signal. The final contribution to the total phase delay is the visibility phase ϕ_{υ} for extended sources.

The correlator calculates a model phase ϕ_M. This correlator model takes into account a large number of effects, which includes the geometry of the interferometer like the positions of the source and the telescope, the nutation and precession of the Earth as well as the tectonic motion, and tidal effects. The effects of the light deflection in the gravitational potential of the sun and the planets are also included. VLBI usually uses the *fringe phase* which is the fractional part of the difference between the model phase delay and the true total phase delay.

2.3.3. Tropospheric delay corrections

The tropospheric effect on a signal appears as an extra delay in the measurement of the signal traveling from the far-field to the antenna. This delay depends on the temperature, pressure and humidity. It remains the dominant error of the tropospheric delay model, which is applied by the VLBA correlator at observing frequency greater than 5 GHz (Wrobel, 1999). The VLBA correlator model uses a seasonally averaged and latitude-dependent atmospheric model (Niell, 1996). This model often mis-estimates the zenith delay by a few centimeters. For an understanding of the tropospheric delay errors, we will discuss the effect of neutral atmosphere on a signal.

If we consider an electromagnetic wave that propagates through a dielectric medium with refractive index n, it will travel with a phase velocity of $\mathrm{c/n}$. This implies that the wave will have a delay $\triangle \mathrm{t} = \int (\mathrm{n}-1)/\mathrm{c}\,\mathrm{dx}$ compared to a wave in vacuum. This time delay can be interpreted as an excess path length $\mathrm{c}\triangle\mathrm{t}$, or can be written as:

$$\mathrm{l} = 10^{-6} \int \mathrm{N(x)\,dx} \qquad (2.3.3)$$

where n is the refractive index of air and N, often defined as $\mathrm{N} = 10^{6}(\mathrm{n}-1)$, is the refractivity. The refractivity can be divided in dry gas and moist gas components i.e. $\mathrm{N} = \mathrm{N_{dry\,air}} + \mathrm{N_{moist\,air}}$. The refractivity of moist air is given by the Smith-Weintraub Equation as

$$\mathrm{N} = 77.6\frac{\mathrm{p_D}}{\mathrm{T}} + 64.8\frac{\mathrm{p_V}}{\mathrm{T}} + 3.776 \times 10^{5}\frac{\mathrm{p_V}}{\mathrm{T^2}} \qquad (2.3.4)$$

where T is the temperature in Kelvin, p_D is the partial pressure of the dry air and p_V is the partial pressure of water vapor in millibars.

If we consider a layer of gas in static equilibrium between pressure and gravity, it can be shown that the excess path length due to dry air in the zenith direction can be expressed as

$$\mathrm{l_D} \approx 0.228 \frac{\mathrm{cm}}{\mathrm{mb}} \mathrm{P_0} \tag{2.3.5}$$

where P_0 is the surface pressure (e.g. Thompson et al., 1986). Therefore, the dry excess path length for a pressure of 1013 mb is 231 cm. On the other hand, the excess path length due to the wet component can be approximated by

$$\mathrm{l_V} \approx 7.6 \times 10^4 \frac{\mathrm{P_{V_0}}}{\mathrm{T^2}}, \tag{2.3.6}$$

where P_{V_0} is the partial pressure of water vapor at the surface.

The simplest atmospheric model is that of a uniform flat slab. Here, the signal from a source at zenith angle Z will see excess path length of $\mathrm{l_0 \sec(Z)}$ given l_0 is the zenith excess path length. In a more realistic case, where the refractivity is exponentially distributed with a scale height $\mathrm{h_0}$, the excess path length can be described as

$$\mathrm{l} \approx 0.228 \mathrm{P_0} \sec\mathrm{Z} \, (1 - 0.0013 \tan^2\mathrm{Z}) + \frac{7.5 \times 10^4 \, \mathrm{P_{V_0}} \sec\mathrm{Z}}{\mathrm{T^2}} \, (1 - 0.0003 \tan^2\mathrm{Z}), \tag{2.3.7}$$

where the scale height of the dry and wet atmosphere were 8 km and 2 km respectively.

If the zenith delay of the dry atmosphere is mis-estimated in the correlator model by δl_0, the signal from a source at zenith angle Z will have a delay error of

$$\delta \mathrm{l(Z)} \approx \delta \mathrm{l_0} \sec(\mathrm{Z}) \, (1 - 0.0013 \tan^2\mathrm{Z}). \tag{2.3.8}$$

Practically, the zenith delay error is different for the calibrator and the target source since both sources usually have different zenith angles $Z_c$and Z_t. A fringe-fit on the calibrator will correct both sources for the same value $\delta \mathrm{l(Z_c)}$. Hence, a residual error of $\delta \mathrm{l(Z_c)} - \delta \mathrm{l(Z_t)}$ will remain after phase-referencing for the target source. If the correlator model mis-estimated the zenith delay l_0 by 3 cm (∼0.1 ns), one would expect delay errors of 0.2 cm for zenith angles of ∼60° and source separation of ∼1°. The most commonly and reliable method to estimate the zenith delay offset is to use *geodetic-like* observations. A process that involves observation of a number of bright and compact radio sources with positions known to 1 mas at different elevations. The details of *geodetic-like* observations is discussed in section 3.2.

2.3.4. Relative Astrometry

The correlator model contains both the geometric delay errors (which we would like to know) and other additional parameters known only to a certain accuracy (which need to be removed from the data). This will result in residuals in the observed fringe phase. These residuals can be written as

$$\phi(\mathrm{t}) = \phi_{\upsilon}(\mathrm{t}) + \phi_{\mathrm{ins}}(\mathrm{t}) + \phi_{\mathrm{pos}}(\mathrm{t}) + \phi_{\mathrm{ant}}(\mathrm{t}) + \phi_{\mathrm{atm}}(\mathrm{t}) + \phi_{\mathrm{ion}}(\mathrm{t}). \tag{2.3.9}$$

where ϕ_{υ} are visibility phase contributions, ϕ_{ins} are phase errors caused by instrumental effects, ϕ_{pos} and ϕ_{ant} are residual phase errors caused by source and antenna positions, respectively. The atmospheric residual phase errors are ϕ_{atm} and ϕ_{ion} for neutral atmosphere and ionosphere, respectively.

The residual phases are self-calibrated using the data of the source itself if the target source is strong enough and knowledge of its absolute position is not needed. For weak sources, or if the goal of the observation is to determine the position of the source, the technique of phase-referencing can be used to correct this errors. This is done using a bright and nearby calibrator source as a calibrator to the data. The concept of phase-referencing, is based on the assumption that the phase errors of two sources with a small angular separation on the sky are similar. One observes the target source between scans on the calibrator. Then one can interpolate the calibration between the two scans and apply this interpolated phase corrections ϕ^{i} to the phase of the target source ϕ^{t}.

$$\begin{aligned} \phi^{\mathrm{t}} - \phi^{\mathrm{i}} = \phi^{\mathrm{t}}_{\upsilon} + (\phi^{\mathrm{t}}_{\mathrm{ins}} - \phi^{\mathrm{i}}_{\mathrm{ins}}) + (\phi^{\mathrm{t}}_{\mathrm{pos}} - \phi^{\mathrm{i}}_{\mathrm{pos}}) + (\phi^{\mathrm{t}}_{\mathrm{ant}} - \phi^{\mathrm{i}}_{\mathrm{ant}}) \\ + (\phi^{\mathrm{t}}_{\mathrm{atm}} - \phi^{\mathrm{i}}_{\mathrm{atm}}) + (\phi^{\mathrm{t}}_{\mathrm{ion}} - \phi^{\mathrm{i}}_{\mathrm{ion}}) \end{aligned} \tag{2.3.10}$$

Here we assume that the calibrator source is unresolved, i.e. $\phi^{\mathrm{i}}_{\upsilon} = 0$. Now we assume that the errors are similar for both sources, i.e. $\phi^{\mathrm{t}}_{\mathrm{ins}} \approx \phi^{\mathrm{i}}_{\mathrm{ins}}$, $\phi^{\mathrm{t}}_{\mathrm{ant}} \approx \phi^{\mathrm{i}}_{\mathrm{ant}}$, $\phi^{\mathrm{t}}_{\mathrm{atm}} \approx \phi^{\mathrm{i}}_{\mathrm{atm}}$ and $\phi^{\mathrm{t}}_{\mathrm{ion}} \approx \phi^{\mathrm{i}}_{\mathrm{ion}}$. Then we can write

$$\phi^{\mathrm{t}} - \phi^{\mathrm{i}} = \phi^{\mathrm{t}}_{\upsilon} + (\phi^{\mathrm{t}}_{\mathrm{pos}} - \phi^{\mathrm{i}}_{\mathrm{pos}}). \tag{2.3.11}$$

This means that, the phase-referenced difference phase contains only the information about the target source structure and its position relative to the calibrator together with noise from interpolation errors.

3. Observation and Data reduction

In this chapter, we present the general information on the VLBA data observed for proper motion measurements, the procedure for tropospheric delay correction using geodetic-like observations and a discussion on the calibration procedure.

3.1. VLBA Observations

The observations target the compact radio source at the core of M 81 (M 81*), H_2O masers in M 82 and three background quasars (0945+6924, 0948+6848, 1004+6936). The observations were first conducted once per year for 3 years at X- (8.4 GHz), U- (15.3 GHz) and K-band (22.2 GHz). The observations at K-band were repeated in December 2015 as summarized in table. 3.2. We used the VLBA antennas, the Green Bank 100 m-telescope (GB), the Effelsberg 100 m-telescope (EF) and the phased 27 VLA antennas (see details in table 3.1). Effelsberg is located close to Bonn, Germany, and Green Bank is located in West Virginia, USA. Thus, the baselines to Effelsberg are the longest ones (5602 to 10328 kilometres) and give the highest resolution. The inclusion of non-VLBA antennas, which have the largest collecting area, was to increase the sensitivity of the array in order to detect as many maser features as possible. However, their inclusion come with two main downsides. First, they result in longer switching times for phase-referencing, because the non VLBA antenna cannot switch between sources as fast as the VLBA antennas, which were specifically optimized for this purpose. Second, they cannot be included in the dynamic scheduling for the VLBA, hence, the observations involving them have to be on a fixed date regardless of the weather conditions.

The X- and U-band observations comprised of continuum sources i.e. the calibrator (M 81*) and the 3 background quasars. The observations were done using only the VLBA antennas in four sub-bands of 8 MHz bandwidth in dual circular polarization, with 16 spectral channels in each band yielding a channel spacing of 0.5 MHz. The observations involved rapid switching between the phase-calibrator, M 81*, and the three background quasars (0945+6924, 0948+6848, and 1004+6936), over a total observing time of 12 hours. The observing sequence is M 81* – 0945+6924 – M 81* – 0948+6848 – M 81* – 1004+6936 – M 81*. During the observations, three strong calibrators sources (i.e. 3C345, DA 193 and J1048+7143) were observed as fringe finders. The calibrator 3C345 was observed at the end of the observations for ∼4 minutes. The calibrators DA 193 and J1048+7143 were observed several times during the observation for ∼2 minutes every cycle. The entire observation yielded a total observing time of

$\sim$10 hours for all sources at both observing bands.

The K-band observations comprised targeted continuum and spectral line sources and were therefore analyzed for continuum sources and maser line emission. The observations included all VLBA antennas, EB, GB and the phased VLA to ensure a good SNR on the weak water maser sources (see table.3.2). After observation at the respective telescope stations, the data underwent 3 correlator passes with 3 positions for M 82 (i.e. R. A=09:55:50.91932 Dec=+69:40:45.5433, R. A=09:55:54.83367 Dec=+69:40:53.8233, and R. A=09:55:51.38702 Dec=+69:40:44.4676). This resulted to the data being grouped into three sets, each of which allowed mapping of the different locations observed for water maser emission in M 82. The observations were conducted in four sub-bands of 8 MHz bandwidth in dual circular polarization, with 128 spectral channels with each band yielding a channel spacing of 62.5 kHz which is equivalent to 0.84 km s^{-1}. The 21 and 27 December 2015 observations were conducted in two sub-bands of 32 MHz bandwidth in dual circular polarization, with 1024 spectral channels in each band, yielding a channel spacing of 31.25 kHz which is equivalent to 0.42 km s^{-1}. The K-band observations involved rapid switching between the phase-calibrator M 81*, source (M 82), and three background quasars (see Fig. 4.1). The switching time between sources is 50 seconds in the sequence M 81* – M 82 – M 81* – 0945+6924 – M 81* – 0948+6848 – M 81* – M 82 – M 81* – 1004+6936 – M 81*. Over the entire observation of 12 hours, we spent 4 hours on the calibrator (M 81*), 2 hours on M 82, 30 minutes on each of the 3 background quasars and 30 minutes on each of the 3 geodetic block observations. Additionally, data of two strong calibrator sources (DA 193 and J1048+7143) were taken for the delay calibration. Each of them was observed several times during the observation for $\sim$5 minutes every cycle. The datasets were recorded in the MARK5A mode at a data rate of 256 Mb s^{-1} for 2007–2009, and MARK5C at a data rate of 512 Mb s^{-1} for the 2015 datasets. All data were correlated at the NRAO in Socorro.

3.2. Geodetic - like observations

The concept of phase referencing is based on the assumption that the phase errors of any two sources with a small angular separation on the sky are similar. The main problem encountered when using the phase-referencing VLBI technique are the phase errors due to the unknown tropospheric zenith delay at each antenna (Brunthaler et al., 2005a). Brunthaler et al. (2005a) presented two independent methods to estimate the zenith delay offsets at each antenna. These involve the least-square fit to the phase data of a strong target source (phase fitting) and use of geodetic-like observations. The images obtained from these two independent methods are similar and the positions measured from the images are also consistent.

For this work, we choose to perform geodetic block observations to determine the tropospheric zenith delay corrections (see section.2.3.3). With this technique improvements of the image peak-to-noise ratio by $\approx 30\%$ have been achieved, resulting in an astrometric accuracy of up to $10\,\mu$as (Brunthaler et al., 2005a). The tropospheric zenith delay is dependent on the observing frequency and the source position. To correct for the phase delay due to different airmass along the line-of-sight of the observed sources, 13 – 18 strong compact radio quasars (>200 mJy) with accurate positions known to better than 1 mas were observed over a large range of elevations. The strong and compact nature of the geodetic block sources allows detections even at low elevations angles ($< 20^\circ$) where atmospheric attenuation can be significant (see Reid and Brunthaler, 2004 and Brunthaler et al., 2005a).

The zenith delays are determined by multi-band delays (MBD) which is the rate of phase change with frequency. The observation frequency set up to enable the MBD was eight subbands of 8 MHz bandwidth in left circular polarization, with 16 spectral channels at U- and K-bands for the 2007-2009 datasets. The 2015 K-band observation set up was four sub-bands of 32 MHz bandwidth in left circular polarization with 1024 spectral channels. Geodetic block observations in the U and K-bands allow tropospheric delay corrections that scale with frequency and have a sec(ZA) dependence. The observing time was 30 minutes for each block measured every 4 hours (i.e. at the beginning, in the middle and at the end of the observation), resulting in a total dwell time of 90 minutes. The multiple observations allows one to monitor slow changes in the total tropospheric delay for each telescope.

The estimate of tropospheric and clock delay errors for each antenna from the geodetic data was done using the ParselTongue[1] run Python-based script called "BeSSeLmaster.2.2.0.py", written for the BeSSel survey[2] by Andreas Brunthaler. The script first corrects for phase

---

[1] http://www.jive.nl/jivewiki/doku.php?id=parseltongue:parseltongue

[2] http:www3.mpifr-bonn.mpg.de/staff/abrunthaler/BeSSeL/index.shtml

errors due to ionospheric effects using Total Electron Content (TEC) maps and inaccurate Earth orientation parameters (EOPs) in the correlator. Each of this tasks produces a new CL-table. The script then performs delay calibration to correct for phase offsets and instrumental single band delay for each IF. This generates an SN-table which is transfered to a new CL-table. After this corrections, the only other step left is to account for the phase gradient with frequency across the IF bands (i.e. the Multi-band delay), which is caused by the tropospheric delay and clock errors. A fringe fit to the data yields a multi-band delay solution (i.e. one solution for all 8 IFs combined) and rates for each antenna. A linear fit to the multi-band delay solution estimates the tropospheric zenith delay which is stored as an ATMOS.FITS file to be applied to the model during calibration of the target observations.

Table 3.1.: Description of the Antennas

Antenna	Diameter (m)	Affiliation and Location
Y27 (VLA)^a	130^b	NRAO, near Socorro, New Mexico
EB	100	Max-Planck-Institut für Radioastronomie, Effelsberg, Germany
GB	100	NRAO, Green Bank, West Virginia
BR (VLBA)	25	NRAO, Brewster, Washington
FD (VLBA)	25	NRAO, Fort Davis, Texas
HN (VLBA)	25	NRAO, Hancock, New Hampshire
KP (VLBA)	25	NRAO, Kitt Peak, Arizona
LA (VLBA)	25	NRAO, Los Alamos, New mexico
MK (VLBA)	25	NRAO, Mauna Kea, Hawaii
NL (VLBA)	25	NRAO, North Liberty, Iowa
OV (VLBA)	25	NRAO, Owens Valley, California
PT (VLBA)	25	NRAO, Pie Town, New mexico
SC (VLBA)	25	NRAO, Saint Croix, Virgin Islands

[a] A phased array of all the 27 25 m-VLA antennas.
[b] The equivalent diameter of the phased array.

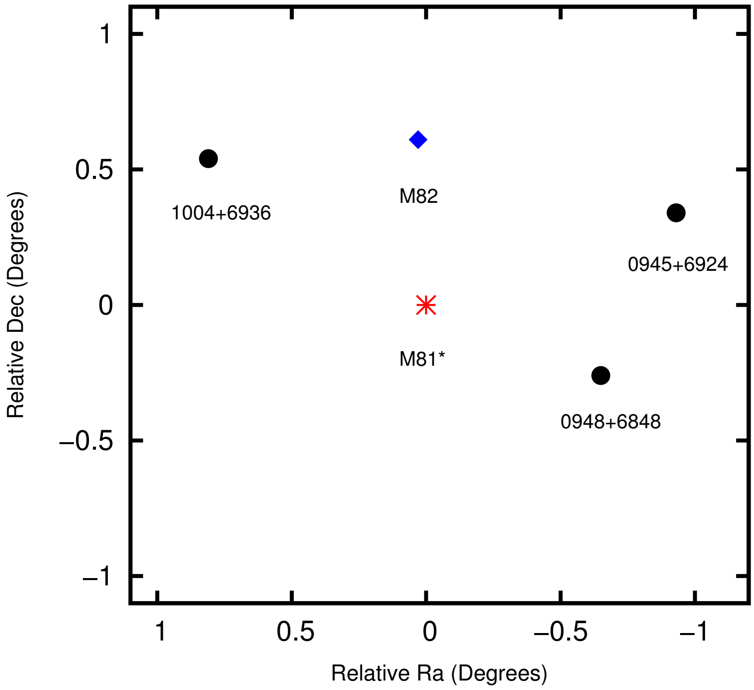

Figure 3.2.1.: The position of the sources relative to M81*, which served as the phase-referencing source over the entire observations. The black "dots" denotes extragalactic objetcs, the blue "diamond" denotes the position of M82 galaxy and the red "asterisk" denotes the position of M81*.

Table 3.2.: Details of the observation

Epoch	Observing Code	Band (GHz)	Observing Date	$t_{obs}{}^{d}$ (hours)	Non-Operative telescopes^{e}
I	BB229A	8.4 (X)	2007/01/26	2	EF, GB, Y27
I	BB229A	15.3 (U)	2007/01/26	8	EF, GB, Y27
I	BB229A	22.2 (K)	2007/01/28	10	–
II	BB255B	8.4 (X)	2008/05/02	2	EF, GB, Y27, NL
II	BB255B	15.3 (U)	2008/05/02	8	EF, GB,Y27, NL
II	BB255B	22.2 (K)	2008/05/03	10	NL
III	BB255C	8.4 (X)	2009/04/10	2	EF, GB, Y27, MK
III	BB255C	15.3 (U)	2009/04/10	8	EF, GB, Y27, MK
III	BB255C	22.2 (K)	2009/04/08	10	SC
IV	BB364A	22.2 (K)	2015/12/21	10	Y27
IV	BB364B	22.2 (K)	2015/12/27	10	EB,Y27

[d] The Observation time length at different bands at different epochs

[e] The antenna not used from the antenna list presented in table.3.1

3.3. Data Reduction

The data is edited and calibrated using ParselTongue run a Python-based script called "BeSSeL-master.2.2.0.py" (privately shared). The script allow the sequential execution of programs from the Astronomical Image Processing System (AIPS), with each step of the calibration correcting either phase or the amplitude of the data.

The first part of the script performs a number of tasks which involves phase corrections only. To do this, the script automatically downloads the latest EOP file and the TECOR files (see below) and applies them to the specified input data. It also performs the tropospheric corrections using the ATMOS.FITS file generated from the geodetic-block analysis, applies parallactic angle corrections and shifts source positions if required. For clarity, we now discuss the tasks involved in each part of the script.

The AIPS task 'TECOR' corrects for the delay caused by the ionosphere. The ionosphere has variations caused by free electrons which absorb, refract and rotate the incoming electromagnetic wave. These variations are measured by the Global Positioning System (GPS[3]) at particular times. The models for all times are approximated from the data, and is accessed from Crystal Dynamics Data Information System (CDDIS) data archive [4]. The task 'TECOR' examines the data to obtain information such as the observation dates and antennas used. The task then reads a set of maps of ionospheric electron content that covers the time range of the observations and uses this data to calculate the ionospheric delays. The estimated ionospheric corrections are written into a new CL table. The CL table is incremental such that, every new CL table contains the information from the previous tables.

The Earth Orientation Parameters EOPs correction accounts for the slow variation of the Earth's orientation and the sky rotation with the respect to the antennas during the observations. The correct EOPs are downloaded automatically by the script and the corresponding corrections written into a new CL table (see Fig.3.3.2). The parallactic angle corrections and source position shifts (if specified) are also applied to the data at this point. For instance, in our data, we realized the phase-calibrator position used in the correlator for the first epoch (2007 January) and fourth epoch (2015 December) varied slightly to the position of the other epochs (i.e. 2008 May, 2009 April) by $-0.036\,\mathrm{mas}$ and $-0.0216\,\mathrm{mas}$ in the right ascension and declination directions, respectively for the first epoch, and by $1.044\,\mathrm{mas}$ in the right ascension and $-0.0684\,\mathrm{mas}$ in declination for the fourth epoch. Applying the correction for the change in angular size of circles of constant right ascension by a factor of cos(Dec), the

---

[3] https://en.wikipedia.org/wiki/Global_Positioning_System

[4] http://cddis.nasa.gov

position shifts at epoch I is shifted by $-0.0129\,\mathrm{mas}$ and $-0.0216\,\mathrm{mas}$ in right ascension and declination, respectively, and at epoch IV by $0.373\,\mathrm{mas}$ and $-0.0684\,\mathrm{mas}$ in right ascension and declination, respectively. From the observations in epoch IV, we also noted the position of quasar 0948+6848 to be off by $-0.0129\,\mathrm{mas}$ in right ascension.

The second part of the script involves a correction for the sampler bias, that affects the amplitude of the data only. The bias comes from the digital samplers at the antennas, which often have a difference in their ideal theoretical values and the corresponding voltage threshold levels. Typically, the observed visibilities (see Eqn. 2.2.1) are obtained from the Fourier transform of cross-correlation function $\mathrm{C_{i,j}}(\tau)$, such that

$$\mathrm{C_{i,j}}(\tau) \leftarrow \mathrm{FT} \rightarrow \mathrm{V^{obs}_{i,j}}(\nu). \tag{3.3.1}$$

The task ACCOR normalizes the cross-correlation function by dividing it with the geometric mean of the value of the correlation function at $\tau = 0$ as

$$\rho_{\mathrm{i,j}}(\tau) = \frac{\mathrm{C_{i,j}}(\tau)}{\sqrt{C_{i,i}(\tau=0).C_{j,j}(\tau=0)}}. \tag{3.3.2}$$

The cross-correlation output is a gain of $\sim$1 (See Fig. 3.3.1b). These results are written into a solution (SN) table 1 before transferring it to a new CL table.

To obtain physical results, the script performs amplitude calibration by multiplying the normalized visibilities by the geometric mean of SEFD (System Equivalent Flux density) of each antenna pair. The SEFDs are estimated from antenna gains (effective aperture areas) and system noise temperatures as,

$$|\mathrm{g}| = \sqrt{\mathrm{SEFD}} = \left(\frac{2\mathrm{K_B T_{sys}}}{\mathrm{A_e}}\right)^{\frac{1}{2}}. \tag{3.3.3}$$

For each baseline $\mathrm{K_B}$=$1.38\times10^3\,\mathrm{Jy\,m^2/K}$ is the Boltzmann constant, A_e is the effective aperture area while $\mathrm{T_{sys}}$ is the system noise temperature. The antenna gain values are recorded in the GC (gain curve) extension table. This table contain values of $\mathrm{A_e/2K_B}$ as a function of elevation because the effective aperture area depends on the amount of gravitational force distortions. The $\mathrm{T_{sys}}$ is recorded in the TY extension table which has values of the system noise temperature as a function of time. With TY, GC and SU extension prepared, the task APCAL calculates the SEFDs and write them in the SN extension table 2 before being transferred to a new CL table by the CLCAL task (see Fig.3.3.1).

After determining the amplitude calibration corrections, the third part of the script deals with corrections that involve phase delay calibration and the short term fluctuations. These instrumental phase delays cause steep phase slopes within one intermediate frequency band (IF) and phase jumps between the IFs. The aim of the correction is to flatten the phases within each IF. This step is called the manual phase calibration, done on the best delay calibrator source specified in the input. For the delay calibration, we observed three strong calibrator sources (3C345, DA 193 and J1048+7143). However, only one strong calibrator is needed, the one with best solutions on a short time interval and observed with all antennas. The task "FRING" uses the selected calibrator for the manual phase calibration, and the corrections are written in an SN table before being transferred to a new CL table (see Fig.3.3.2).

The script then solves the bandpass roll off problem by chopping off the bad edges i.e. channel 1–7 for lower edge and channel 123–128 for the upper edge at epochs I–III, channel 1–13 for lower edge and channel 1012–1024 for the upper edge at epoch IV in K-band, and channel 1–16 in X- and U-bands. To establish the correct Doppler velocity scale for the water maser emission at K-band, the script runs CVEL on the specified line source using the appropriate input velocity for each sub-band (i.e. IF 1 = 447.86, IF 2 = 340, IF 3 = 232.14 and IF 4 = 124.28 $\mathrm{km\,s^{-1}}$ at epochs I–III, and IF 1=220.00, IF 2=−211.44 at epoch IV).

At this point, we have no phase offsets between IFs and no slopes in the phase as a function of frequency over the full bandwidth. The aim of this step which is often referred to as fringe fitting is to remove the global frequency–dependent phase errors(delay) and time–dependent phase errors (rate) for the complete time range. These phase errors cannot be corrected with a strong, yet distant calibrator source, this is why the phase-reference source M 81* is located within a degree from the target sources. The script runs the task FRING which produces an SN table, containing the corrections which are transferred to a new CL table.

The calibration is finished at this point, and the corrections stored in tables must now be applied to the data. The script runs the task SPLIT creating new files for each source and applies the highest numbered CL and flag (FG) tables on the individual continuum and spectral line sources. FG tables specify data that was identified as faulty during the calibration process and that are not to be used further. The continuum sources are averaged over all channels, excluding the band edge channels listed above. For the spectral line data, SPLIT retains their full resolution i.e. without channel average. The imaging is done manually using AIPS task “IMAGR” .

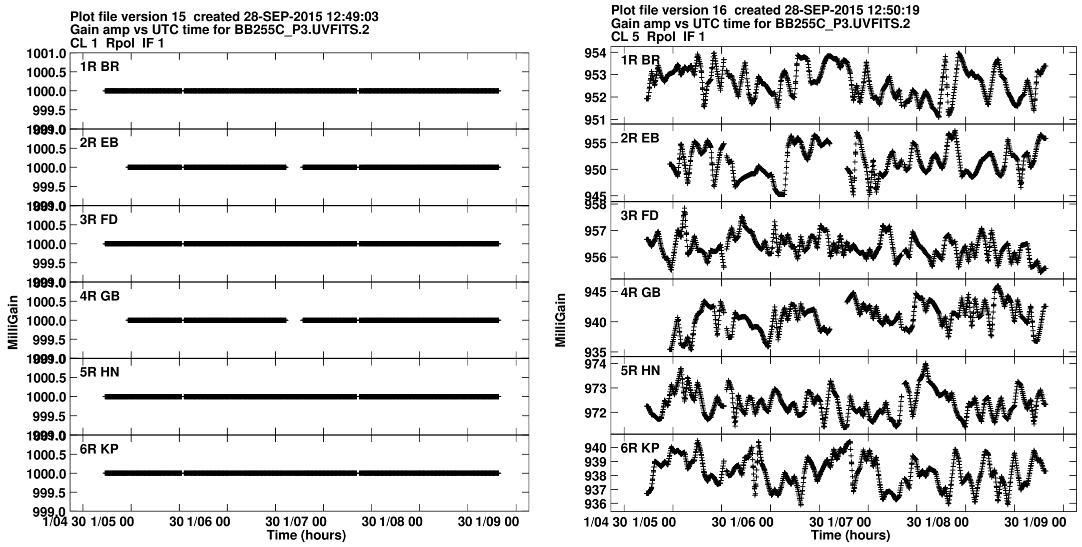

(a) Before amplitude correction

(b) After applying “ACCOR”

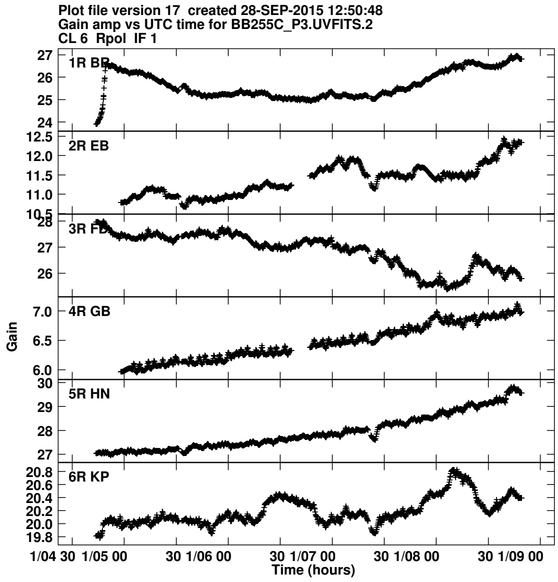

(c) After applying “APCAL”

Figure 3.3.1.: Examples of the different CL-tables showing the amplitude corrections for a data set BB255C at K-band. The figures show a part of the observing time at one polarization at IF 1, for a subset of antennas.

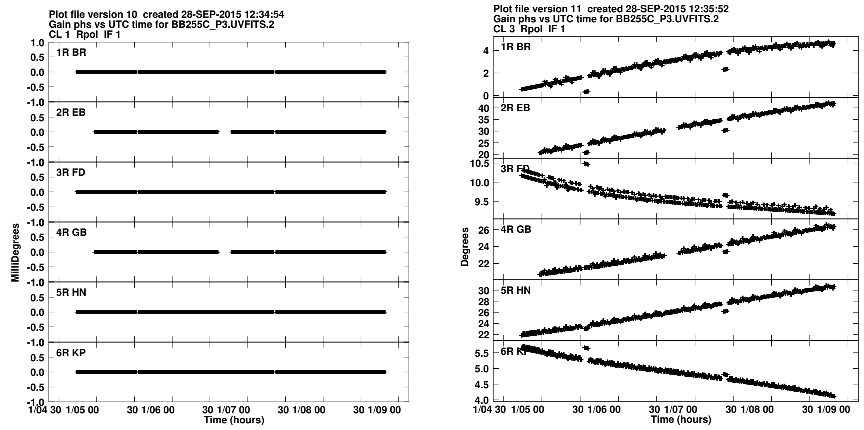

(a) Before calibration

(b) After Ionospheric and Earth Orientation correction

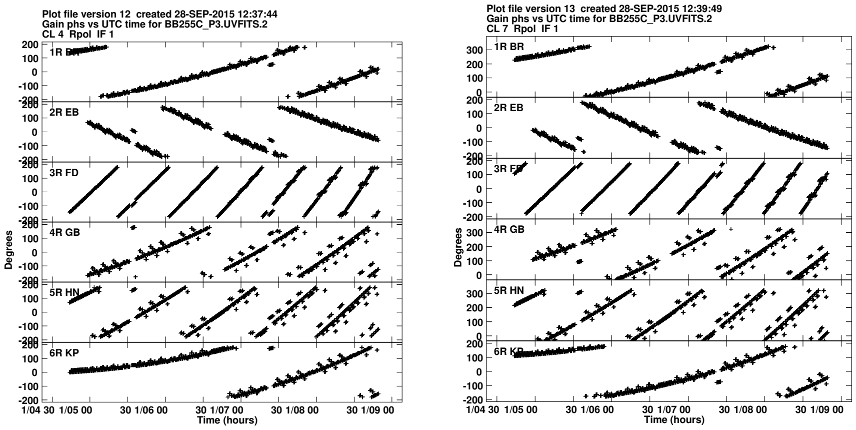

(c) After Atmospheric and Parallactic angle correction

(d) After manual phase calibration

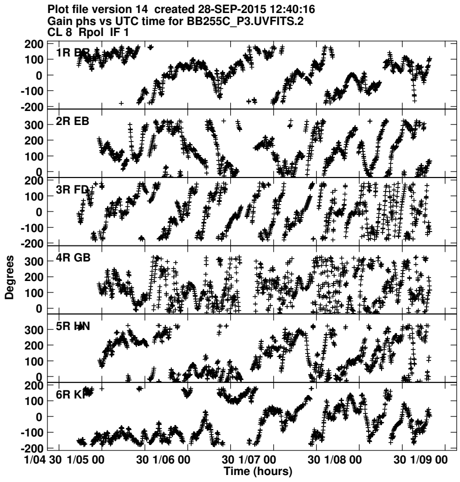

(e) After fringe fitting

Figure 3.3.2.: Examples of the different CL-tables showing the phase corrections for a data set BB255C at K-band. The figures show a part of the observing time at one polarization at IF 1, for a subset of antennas.

4. M 81 Proper Motion

In this chapter, we check the structural stability of the phase-referencing source (M 81*), we also present the μas VLBI astrometry results by deriving the proper motion of M 81, clarify the space-velocity transformation technique and derive the space motion of M 81 relative to the Milky Way galaxy.

4.1. Introduction

The galaxy M 81 (NGC 3031, 0951+693), located at a distance of 3.63±0.34 (Freedman et al., 1994) is a grand-design spiral, that shares some characteristics with radio galaxies and quasars (Bietenholz et al., 1996). It resembles the Milky Way galaxy in type, size and mass. It is also known to host a nuclear radio source often referred to as M 81*, which is believed to be a scaled up version of Milky Way's nuclear source (Sgr A*). M 81* is most likely associated with a supermassive black hole in the galaxy's gravitational center (Bietenholz et al., 2000), whose mass is estimated as $7\times10^{7}\mathrm{M}_{\odot}$ (Devereux et al., 2003). The nucleus has a high X-ray luminosity ($\sim1.7\times10^{40}\,\mathrm{erg\,s^{-1}}$; Elvis and van Speybroeck, 1982) and a nonstellar UV continuum (Ho et al., 1996). Its optical spectroscopy show a broad Hα line (Peimbert and Torres-Peimbert, 1981) and double-peaked broad other emission lines (e.g. Lyα and Mg II lines). These properties are often associated with jets in galaxies that host active galactic nucleus (AGN; e.g.Seyfert, 1943, Bower et al., 1996).

As mentioned in section 1.1, successful VLBA phase-referencing observations of M 81 are possible by choosing its compact radio core as a target. In this project, we are using M 81* and three background quasars to derive the proper motion of the M 81 Galaxy. The M 81 radio core is used as the phase-referencing source throughout the study, because it is compact and has a relatively high flux density. This implies that a clear understanding of the nature of the M 81* is of great importance in this work. In the following subsections, we discuss its properties.

4.1.1. Apparent source size

M 81* is considered one of the most compact nuclei observed in active galaxies. A 12 year long campaign of the VLBI observations found it to be extremely stable in its size and orientation at a given observing frequency (Bietenholz et al., 2004). Its radio morphological structure show a stationary feature identified as the core, with a one-sided jet to the north-east

(Bietenholz et al., 2000, Martí-Vidal et al., 2011c). The core size is observed to be frequency dependent i.e. decreases with increase in frequency, obviously larger at lower frequencies. The apparent major axis source size, Θ, is estimated to be 1.48 mas at 1.7 GHz, 0.8 mas at 2.3 GHz, 0.5 mas at 8.4 GHz, 0.18 mas at 22 GHz, and 0.09 mas at 43 GHz (1 mas$\approx$3600 AU; Ros and Pérez-Torres, 2012 and references there in).

A linear fit to the size estimates reveals a strong dependence on the observing frequency, following a frequency-size dependent power-law $\Theta \propto \nu^{(-0.88\pm0.04)}$ between 1.7 GHz and 43 GHz (Ros and Pérez-Torres, 2012). A similar dependence was observed in Sgr A* whose size is proportional to ν^{-2} (for frequencies below 20 GHz), which is thought to be the result of interstellar scattering, since Sgr A* is known to be largely hidden behind scattering clouds of gas (e.g. Backer, 1994, Marcaide et al., 1992). Bietenholz et al. (1996) suggest that the frequency dependence of M 81* is intrinsic to the source. This claim is supported by two facts; first, although SN 1993J is located at the disc of M 81, its VLBI observations do not show any scattering effects. Secondly, interstellar scattering would be expected to produce an approximately ν^{-2} size dependence as seen for Sgr A*.

4.1.2. Peak flux density variation

Several studies have reported peak flux density variability of M 81* i.e. in the X-ray regime (long-term; Ishisaki et al., 1996 and short-term; Markoff et al., 2008), the millimeter regime (Schödel et al., 2007, Markoff et al., 2008) and the radio regime (e.g. Ho et al., 1999a, Martí-Vidal et al., 2011c). For instance, the VLA observations of M 81* at 8.4 GHz, show strong flux density fluctuations with timescales of less than a few weeks. Its flux densities varied with time by up to a factor of 2 from 81 mJy to 189 mJy, with a mean flux of 127 mJy (Bietenholz et al., 2004). The mean flux translates to a radio luminosity of only $\sim 10^{37.5}\,\mathrm{erg\,s^{-1}}$ for a radio frequency range up to 100 GHz, which makes the core of M 81 to be classified as a low-luminosity AGN (Bietenholz et al., 1996).

The flux density variability among AGNs is believed to be either intrinsic or extrinsic in nature. For M 81*, the variability is argued to be intrinsic to the source (e.g. Bietenholz et al., 2004). We have previously presented arguments for the intrinsic nature based on the frequency-size dependence of this source. Rickett (1986) continues the argument, arguing that for M 81* the flux density variations due to extrinsic variability causes (such as interstellar medium induced refractive index and scattering medium fluctuations) can only account of at most a few percent at 8.4 GHz. This is clearly not the case for M 81 core, whose flux density variations are much larger ($\sim$200%). This implies that the flux variability is intrinsic to M 81*.

4.1.3. Core location and jet motion

Reuter and Lesch (1996) obtained a spectrum of M81* from the radio to the mm-regime. The spectrum is best described by a power-law of the form $S_\nu \propto \nu^{1/3} e^{-(\nu/\nu_c)}$ which is an inverted spectrum with a turnover frequency of ν_c=200 GHz. This kind of spectrum best fits a core-jet source, for which the core exhibits a flat or inverted spectrum and the jet exhibits a steep spectrum. This confirms the core-jet nature of M81*, with the "core" being an unresolved point source even at 43 GHz (Ros and Pérez-Torres, 2012).

The location of the brightness peak relative to the stationary core is reported to be variable both in time and frequency. The brightness peak generally shifts towards the south-west extremity with increasing frequency (Bietenholz et al., 2004). The south-west extremity position is largely frequency-independent, suggesting a hard edge to the emission region at that point. This is considered the best estimate for the core location, confirming the brightness peak of M81* to be unambiguously identified with the jet rather than the core. Since the location of the brightness peak seems to be well-behaved function of frequency, its possible to extrapolate it to at least $\nu \sim 200$ GHz, the turnover frequency, and use the extrapolated position for a best estimate of the core location (Bietenholz et al., 2004).

4.1.4. Polarization

Brunthaler et al. (2006), using archival VLA observations of M81* spanning from 1994 to 2002, reported circular polarization at 4.8, 8.4 and 15 GHz, without detection of linear polarization. Several mechanisms have been put forward to explain the circular polarization detections in extragalactic sources, e.g. synchrotron emission (intrinsic circular polarization; Roberts and Komesaroff, 1965, Legg and Westfold, 1968), interstellar propagation effects (Macquart and Melrose, 2000), Faraday conversion (Pacholczyk, 1977, Jones and Odell, 1977) and gyro-synchrotron emission (Ramaty, 1969).

The fractional circular polarization of M81* shows significant variability on timescales of a few weeks, which is not correlated with the variability in the total intensity. However, it is remarkable that, despite the strong variability, all observations find the sign of the circular polarization to be always positive at all frequencies. The spectrum of the fractional circular polarization is inverted with values between 0.4 and 2 whenever polarization was detected at more than one frequency. Based on the range of observed spectral indices, their inverted spectra and fractional circular polarization levels, the plausible mechanism responsible for the circular polarization of M81* and Sgr A* is Faraday conversion of linear polarization to circular polarization caused by the lowest energy relativistic electrons (Brunthaler et al., 2006).

The polarization properties of M 81* are strikingly similar to the properties in Sgr A* which are (i) the circular polarization is variable on timescales of days to months, (ii) the sign of the circular polarization stayed constant over the entire time range of almost 20 years, and (iii) the average spectrum of circular polarization is inverted (Bower et al., 2002). This similarity further supports the hypothesis that M 81* is a scaled up version of Sgr A*. However, polarization phenomenology of Sgr A* and M 81* strongly contrasts that found in most AGN core/jet sources in which linear polarization often exceeds circular polarization by a large factor (e.g. Rayner et al., 2000).

4.2. Results

As already mentioned, M 81* was observed as a phase-referencing source for the multi-frequency VLBA observations of background quasars. This allows us to obtain very accurate relative positions to the three quasars at frequencies 8.4, 15.3 and 22.2 GHz. The sources are very close in the sky to the M 81*, with a separation of within 1° as seen in fig. 3.2.1. The small separation reduces significantly the systematic sources of errors when determining the relative positions. The three background quasars were assumed to be stationary on the sky, considering their large distance.

4.2.1. Core location Estimate

The brightness peak position of M 81* has been reported not to coincide with the core, and also tends to vary with frequency (e.g. Bietenholz et al., 2004). The core location, rather than the brightness peak is important in determining the proper motion. The previous core position of M 81* was estimated from 8.4 GHz observations as the most stationary point in the brightness distribution, using the geometric center of SN 1993J as the astrometric referencing point. The core position was estimated to be R.A.=$9^{\mathrm{h}}55^{\mathrm{m}}33^{\mathrm{s}}.173063$, Dec.=$69^{\circ}03'55''.061464$ (J2000, Bietenholz et al., 2000, Bietenholz et al., 2004), and presumed to be constrained to within ± 0.2 mas.

From the phase-referencing technique, we obtain the proper motions at any frequency from the position offsets of the quasars relative to M 81*. While, the quasars can also have small core shifts, these should be in random directions. The position of the brightness peak position is frequency dependent, with the 22 GHz peak position to be considered closest to the stationary core location. We obtained the difference in the position offsets of quasars at 8.4 and 15 GHz against their 22 GHz offsets. These differences in right ascension and declination are averaged for the three quasars at each frequency at a given epoch (see Table. 4.1). We then plot the relative average positions of their brightness peak at each epoch and frequency in figure 4.2.1. The plot shows offsets of the three quasars at different frequencies to be only in one direction. This is due to the difference in the peak brightness position of the phase-referencing source, M 81*. Figure 4.2.1 also shows the core shift of the brightness peak relative to 22 GHz brightness peak position to be somewhat variable at each frequency, moving to the south-west direction with increasing frequency, in agreement with Bietenholz et al. (2004). This shows that the source structure is stable, and we thus dropped the 8.4 and 15 GHz observations in the later epochs.

Table 4.1.: The averaged position offsets of the brightness peak of M 81*

Date	Average Position Offset (mas)			
	15.3 GHz		8.4 GHz	
	$\triangle\alpha$	$\triangle\delta$	$\triangle\alpha$	$\triangle\delta$
2007 Jan 26	0.050 ± 0.006	0.018 ± 0.007	0.108 ± 0.006	0.062 ± 0.007
2008 May 02	0.054 ± 0.011	0.026 ± 0.014	0.117 ± 0.021	0.070 ± 0.014
2009 Apr 10	0.044 ± 0.010	0.017 ± 0.015	0.103 ± 0.009	0.067 ± 0.014

The right ascension ($\triangle\alpha$) and declination ($\triangle\delta$) offsets to the position of the brightness peak of M 81* derived from the average position offsets of the three quasars relative to their 22 GHz brightness peak position.

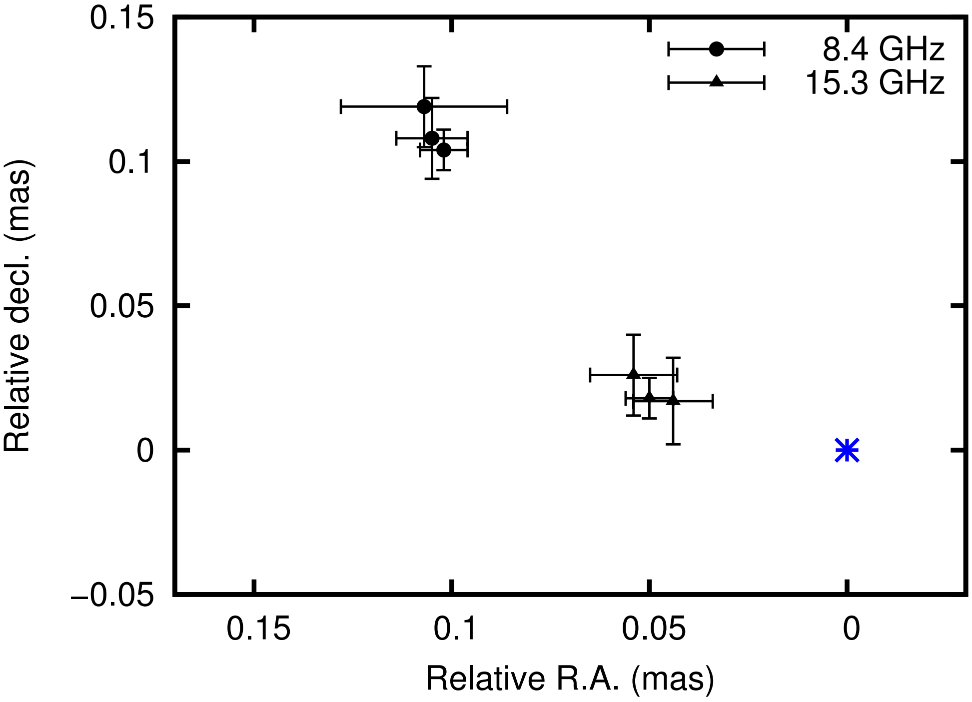

Figure 4.2.1.: The figure shows the core-shift of M 81* peak brightness distribution relative to the 22.2 GHz brightness peak position (marked by a blue asterisk symbol).

4.2.2. Morphology of continuum sources

The morphological structures of M 81* and the three quasars are shown in Figs. 4.2.2, 4.2.3,4.2.4, & 4.2.5. The individual figures show the three representative images of the sources taken on 2009 April, at frequencies of 8.4, 15, and 22 GHz.

Fig.4.2.2 shows the three representative images of the core of M 81. The images are made with the IMAGR task in AIPS, using uniform weighting and convolved with the restoring beam determined by IMAGR of ∼1.3×1.0 mas, ∼0.9×0.7 mas and ∼0.7×0.5 mas at position angles 50°, 51°, 51° east of north at 8.4, 15.3 and 22.2 GHz respectively. The FWHM of the original restoring beam is indicated at the lower left corner. From the images, the source is marginally resolved with a simple brightness distribution. The 8.4 GHz image shows the source to be elongated along the southwest-northeast axis in agreement with Bietenholz et al. (2000, 2004). The rms of noise for the images shown below are 0.3, 0.5 and 0.8 mJy/b at 8.4, 15.3 and 22.2 GHz, respectively.

As discussed above, the source is known to have highly variable radio emission especially at frequencies greater than 5 GHz. For instance, at 15 GHz, M 81* has an average flux density of 116 mJy (Pooley, 2011) with typical flares reaching 150 mJy (Ho et al., 1999b). However, in 2011 M 81* flares were reported to have exceeded the typical strengths, increasing from a flux density of 140 mJy on 2011 August 24, to 261 mJy on 2011 August 27 and 321 mJy on 2011 September 1 (King et al., 2016). King et al. (2016) also reported strong flares in X-ray emission. Moreover, for the first time, they report the detection of a discrete optically thick knot at 23 GHz over four epochs (17 Sept, 20 Sept, 26 Sept and 2 Oct 2011). The knot is reported to move radially from the center of the radio core with a projected velocity of $\upsilon_{\mathrm{app}}/c=0.51\pm0.17$. VLBA observations at 15 and 23 GHz nearly 3 months later (2012 January 16), found both the discrete knot and the core to be optically thin, $\alpha < 0$, and a significant drop in flux densities, indicating that the flare had stopped. Our VLBA observations at 22 GHz conducted in 2015 December 21 & 27 do not show any signs of a discrete knot at a noise level of 0.5 mJy/beam.

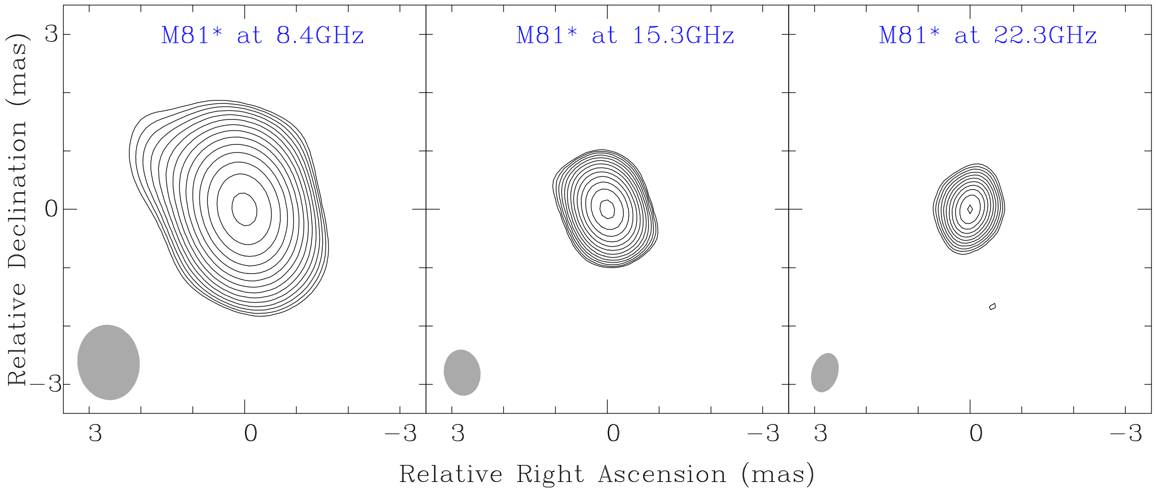

Figure 4.2.2.: The images of M 81* obtained on 2009 April at observing frequencies 8.4, 15.3 and 22.2 GHz. The contour values are spaced in $\sqrt{2}$ intervals starting at 1.0, 1.6 and 2.6 mJy which is 3×rms level, with a peak brightness of 99.3±0.3, 113.9±0.2 and 86.0±0.3 mJy/beam at 8.4, 15.3 and 22.2 GHz, respectively.

Fig.4.2.3 shows representative images of the quasar 0948+6848 observed during the third epoch. The source has a double component structure made up of a southern and a northern source. The flux densities of the two components were observed to vary relative to each other (see Tables.A.3, A.2, A.1). The northern component in the 2009 epoch show a steep spectrum with integrated flux densities of 29.0±0.5 mJy at 8.4 GHz, 20.2±1.3 mJy at 15.3 GHz and 12.2±2.0 mJy at 22.2 GHz as it becomes more resolved. On the other hand, the southern component at the same epoch has a flat spectrum with 24.1±0.3 mJy, 35.8±0.6mJy, and 29.8±0.6 mJy at 8.4, 15.3 and 22.2 GHz, respectively.

This shows that quasar 0948+6848 hosts a jet structure with a south-north orientation. During the observations, the quasar does not show strong morphological structure changes at a given frequency, a likely sign of slow jet motion. However, across the frequencies, the northern component was significantly resolved, which could account for the absence of observed structures at higher frequencies. This implies that, the northern source component must be the jet, while the core location is expected to be at the southern component, which remains very compact and unresolved even at higher frequencies.

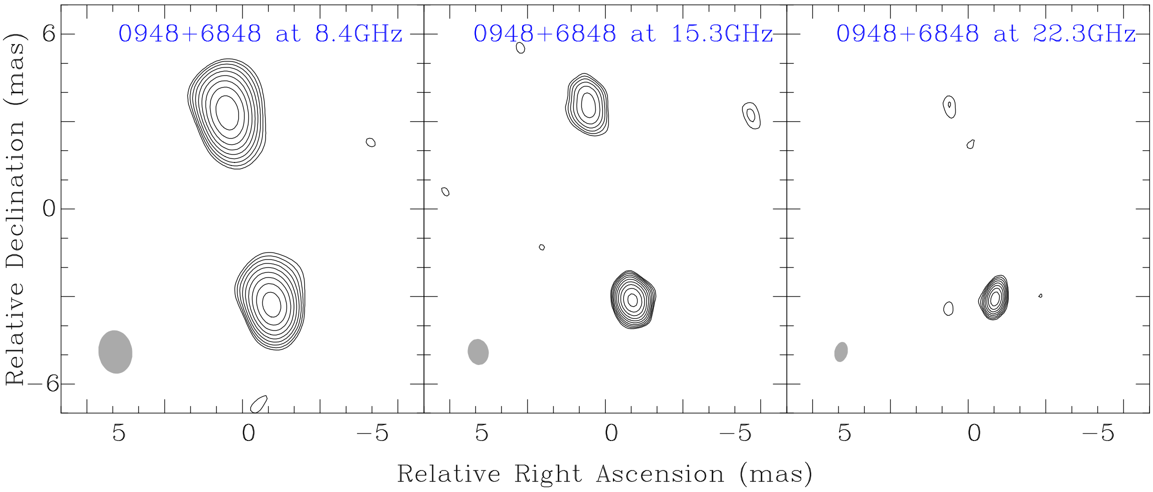

Figure 4.2.3.: Images of quasar 0948+6848 on 2009 April at observing frequencies 8.4, 15.3 and 22.2 GHz. The contour values are spaced in $\sqrt{2}$ intervals starting at 1.0, 1.2 and 1.5 mJy which is 3×rms, with a core peak brightness of 21.8±0.2, 32.1±0.3 and 27.4±0.2 mJy/b at 8.4, 15.3 and 22.2 GHz, respectively.

Fig.4.2.4 shows representative images of the quasar 0945+6924. The images show a central source with an unresolved northern elongation at 8.4 GHz. The elongation structure is completely resolved at 15.3 and 22.2 GHz 3σ noise level. The main component remains compact and unresolved across the frequencies and was considered the image center and used to derive the position offsets. The integrated flux density of the central component on 2009 April was 8.2±0.2 mJy, 8.6±0.4 mJy and 7.4±0.5 mJy at 8.4, 15.3, and 22.2 GHz, respectively.

Fig.4.2.5 shows representative images of quasar 1004+6936 observed during the third epoch. The source is generally simple and compact. The integrated flux densities are 21.2±0.3 mJy, 25.3±0.5 mJy, and 18.1±0.5 mJy at 8.4, 15.3 and 22.2 GHz, respectively.

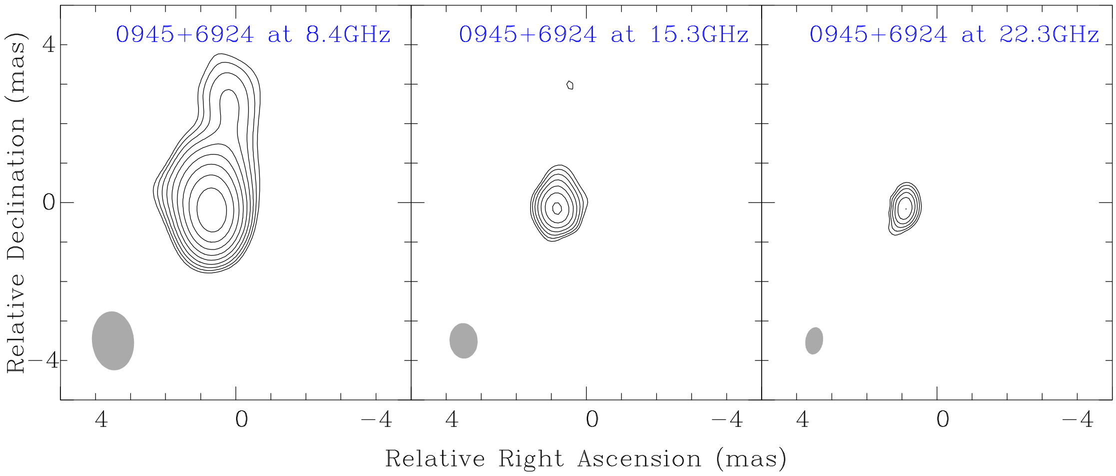

Figure 4.2.4.: Images of quasar 0945+6924 on 2009 April at observing frequencies 8.4, 15.3 and 22.2 GHz. The contour values are spaced in $\sqrt{2}$ intervals starting at 0.3, 0.6 and 0.6 mJy which is 3×rms, with a peak brightness of 6.2±0.1, 6.7±0.2 and 4.6±0.2 mJy/b at 8.4, 15.3 and 22.2 GHz, respectively.

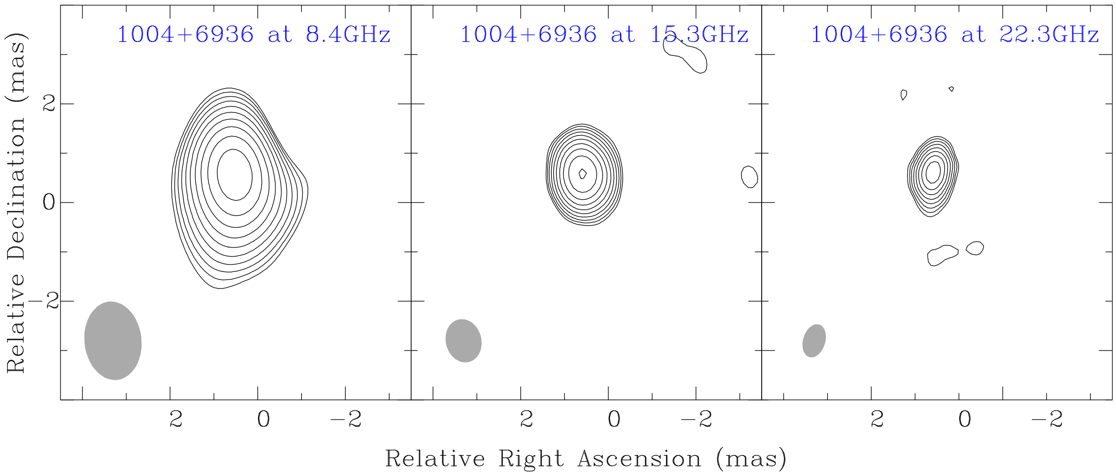

Figure 4.2.5.: Images of quasar 1004+6936 on 2009 April at observing frequencies 8.4, 15.3 and 22.2 GHz. The contour values are spaced in $\sqrt{2}$ intervals starting at 0.7, 0.9 and 1.0 mJy which is 3×rms, with a peak brightness of 22.5±0.2, 22.7±0.2 and 14.7±0.2 mJy/b at 8.4, 15.3 and 22.2 GHz, respectively.

4.2.3. Proper Motion results

The proper motion of M 81 relative to the three background quasars was successfully derived at 8.4, 15.3 and 22.2 GHz. This involves obtaining the position offsets of a given quasar relative to M 81* at multiple times, and fitting a straight-line motion to the data. The linear fit errors can be unrealistically small due to low number statistics. The proper motion measurements results are presented as in figures 4.2.6,4.2.7, and 4.2.8.

The 8.4 GHz proper motion

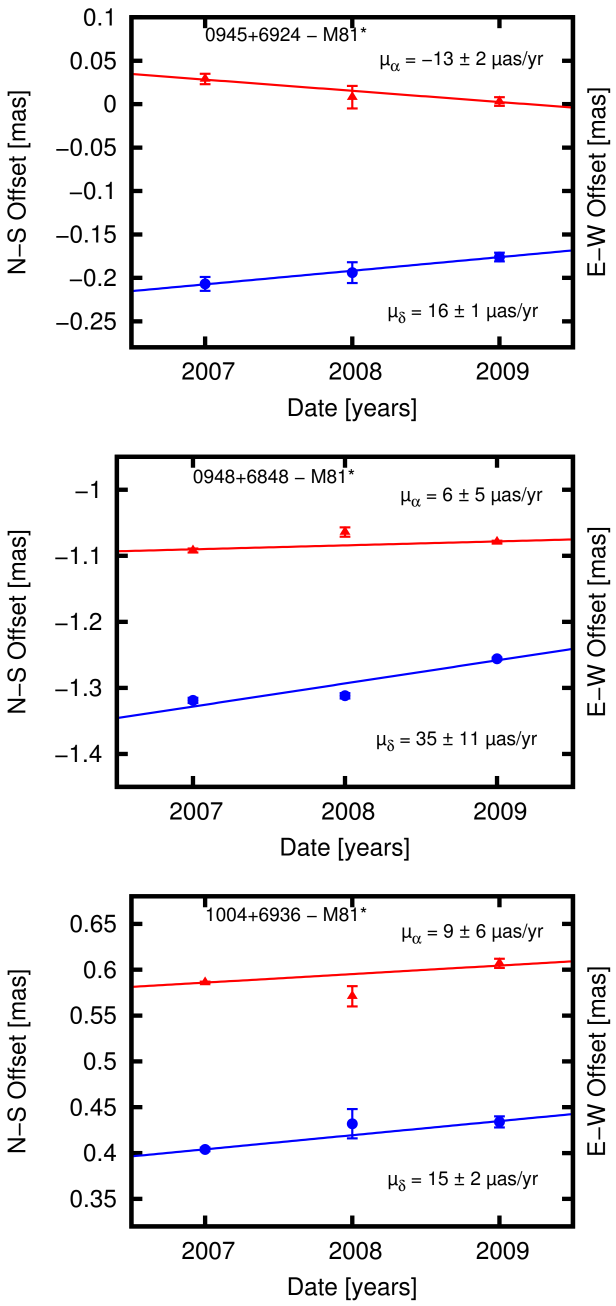

Figure 4.2.6.: The 8.4 GHz position of the quasars (0945+6924, 0948+6848, 1004+6936) relative to the phase-reference source M 81*. The east-west positions are marked with red triangles and north-south with blue circles. The lines show the weighted linear fit to the data points.

The 15.3 GHz proper motion

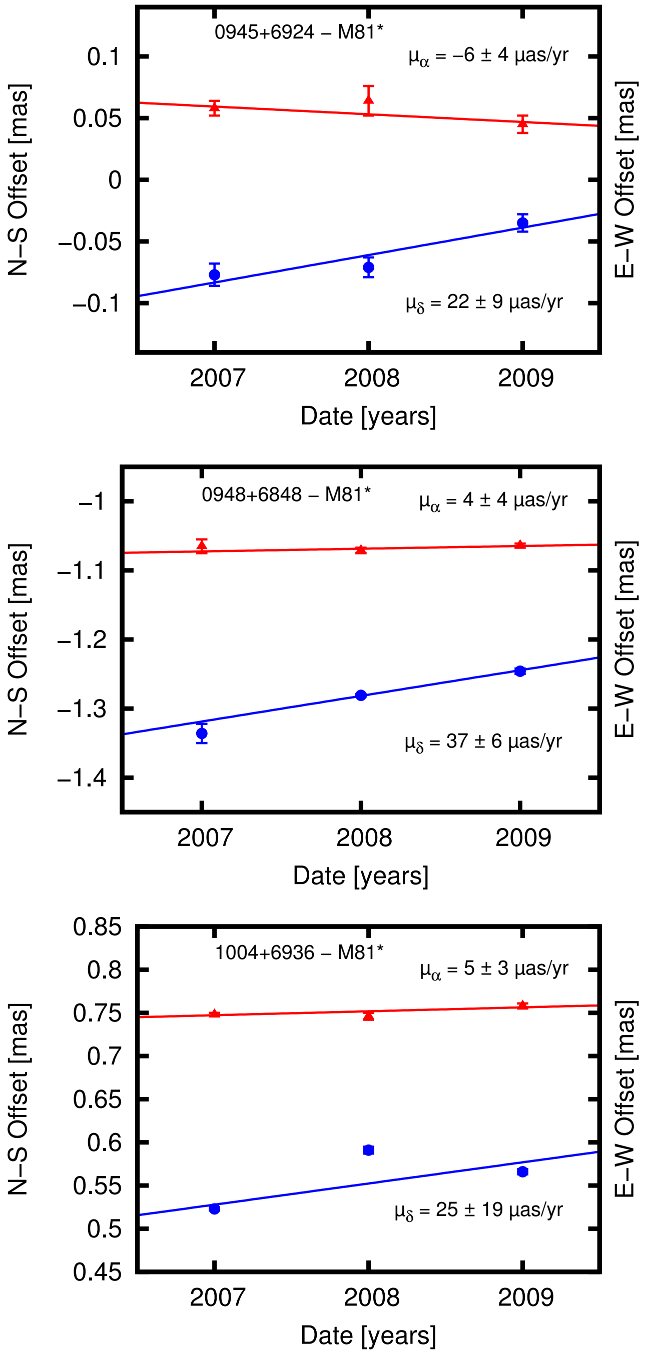

Figure 4.2.7.: The 15.3 GHz position of the quasars (0945+6924, 0948+6848, 1004+6936) relative to the phase-reference source M 81*. The east-west positions are marked with red triangles and north-south with blue circles. The lines show the weighted linear fit to the data points.

The 22.2 GHz proper motion

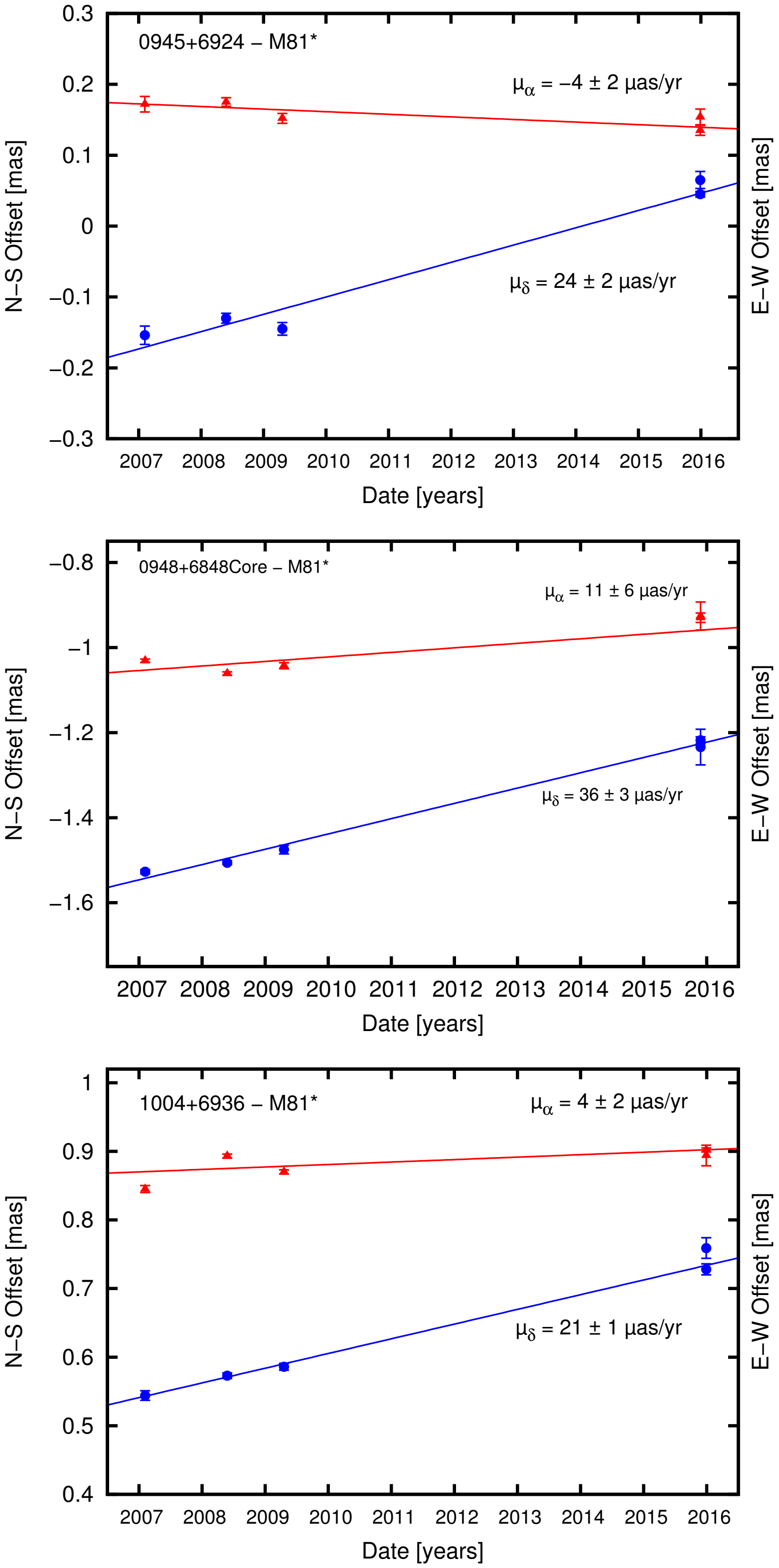

Figure 4.2.8.: The 22.2 GHz position of the quasars (0945+6924, 0948+6848, 1004+6936) relative to the phase-reference source M 81*. The east-west positions are with red triangles and north-south with blue circles. The lines show the weighted linear fit to the data points.

Table 4.2.: Summary of the observed proper motions of quasars

Quasars	Observed proper motion					
	8.4 GHz		15.3 GHz		22.2 GHz	
	μ_α (μas yr^{-1})	μ_δ (μas yr^{-1})	μ_α (μas yr^{-1})	μ_δ (μas yr^{-1})	μ_α (μas yr^{-1})	μ_δ (μas yr^{-1})
$0945+6924$	-13 ± 2	16 ± 1	-6 ± 4	22 ± 9	-4 ± 2	24 ± 2
$0948+6848$	6 ± 5	35 ± 11	4 ± 4	37 ± 19	11 ± 6	36 ± 3
$1004+6936$	9 ± 6	15 ± 2	5 ± 3	25 ± 19	4 ± 2	21 ± 1

The proper motions of the individual quasars agree very well within the errors across the observing frequencies (see Table. 4.2). Moreover, the east-west motions and north-south motions of quasars 0945+6924 and 1004+6936 agree within the errors across the observing frequencies. However, if one splits up quasar 0948+6848 offsets to its north-south and east-west components, one realizes the deviation is large in the south-north direction, i.e. a factor of ~1.5 larger than that of other two quasars. As seen from its morphological structure in Fig.4.2.3, quasar 0948+6848 hosts a south-north oriented jet structure. We can therefore argue that the peak brightness position used in obtaining the position offsets does not coincide with the stationary core position. This implies that the observed motion has a contribution from the internal jet motion. If we take this as a plausible explanation of the unusually high northern motion compared to the other quasars, we exclude its motion when deriving the M 81 galaxy proper motion because our measurement is contaminated.

The derived proper motion of M 81 is the averaged motion of quasars 0945+6924 and 1004+6936. Given their distances, the two background quasars are considered stationary. This allows a direct measurement of M81's motion. The rectilinear fit errors were considered non-representative due to the few fitting points from the few epochs. We therefore derive the M 81 proper motion errors from the standard deviation of the fit results. The standard deviation is given by

$$\sigma_N = \sum_{i=1}^{N} \sqrt{\frac{(x_i - \bar{x})^2}{N-1}}, \tag{4.2.1}$$

where x_i are the individual measurements and $\bar{x}$ is the arithmetic mean. Usually, a standard deviation is reliable only for a large number of measurements N. In our case, the number of observations is very small. Based on the number statistics, the derived standard deviation can be misleading. For instance, two measurements may coincidentally be very close, thereby yielding a very small error, even if their intrinsic error is much larger. However, the derived standard deviation errors seem more representative, always better in the declination than in right ascension.

The derived motions are $\mu_\alpha = 2 \pm 15.5\,\mu\mathrm{as\,yr^{-1}}$ and $\mu_\delta = -15.5 \pm 0.7\,\mu\mathrm{as\,yr^{-1}}$ at 8.4 GHz, $\mu_\alpha = 0.5 \pm 7.8\,\mu\mathrm{as\,yr^{-1}}$ and $\mu_\delta = -23.5 \pm 2.1\,\mu\mathrm{as\,yr^{-1}}$ at 15.3 GHz, $\mu_\alpha = 0 \pm 5.7\,\mu\mathrm{as\,yr^{-1}}$ and $\mu_\delta = -22.5 \pm 2.1\,\mu\mathrm{as\,yr^{-1}}$ at 22.2 GHz. The general observed motion of M 81 is towards the southern direction. In our analysis, we adopt the 22 GHz values as the representative for the proper motion of M 81 for the following reasons; 1) the position of the brightness peak is frequency dependent with 22 GHz closest to the core, 2) systematic effects on the motions are smallest at higher frequencies, and 3) a higher number of observation epochs at that frequency. However, this proper motion results are largely dependent on the 2015 position offsets. With the jet activity reported in our phase-referencing source, M 81*, in 2011, we cannot ascertain the effect of that activity to the position offsets derived from the fourth epoch. Nevertheless, the subsequent observations that are scheduled for 2016 and 2017, will help to illuminate the effect if any, of the jet activity.

4.3. Discussion

4.3.1. Space Motion of M 81

The proper motion $\mathbf{v}_{\mathrm{prop}}$ of an extragalactic source (i.e. M 81) measured relative to the Sun can be decomposed into a sum of three components;

$$\mathbf{v}_{\mathrm{prop}} = \mathbf{v}_{\mathrm{pec}} + \mathbf{v}_{\odot} + \mathbf{v}_{\mathrm{M81}}. \tag{4.3.1}$$

In equation 4.3.1, the first contribution $\mathbf{v}_{\mathrm{pec}}$ is the peculiar motion of M 81* relative to the center of mass of M 81 which is expected to be very small since M 81* is at the galaxy's nucleus and thus its center of mass. Note that in the Milky Way, the motion of the SMBH is less than $1\,\mathrm{km\,s^{-1}}$ ($0.03\,\mathrm{mas\,yr^{-1}}$, Reid and Brunthaler, 2004). The second contribution $\mathbf{v}_{\odot}$ is the apparent motion of M 81 caused by the motion of the Sun about the galactic center, while the last contribution $\mathbf{v}_{\mathrm{M81}}$ is the proper motion of M 81 galaxy relative to the center of the Milky Way.

4.3.2. Rotation motion of the Sun

As shown from equation 4.3.1, the only contribution that we need to correct for the M 81 proper motion, is the contribution from the motion of the sun ($\mathbf{v}_{\odot}$). The sun rotation velocity correction involves a coordinate transformation from the equatorial (centered at the Earth) to the galactic (centered at the sun) and finally to the galactocentric coordinate system (centered at the galactic center). The velocity transformation involves two main steps:

(i) A transformation from equatorial velocities (V_r, μ_α, μ_δ) to galactic velocities (U, V, W), then

(ii) A transformation from galactic velocities (U, V, W) to galactocentric velocities (V_r, μ_l, μ_b).

Equatorial to galactic transformation.

The transformation from equatorial velocities (V_r, μ_α, μ_δ) to galactocentric velocities (V_r, μ_l, μ_b), can be written in a matrix form which shows that a full transformation is the combination of three simple transformations derived from the transformation equations generally given as:

$$\cos \mathrm{b} \cos(\theta - \mathrm{l}) = \sin\delta \sin\delta_{\mathrm{NGP}} - \cos\delta \sin\delta_{\mathrm{NGP}} \cos(\alpha - \alpha_{\mathrm{NGP}}).$$

$$\cos \mathrm{b} \sin(\theta - \mathrm{l}) = \cos\delta \sin(\alpha - \alpha_{\mathrm{NGP}}). \tag{4.3.2}$$

$$\sin \mathrm{b} = \sin\delta_{\mathrm{NGP}} \sin\delta + \cos\delta_{\mathrm{NGP}} \cos\delta \cos(\alpha - \alpha_{\mathrm{NGP}}).$$

Here, α and δ are equatorial coordinates right ascension and declination respectively, l and b are galactic longitude and latitude respectively. $\alpha_{\mathrm{NGP}}=12^h51^m26^s.275$ and $\delta_{\mathrm{NGP}}=+27^\circ07'41''.704$ (J2000) are the equatorial coordinates of the North Galactic Pole (NGP), while $\theta=122^\circ.9$ (J2000) denotes the galactic longitude of the ascending node of the galactic plane (Liu et al., 2011)

The transformation equation can be simplified into a transformation matrix written as,

$$\begin{bmatrix} \cos \mathrm{b} \cos \mathrm{l} \\ \cos \mathrm{b} \sin \mathrm{l} \\ \sin \mathrm{b} \end{bmatrix} = \mathrm{T} \begin{bmatrix} \cos\delta \cos\alpha \\ \cos\delta \sin\alpha \\ \sin\delta \end{bmatrix}.$$

where $\mathbf{T}\equiv\mathbf{T}(\alpha_{\mathrm{NGP}}, \delta_{\mathrm{NGP}}, \theta)$, and thus can be evaluated for the epoch at which the (α, δ) are measured. The derived transformation matrix of $\mathbf{T}$ from Equation 4.3.2 can be written as

$$T = \begin{bmatrix} \cos\theta & sin\,\theta & 0 \\ \sin\theta & -\cos\theta & 0 \\ 0 & 0 & 1 \end{bmatrix} \begin{bmatrix} -\sin\delta_{\rm NGP} & 0 & \cos\delta_{\rm NGP} \\ 0 & -1 & 0 \\ \cos\delta_{\rm NGP} & 0 & \sin\delta_{\rm NGP} \end{bmatrix} \begin{bmatrix} \cos\alpha_{\rm NGP} & \sin\alpha_{\rm NGP} & 0 \\ -\sin\alpha_{\rm NGP} & \cos\alpha_{\rm NGP} & 0 \\ 0 & 0 & 1 \end{bmatrix},$$

which agrees with the representation given by Johnson and Soderblom (1987). Using the above definitions for $\alpha_{\rm NGP}$, $\delta_{\rm NGP}$, and θ, the right-handed galactic space-velocity transformation matrix **T** is simplified as:

$$T = \begin{bmatrix} -0.0548755604 & +0.4941094279 & -0.8676661490 \\ -0.8734370902 & -0.4448296300 & -0.1980763734 \\ -0.4838350155 & +0.7469822445 & +0.4559837762 \end{bmatrix}. \tag{4.3.3}$$

In a situation in which all the three position coordinates of a galaxy are known, i.e. the radial distance (d) and the position on the celestial sphere (α, δ), then its position can be specified in a rectangular equatorial coordinate system as:

$$\begin{bmatrix} \rm x_{eq} \\ \rm y_{eq} \\ \rm z_{eq} \end{bmatrix} = \begin{bmatrix} \rm d\cos\delta\cos\alpha \\ \rm d\cos\delta\sin\alpha \\ \rm d\sin\delta \end{bmatrix}. \tag{4.3.4}$$

We can describe the velocity of the galaxy in the galactic coordinates (U, V, W) as the first order differential of the position of the galaxy in the equatorial coordinate. Actually, the galactic coordinate system is conventionally denoted as $(\rm U, V, W) \equiv (\dot{x}, \dot{y}, \dot{z})$ such that,

$$\begin{bmatrix} \rm U \\ \rm V \\ \rm W \end{bmatrix} = \rm T\frac{d}{dt} \begin{bmatrix} \rm x_{\it eq} \\ \rm y_{\it eq} \\ \rm z_{eq} \end{bmatrix}$$

equally written as,

$$\begin{bmatrix} \rm U \\ \rm V \\ \rm W \end{bmatrix} = \rm T\frac{d}{dt} \begin{bmatrix} \rm d\cos\delta\cos\alpha \\ \rm d\cos\delta\sin\alpha \\ \rm d\sin\delta \end{bmatrix}. \tag{4.3.5}$$

After differentiation, Eqn. 4.3.5 becomes,

$$\begin{bmatrix} \mathrm{U} \\ \mathrm{V} \\ \mathrm{W} \end{bmatrix} = \mathrm{T} \begin{bmatrix} \cos\delta\cos\alpha\,\dot{\mathrm{d}} - \mathrm{d}\sin\delta\cos\alpha\,\dot{\delta} - \mathrm{d}\cos\delta\sin\alpha\,\dot{\alpha} \\ \cos\delta\sin\alpha\,\dot{\mathrm{d}} - \mathrm{d}\sin\delta\sin\alpha\,\dot{\delta} + \mathrm{d}\cos\delta\cos\alpha\,\dot{\alpha} \\ \sin\delta\,\dot{\mathrm{d}} + \mathrm{d}\cos\delta\,\dot{\delta} \end{bmatrix}. \tag{4.3.6}$$

Here we use the relations; $\dot{d}$≡V_r, $\dot{\alpha}\cos\delta$≡μ_α, and $\dot{\delta}$≡μ_δ. Equation 4.3.6 can be further simplified to

$$\begin{bmatrix} \mathrm{U} \\ \mathrm{V} \\ \mathrm{W} \end{bmatrix} = \mathrm{T} \begin{bmatrix} \cos\alpha & -\sin\alpha & 0 \\ \sin\alpha & \cos\alpha & 0 \\ 0 & 0 & 1 \end{bmatrix} \begin{bmatrix} \cos\delta & 0 & -\sin\delta \\ 0 & 1 & 0 \\ \sin\delta & 0 & \cos\delta \end{bmatrix} \begin{bmatrix} \dot{\mathrm{d}} \\ \mathrm{d}\dot{\alpha}\cos\delta \\ \mathrm{d}\dot{\delta} \end{bmatrix}. \tag{4.3.7}$$

Using a single matrix **A** defined as

$$\mathrm{A} \equiv \begin{bmatrix} \cos\alpha & -\sin\alpha & 0 \\ \sin\alpha & \cos\alpha & 0 \\ 0 & 0 & 1 \end{bmatrix} \begin{bmatrix} \cos\delta & 0 & -\sin\delta \\ 0 & 1 & 0 \\ \sin\delta & 0 & \cos\delta \end{bmatrix}, \tag{4.3.8}$$

equation 4.3.7 can be simplified as

$$\begin{bmatrix} \mathrm{U} \\ \mathrm{V} \\ \mathrm{W} \end{bmatrix} = \mathrm{T\,A} \begin{bmatrix} \mathrm{V_r} \\ \mathrm{k\,d}\,\mu_\alpha \\ \mathrm{k\,d}\,\mu_\delta \end{bmatrix}. \tag{4.3.9}$$

A proportionality constant k=4.74047 allows the values of U, V, W to be in units of $\mathrm{km\,s^{-1}}$, if the distance (**d**) is given in parsec, proper motion (μ_α,μ_δ) in $\mathrm{arcsec\,yr^{-1}}$ and radial velocity ($\mathrm{V_r}$) in $\mathrm{km\,s^{-1}}$. The U, V, W motions for M 81 are derived from V_r=−34±4 $\mathrm{km\,s^{-1}}$, d=3.63±0.34 Mpc, α=148.88822112, δ=+69.065295, μ_α=0±5.7 $\mu\mathrm{as\,yr^{-1}}$and μ_δ=−22.5±2.1 $\mu\mathrm{as\,yr^{-1}}$ as the input parameters. The obtained velocities are U=−69±3 $\mathrm{km\,s^{-1}}$, V=−110±29 $\mathrm{km\,s^{-1}}$ and W = 153±11 $\mathrm{km\,s^{-1}}$.

As mentioned earlier, the rotation of the sun about the Galactic center causes an apparent motion of the M 81 galaxy. This motion can be decomposed into a peculiar motion of the Sun and a circular motion of the local standard of rest (LSR), which follow the mean motion of material in the Milky Way's Sun neighborhood. The peculiar motion of the Sun has been determined from Hipparcos data (Dehnen and Binney, 1998) to be $\mathrm{U}_\odot$=10.00±0.36 $\mathrm{km\,s^{-1}}$(radially inwards), $\mathrm{V}_\odot$=5.25±0.62 $\mathrm{km\,s^{-1}}$ (in the direction of Galactic rotation) and $\mathrm{W}_\odot$=7.17±0.38 $\mathrm{km\,s^{-1}}$

(vertically upwards). The circular motion of the Sun has been obtained from VLBI measurements of the proper motion of Sgr A*, which is 6.379±0.026 $\mathrm{mas\,yr^{-1}}$ along the galactic plane (Reid et al., 1999, Reid and Brunthaler, 2004). If this motion is combined with a recent geometric distance estimate of the Galactic center of 8.34±0.16 kpc (Reid et al., 2014), it results to a circular rotation speed at the Sun position to be 240±8 $\mathrm{km\,s^{-1}}$ for the LSR.

Table 4.3.: M81*'s motion in Galactic coordinates

Description	U ($\mathrm{km\,s^{-1}}$)	V ($\mathrm{km\,s^{-1}}$)	W ($\mathrm{km\,s^{-1}}$)
Observed M81* motion	−59±3	−355±29	146.3±11
Effects of solar motion[a] removed	−69±3	−350.0±29	153.4±11
Effects of galactic rotation[b] removed	−69±3	−109±30	153.4±11

[a] The adopted solar motion with respect to a circular orbit is $U_\odot$=10.0±0.36 $\mathrm{km\,s^{-1}}$, $V_\odot$=5.25±0.62 $\mathrm{km\,s^{-1}}$ and $W_\odot$=7.17±0.38 $\mathrm{km\,s^{-1}}$.

[b] The adopted circular velocity of 240±8 $\mathrm{km\,s^{-1}}$ for the LSR.

Galactic to galactocentric transformation.

To obtain galactocentric motions involves going through the description used in equations 4.3.5 to 4.3.7 and write

$$\begin{bmatrix} \mathrm{U} \\ \mathrm{V} \\ \mathrm{W} \end{bmatrix} = \begin{bmatrix} \cos l & -\sin l & 0 \\ \sin l & \cos l & 0 \\ 0 & 0 & 1 \end{bmatrix} \begin{bmatrix} \cos b & 0 & -\sin b \\ 0 & 1 & 0 \\ \sin b & 0 & \cos b \end{bmatrix} \begin{bmatrix} \dot{d} \\ d\dot{l}\cos b \\ d\dot{b} \end{bmatrix} \tag{4.3.10}$$

where $\dot{l}\equiv\mu_l$, and $\dot{b}\equiv\mu_b$, we define a new matrix,

$$\mathrm{R}^T \equiv \begin{bmatrix} \cos l & -\sin l & 0 \\ \sin l & \cos l & 0 \\ 0 & 0 & 1 \end{bmatrix} \begin{bmatrix} \cos b & 0 & -\sin b \\ 0 & 1 & 0 \\ \sin b & 0 & \cos b \end{bmatrix} \tag{4.3.11}$$

where $V_l = k\,d\,\mu_l \cos b$ and $V_b = k\ d\ \mu_b$, which means that by taking a transpose of matrix R^T gives matrix R as

$$\mathrm{R}_{\mathrm{M81}} = \begin{bmatrix} -0.596364 & 0.464390 & 0.654740 \\ -0.614395 & -0.788998 & 0 \\ 0.516589 & -0.402269 & 0.755850 \end{bmatrix}, \tag{4.3.12}$$

and

$$\mathrm{R_{M82}} = \begin{bmatrix} -0.59370 & 0.47380 & 0.65034 \\ -0.62375 & -0.78160 & 0 \\ 0.50831 & -0.40565 & 0.75960 \end{bmatrix}, \tag{4.3.13}$$

such that

$$\begin{bmatrix} \mathrm{V_r} \\ \mathrm{V_l} \\ \mathrm{V}_b \end{bmatrix} = \mathrm{R} \begin{bmatrix} \mathrm{U} \\ \mathrm{V} \\ \mathrm{W} \end{bmatrix}. \tag{4.3.14}$$

A single direct transformation from the equatorial to the galactocentric coordinates can be obtained by solving the matrix multiplication of **RTA** given by:

$$\begin{bmatrix} \mathrm{V_r} \\ \mathrm{V_l} \\ \mathrm{V}_b \end{bmatrix} = \mathrm{RTA} \begin{bmatrix} \mathrm{V}_r \\ \mathrm{kd}\mu_\alpha \\ \mathrm{kd}\mu_\delta \end{bmatrix} \tag{4.3.15}$$

From the equations, the derived M81 results are $\mathrm{V_r}$=90±19 km s^{-1}, $\mathrm{V_l}$=129±25 km s^{-1} and $\mathrm{V_b}$=124±2 km s^{-1}. The motion of the Sun causes an apparent proper motion of 7.5±0.8 μas yr^{-1} in galactic longitude and 7.2±0.2 μas yr^{-1}in galactic latitude (for distance of 3.63±0.34 Mpc, galactic coordinates l =142.09°, b = 40.90° and 1 μas yr^{-1} = 17.5 km s^{-1}).

Galactocentric to equatorial transformation.

The transformation is a single rotation matrix denoted as **P** which is a simplified equation 4.3.15 such that

$$\begin{bmatrix} \mathrm{V_r} \\ \mathrm{kd}\mu_\mathrm{l}\cos\mathrm{b} \\ \mathrm{kd}\mu_\mathrm{b} \end{bmatrix} = \begin{bmatrix} 1 & 0 & 0 \\ 0 & \cos\phi & \sin\phi \\ 0 & -\sin\phi & \cos\phi \end{bmatrix} \begin{bmatrix} \mathrm{V_r} \\ \mathrm{kd}\mu_\alpha\cos\delta \\ \mathrm{kd}\mu_\delta \end{bmatrix}, \tag{4.3.16}$$

and the rotation matrix **P** is defined as

$$\mathrm{P} = \begin{bmatrix} 1 & 0 & 0 \\ 0 & \cos\phi & \sin\phi \\ 0 & -\sin\phi & \cos\phi \end{bmatrix},$$

where ϕ in equation 4.3.16 is the galactic parallactic angle given as $\phi_{\rm M81}= -234.84^\circ$ and $\phi_{\rm M82}= 125.69^\circ$. To transform directly from ($\mu_{\rm l}$, $\mu_{\rm b}$) to (μ_α,μ_δ) require the inverse of matrix denoted as $\mathbf{P^{-1}}$ given as

$$\mathrm{P}^{-1}_{\rm M81} = \begin{bmatrix} -0.57592 & -0.81753 \\ 0.81753 & -0.57592 \end{bmatrix}, \tag{4.3.17}$$

and

$$\mathrm{P}^{-1}_{\rm M82} = \begin{bmatrix} -0.5835 & -0.8121 \\ 0.8121 & -0.5835 \end{bmatrix}. \tag{4.3.18}$$

Applying the inverse matrix $\mathrm{P}^{-1}_{\rm M81}$ to the galactocentric motion of the Sun we obtain equatorial proper motion of $\dot\alpha_\odot$=$-10.2\pm0.6\,\mu$as yr^{-1} and $\dot\delta_\odot$=$2.0\pm0.5\,\mu$as yr^{-1}

4.3.3. The proper motion of M 81

The proper motion of M 81 relative to the Milky Way is obtained by correcting for the contribution of the Sun. This is derived as;

$$\begin{aligned} \dot\alpha_{M81} &= \dot\alpha_{prop} - \dot\alpha_\odot \\ &= 0(\pm5.7)+10.2(\pm0.6) \\ &= 10.2\pm5.7\,\mu\mathrm{as\,yr^{-1}} \\ &\simeq 179\pm100\,\mathrm{km\,s^{-1}} \end{aligned}$$

and

$$\begin{aligned} \dot\delta_{M81} &= \dot\delta_{prop} - \dot\delta_\odot \\ &= -22.5(\pm2.1)-2.0(\pm0.5) \\ &= -24.5\pm2.2\,\mu\mathrm{as\,yr^{-1}} \\ &\simeq -429\pm39\,\mathrm{km\,s^{-1}} \end{aligned} .$$

The reported galactocentric velocity of M 81 (73±6 km s^{-1}, de Vaucouleurs et al., 1991) is the radial motion of M 81 towards the Milky Way. Therefore, using the proper motion and the radial velocity component the three-dimensional space velocity of M 81 can be obtained. The derived total space velocity of M 81 becomes 471±108 km s^{-1} relative to MW galaxy.

5. M 82 Proper Motion

In this chapter, we discuss the nature of the observed water maser components in M 82, we also present the μas VLBI astrometry results by deriving the proper motion of the water maser spots, derive the space motion of M 82 relative to M 81 and estimate a lower limit to the mass of M 81.

5.1. Introduction

The galaxy M 82 (NGC 3034, Arp 337) is a darling of many astronomers not only due to its proximity ($\approx$3.53$\pm$0.07 Mpc; Dalcanton et al., 2009) but also for being one of the brightest infrared objects in the sky. It also hosts active starburst activity, numerous supernova remnants, maser sources and also a fascinating prominent bipolar outflow or “superwind” (Mayya and Carrasco, 2009). Besides being a fascinating object, M 82 is an edge-on inclined galaxy (i$\sim$80°) that suffers from a large amount of optical obscuration. This results to confusion in its classification. It was originally classified as Dwarf (6×10^9M$_\odot$) irregular type-II galaxy (Sandage and Brucato, 1979; Sofue, 1998), but with the discovery of a bar (Telesco et al., 1991) and arm structures in the disc (Mayya et al., 2005), it seems more likely as a late type spiral ($\sim$SBc, de Cea del Pozo et al., 2009; Mayya and Carrasco, 2009).

5.1.1. M 82 galaxy morphology

Multi-wavelength observations of M 82 reveal the complexity of the galaxy’s morphology. If we explore its structure from the inner region outwards; it has a bulge of maximum size (diameter) estimate of $\sim$ 7.5 pc (0.4 arcsec at 3.55 Mpc) and an upper mass limit of 10^7 M$_\odot$ (Gaffney et al., 1993). The nuclear starburst occupies a central region of $\sim$500 pc ($\sim$30 arcsec) in size, and harbours $\sim$$6\times10^8$ M$_\odot$ of stars which are concentrated in 200 compact clusters (Mayya and Carrasco, 2009). Surrounding the active starburst region is a molecular ring of 800 pc ($\sim$50 arcsec) in size. Using extinction free infrared bands, Telesco et al. (1991) discovered a bar of $\sim$1 kpc ($\sim$1 arcmin) length along the major axis. This bar is thought to be the main contributor to the dynamical mass of the central region. All of the above mentioned features occupy the inner disk of M 82 whose size along the major axis is estimated from optical surface brightness profile as $\sim$8 kpc ($\sim$8 arcmin). The outer disk however, extends at least up to 12 kpc ($\sim$11.2 arcmin) in size along the major axis and 4.4 kpc ($\sim$4.3 arcmin) along the minor axis. The size long the major axis is largely affected by the projection effect. The biggest feature along both sides of the minor axis is the prominent H_α and X-ray traced cone-shaped bipolar outflow structure known as a galactic superwind. The galactic superwinds trace outflows driven by winds from massive stars in the central star clusters and supernova explosions. The superwinds extends up to distances of $\sim$10 kpc ($\sim$10 arcmin) above and below the galactic plane.

The rotation curves of galaxies are often modeled to obtain the radial distribution of mass. M 82's rotation curve has been modeled using both stellar tracers (i.e. Hα and NaI; Goetz et al., 1990) and gaseous tracers (i.e. HI and CO; Sofue, 1998), yielding a maximum rotation motion of $\sim$130 km s^{-1} and $\sim$200 km s^{-1}, respectively. From figure 5.1.1, the rotation velocity of M 82 increases steeply near the center, and attains a sharp maximum at 400 pc (24 arcsec) radius. It then declines monotonically to a velocity as low as 50 km s^{-1} at 4 kpc radius which is the extent of the inner disk. The steep nuclear rise and sharp maximum of the rotation curve suggest solid body rotation, and it resembles that of a central bulge of a massive galaxy like M 81 or the Milky Way. However, no galaxy, except M 82, has been known to exhibit Keplerian-like rotation decline within a few kpc radius. This explains the reason why the mass of M 82 is concentrated within the central 1 kpc radius ($\sim 4\times10^9 M_\odot$), with the mass outside the central bar mostly associated with stars and gas in the disk.

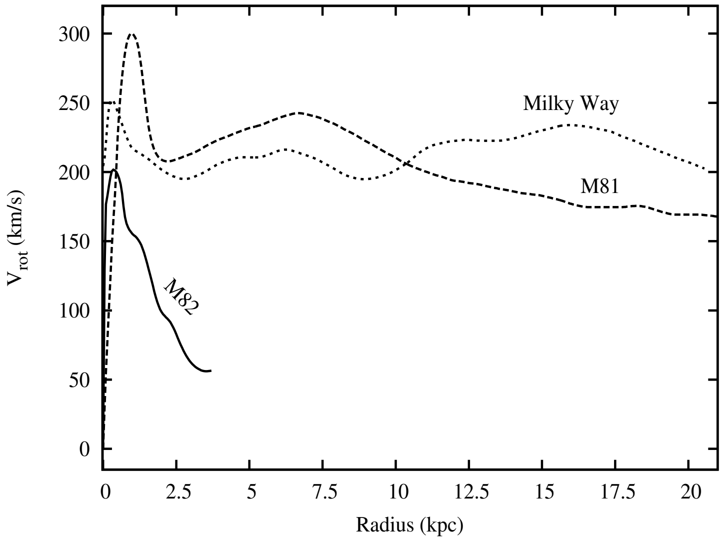

Figure 5.1.1.: Rotation curve of M 82 (full line) compared with those of M 81 (dashed line) and the Milky Way (dotted line). Keplerian-like rotation curve of M 82 is confirmed by both the stellar and gaseous rotation tracers. Courtesy of Y. Sofue.

5.1.2. Maser sources in M 82

The first extra-galactic 22 GHz H_2O maser was discovered by Churchwell et al. (1977), towards the M 33 galaxy, which opened a new phase in their studies. Their detection is done through the 22 GHz ($\lambda\sim$ 1.3 cm) $J_{k_a k_c}$ = 6_{16}–5_{23} line of ortho-H_2O that traces warm (T_{kin} > 400 K) and dense ($n(H_2) > 10^7\,cm^{-3}$) molecular gas (Henkel et al., 2005, and references therein). The extra-galactic H_2O masers, are grouped according to their isotropic luminosity (L_{iso}) (e.g., Greenhill et al., 1993): high-luminosity ($L_{iso} > 10\,L_\odot$) H_2O masers are associated with active nuclei, while low-luminosity ($L_{iso} < 10\,L_\odot$) H_2O masers are mostly associated with star-forming activity and some with low luminosity radio AGNs.

In M 82, several low luminosity H_2O maser sources with radial velocities in the range of 70 to 363 $km\,s^{-1}$ have been reported (e.g. Hagiwara, 2007, Baudry et al., 1994, Henkel et al., 1984, Baudry and Brouillet, 1996). They are located along the central ~1 kpc bar which also hosts nuclear starburst activity. The rotation of the H_2O masers is not easily determined, because the detected masers cannot be associated with other tracers of molecular clouds or continuum sources such as compact HII regions or radio SNRs (Matsushita et al., 2005). However, the kinematics of H_2O masers in M 82 was studied by Hagiwara (2007) and observed to be broadly consistent with HI and CO solid body rotation along the major axis of the galaxy. Matsushita et al. (2005) also compiled all the observed OH and H_2O masers towards M 82 and found them to be concentrated at the 100 GHz continuum emitting regions. By over-plotting the position velocity diagram of the 100 GHz molecular gas with all the detected masers, and assuming that the masers are rotating with the disk, the H_2O maser rotation velocity can be approximated as $130\pm30\,km\,s^{-1}$.

5.2. Results

The observation information is summarized in table 3.2, while a summary of the observed and successfully followed water maser components over the epochs is given in table 5.1. The number of the detected maser components varied from epoch to epoch. Between the epochs, new maser feature appeared and other disappeared. However, we were able to detect and follow the motions of three features (P1IF4C83-84, P2IF2C52-53 and P2IF2C66-67) over the four epochs. The maser names denote the pointing position (P1 and P2), the intermediate frequency (IF4 and IF2), and the channel ranges in which the maser is detected. But for simplicity, the maser features P1IF4C83-84, P2IF2C52-53 and P2IF2C66-67 will be referred to as M 82_SW, M 82_NE_1 and M 82_NE_2 features, respectively. All the maser components could be detected in two adjoining frequency channels each 1.7 $km\,s^{-1}$ wide. The feature identification was based on the positions and radial velocities of the maser emission. Throughout the observations, all the maser components were unresolved. And since the astrometric accuracy depends strongly on the source strength, we concentrate in the two channels with the strongest emission.

5.2.1. Spatial structure and variability

Figure 5.2.1 shows a 1.4 GHz continuum image of M 82, overlaid with linear contours. It also shows the three positions searched for water masers marked with red circles, while blue crosses indicate the positions for which the maser components were followed successfully over the epochs. The maser components are located on opposite sides of the M 82's center, which is marked by a magenta asterisk. The masers are at projected distances of ∼160 pc (9.4″) and ∼240 pc (13.6″) for M 82-SW and M 82-NE, respectively.

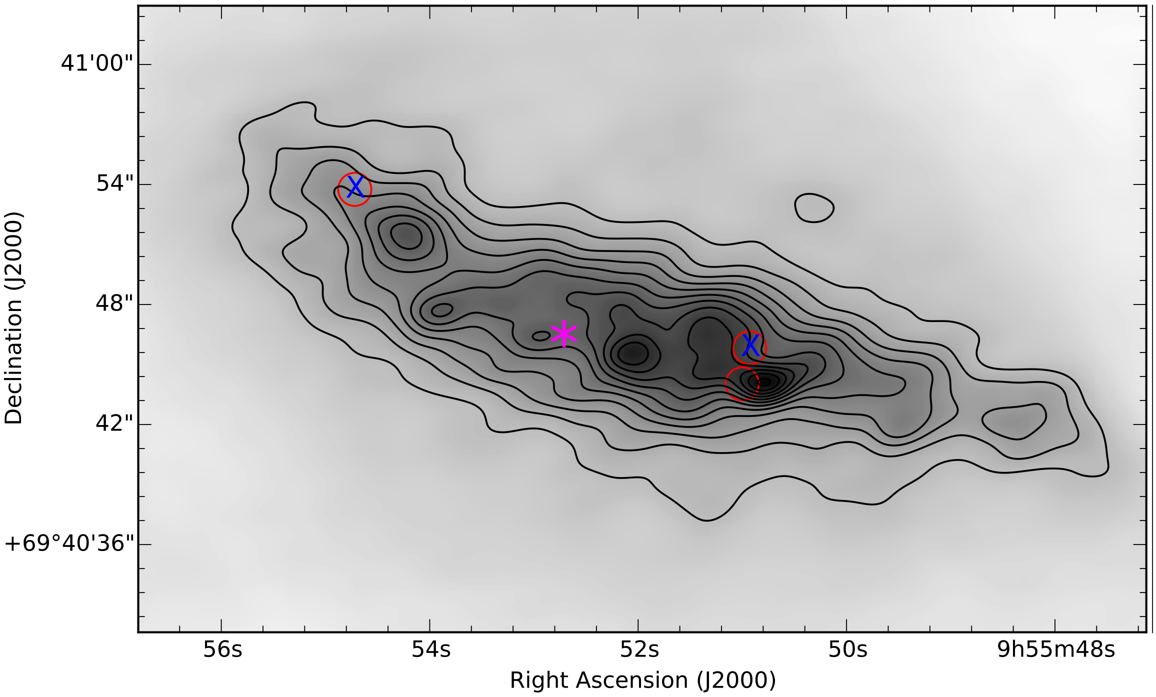

Figure 5.2.1.: The contours and the gray scale represents a 1.4 GHz image of the central region of M 82. The peak flux values are 111.86 mJy/beam while the linearly spaced contour levels start at 20 mJy/beam and have increments of 10 mJy/beam. The yellow circles indicate the three positions searched for maser emission. The position for which H_2O maser emission could be followed successfully over the four epochs of observing are marked with green cross symbols. The magenta asterisk marks the position of the radio kinematic center of M 82 at coordinates $09^h55^m52^s.725$, $+69°40'45''782$ for right ascension and declination, respectively (Jackson et al., 2007).

Table 5.1.: A summary of the H_2O maser emission in M 82 that could be followed successfully over the four epochs of observing

Epoch	Source	RA(J2000) ($09^h55^m00^s$)	Dec(J2000) ($69°40'00''$)	Total flux (mJy)	Peak Flux (mJy/b)	$\triangle\alpha$ (mas)	$\triangle\delta$ (mas)	Velocity ($\mathrm{km\,s^{-1}}$)
I (2007)	P1IF4C83-4 (M 82_SW)	50.92119525	45.5582620	68.9±4.5	55.5±2.3	9.842±0.018	14.918±0.017	120
	P2IF2C52-53 (M 82_NE_1)	54.83673734	53.8011000	55.0±6.3	35.0±2.7	15.927±0.021	−22.239±0.018	362
	P2IF2C66-67 (M 82_NE_2)	54.83656426	53.8519088	46.0±6.4	41.9±3.5	15.120±0.012	28.617±0.014	350
II (2008)	P1IF4C83-84 (M 82_SW)	50.92121005	45.5582770	18.7±3.2	12.2±1.4	9.876±0.031	14.960±0.032	120
	P2IF2C52-53 (M 82_NE_1)	54.83670997	53.8010113	235.4±3.2	214.6±1.8	15.908±0.042	−22.252±0.037	362
	P2IF2C66-67 (M 82_NE_2)	54.83654834	53.8518946	16.1±2.3	13.5±1.2	15.112±0.074	28.638±0.053	350
III (2009)	P1IF4C83-84 (M 82-SW)	50.92119987	45.5582028	23.9±1.5	20.8±0.10	9.868±0.019	14.938±0.016	120
	P2IF2C52-53 (M 82_NE_1)	54.83674830	53.8012055	34.8±1.6	21.6±0.72	15.979±0.033	−22.177±0.031	362
	P2IF2C66-67 (M 82_NE_2)	54.83657945	53.8518829	15.7±1.3	15.6±0.75	15.132±0.022	28.630±0.023	350
IV (2015_1)	P1IF4C83-84 (M 82-SW)	50.92118725	45.5586612	15.2±2.7	7.4±1.0	9.897±0.025	15.027±0.027	120
	P2IF2C52-53 (M 82_NE_1)	54.83671818	53.8011638	112.7±7.5	48.2±1.5	15.971±0.021	−22.162±0.021	362
	P2IF2C66-67 (M 82_NE_2)	54.83663842	53.8520456	7.2±0.9	3.2±0.2	15.190±0.019	28.717±0.024	350
IV (2015_2)	P1IF4C83-84 (M 82-SW)	50.92122101	45.5583157	15.0±3.1	8.5±0.8	9.890±0.032	15.049±0.031	120
	P2IF2C52-3 (M 82_NE_1)	54.83672101	53.8011182	106.0±2.7	49.7±1.3	15.955±0.029	−22.120±0.035	362
	P2IF2C66-67 (M 82_NE_2)	54.83663561	53.8521365	7.5±1.6	3.8±0.6	15.201±0.060	28.697±0.057	350

Fig.5.2.2 shows the phase-referenced contour images of maser M 82-SW, image centered at the position followed over the years. The maser M 82-SW ($V_{\rm LSR}$ $\approx$120 km s^{-1}) is located at $(\alpha, \delta)_{\rm J2000}$=09$^{\rm h}55^{\rm m}50^{\rm s}$.92120±0.00002, +69°40′45″.55822±0.00015 considered as position 1. The position errors given above are the formal values determined using AIPS task JMFIT on a map of integrated emission. From the figure, the image on the left shows the maser spot detected in 2007 January 28. It is a single water maser component with a peak flux value of 55.5 mJy/beam. It's contour level starts at 3×rms of noise (2.7 mJy) and increases with $\sqrt{2}$. The restoring beam determined by IMAGR is 0.71×0.52 mas at a position angle of 37°. The image marked May. 2008 shows the maser spot obtained in 2008 May 3. We detected two components separated by about one beam size and blended together. These two features were fit using two elliptical Gaussian components simultaneously to derive the flux and position values. From the fit results, the maser detected in 2007 had its peak flux decreased to 12.2 mJy/beam, while a new brighter maser that appeared on the eastern side had a peak flux of 82.3 mJy/beam. The contour level starts at 3×rms of noise (1.5 mJy), increasing with $\sqrt{2}$. The restoring beam size is 1.17×1.01 mas at a position angle of 24°. The image marked Apr. 2009 shows the same maser spot in 2009 April 8 with a peak flux density of 23.9 mJy/beam, while the peak flux of the maser that appeared in 2008 dropped to 12.4 mJy/beam as also shown in figure 5.2.3. The contour values are spaced in $\sqrt{2}$ intervals starting at 3×rms of noise (0.8 mJy). The beam size during imaging was 0.76×0.54 mas at a position angle of -3°. In the last image marked Dec. 2015, the maser component of interest is still visible with a peak flux of 8.5 mJy/beam, while several weak features are detected on its eastern side. Its contour level starts at 3×rms of noise (0.3 mJy), increasing with $\sqrt{2}$. The beam size is 0.60×0.42 mas at a position angle of 19°.

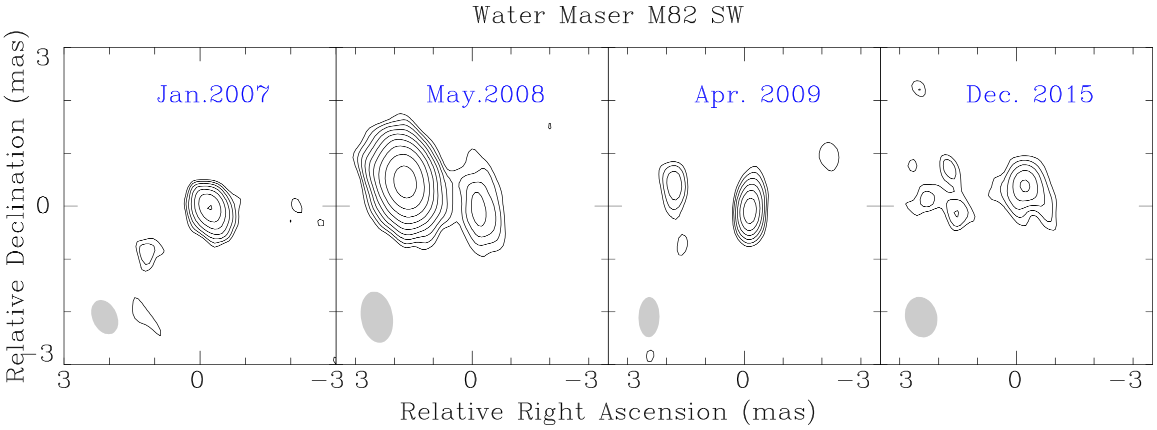

Figure 5.2.2.: The contour maps of evolution of the water maser M82_SW at $V_{LSR} \approx 120\,km\,s^{-1}$ over the eight years of observation. A new maser spot is observed in 2008 May and had weakened by 2009 April observation, thus showing a case of water maser variability of less than two years.

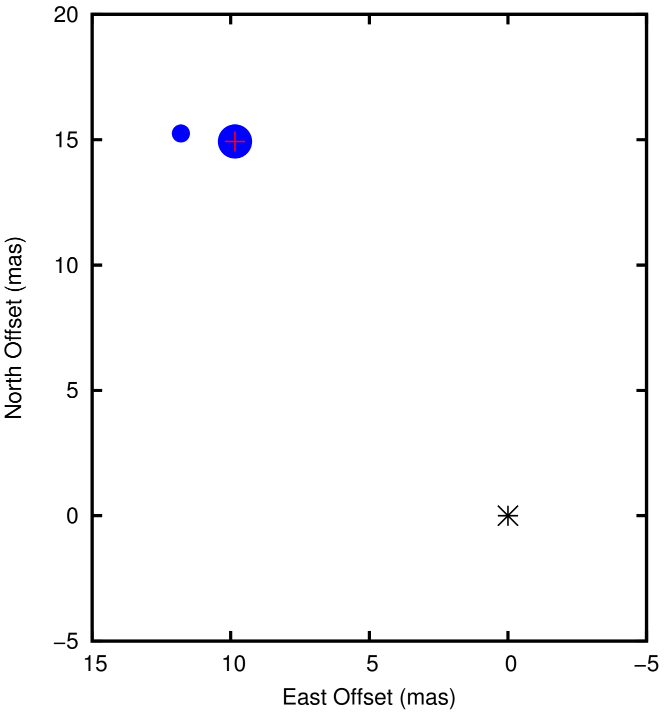

Figure 5.2.3.: Composite map of the H_2O masers in M82 from the April 2009 observation at the pointing position 1. The area of each circle is proportional to the flux density of the respective component. Both of this masers components are at LSR velocity of $120\,km\,s^{-1}$. The black asterisk marks the phase center position of this observation and red cross the location of maser spot M82-SW that could be successfully followed over the four epochs.

Fig. 5.2.4 shows the contour image of maser M 82_NE_1 centered at the position followed over the years. The maser M 82_NE_1 (V_{LSR} ≈362 km s^{-1}) is located at $(\alpha,\delta)_{J2000}$= 09^{h}55^{m}54^{s}.83671± 0.00001, +69°40′53″.80101 ± 0.00002 considered as position 2. The position errors given above are the formal values determined using AIPS task JMFIT on a map of integrated emission. From the figure, the image on the left shows the maser spot observed in 2007 January with a peak flux value of 35.0 mJy/beam. It's contour level starts at 3×rms of noise (2.7 mJy) and increases with $\sqrt{2}$. The restoring beam determined by IMAGR is 0.75×0.49 mas at a position angle of 35°. The second image marked May. 2008 shows the maser spot detected in 2008 May 3, the maser detected in 2007 has its peak flux increased to 214.6 mJy/beam. The contour values increases with $\sqrt{2}$ starting at 3×rms of noise (1.8 mJy). The beam size is 0.45×0.35 mas at a position angle of 2°. The third image marked Apr. 2009 shows the maser spot detected in 2009 April 8. The spot detected in 2007 is still visible with a peak flux density of 21.6 mJy/beam. The contour level start at 3×rms of noise (0.7 mJy), increasing with $\sqrt{2}$. The restoring beam is 0.67×0.48 mas at a position angle of 18°. The last image to the right marked as Dec. 2015 shows the same maser component with a peak flux density of 48.2 mJy/beam. Its contour level start at 3×rms of noise (1.5 mJy), increasing with $\sqrt{2}$. The beam size is 0.74×0.31 mas at a position angle of 156°. The figure 5.2.6 shows this maser spot as the brightest (largest) spot, located at the lower left end of the figure, relative to the pointing position on the third epoch.

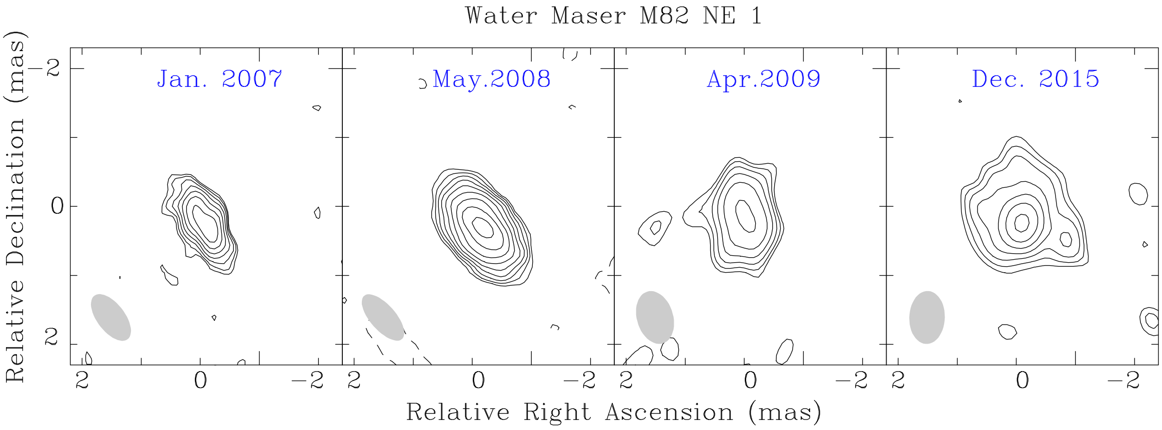

Figure 5.2.4.: The contour maps of water maser M 82_NE_1 at V_{LSR} ≈362 km s^{-1} over the four epochs. The maser peak position used to obtain the proper motion is marked with a red dot.

Fig. 5.2.5 shows the contour image of maser M 82_NE_2 centered at the position followed over the years. The maser M 82_NE_2 (V_{LSR} ≈350 km s^{-1}) is located at $(\alpha, \delta)_{J2000}$= $09^h55^m54^s.83655 \pm 0.00001$, $+69^\circ 40' 53''.85188 \pm 0.00002$ considered as position 2. The position errors given above are the formal values determined using AIPS task JMFIT on a map of integrated emission. From the figure, the image on the left shows the maser spot on 28 Jan 2007 with a peak flux value of 41.9 mJy/beam. It's contour level starts at 3×rms of noise (2.6 mJy) and increases with $\sqrt{2}$. The restoring beam determined by IMAGR is 0.85×0.64 mas at a position angle of 40°. The second image shows the maser spot observed in 2008 May 3, in which the maser detected in 2007 has its peak flux decreased to 13.5 mJy/beam. The contour values increases with $\sqrt{2}$ starting at 3×rms of noise (1.4 mJy). The beam size during imaging is 0.85×0.75 mas at a position angle of 15°. The third image shows the maser spot detected in 2009 April 8. The spot detected in 2007 is still visible with a peak flux density of 15.6 mJy/beam. Its contour level starts at 3×rms of noise (0.8 mJy), increasing with $\sqrt{2}$. The beam size is 0.77×0.54 mas at a position angle of −4°. The last image to the right shows the maser component observed in 2015 December 21 whose peak flux density is 3.2 mJy/beam, contour level starts at 3×rms of noise (0.2 mJy), increasing with $\sqrt{2}$. The restoring beam size is 0.74×0.31 mas at a position angle of 159°. The figure 5.2.6 shows the upper left as location of the maser relative to the pointing position on the third epoch.

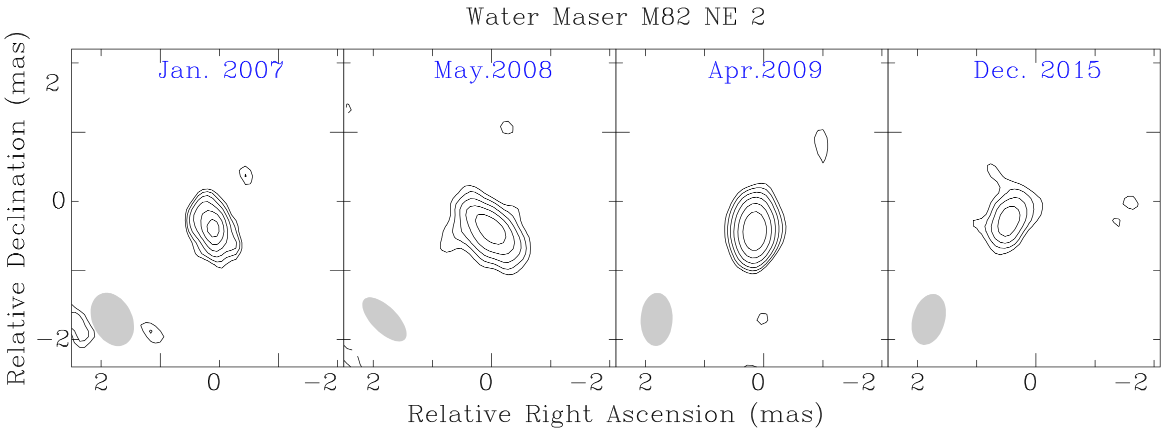

Figure 5.2.5.: The contour maps of water maser M 82_NE_2 at V_{LSR} ≈362 km s^{-1} over the four epochs. The maser peak position used to obtain the proper motion is marked with a red dot.

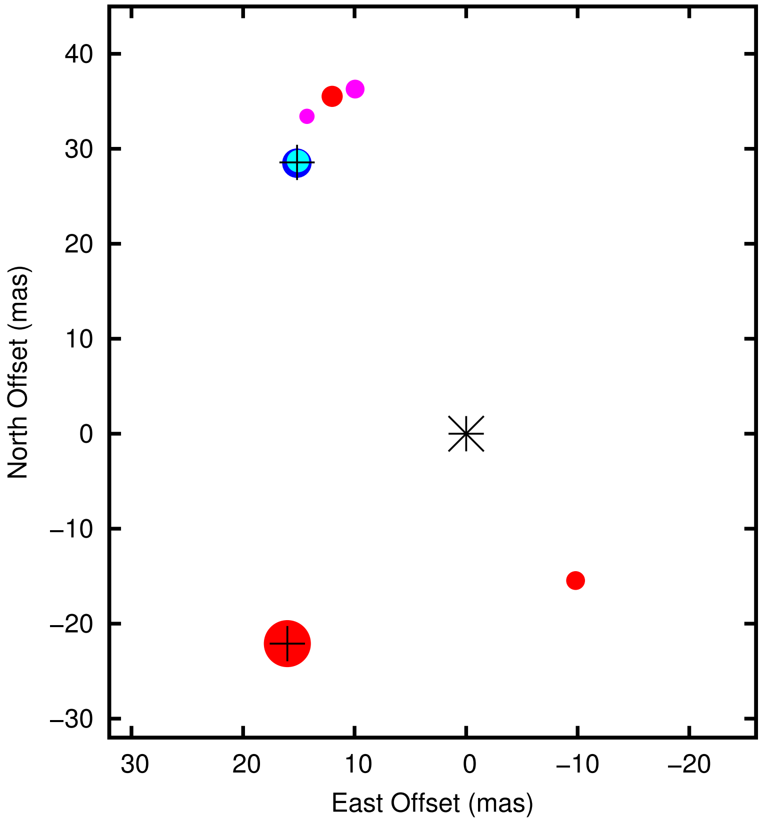

Figure 5.2.6.: Composite map of the H_2O masers in M 82 from the 2009 April 08 observations. The area of each circle is proportional to the flux density of the respective component. The colors denote different LSR velocities with 345 to 349 km s^{-1} (cyan), 350 to 354 km s^{-1} (blue), 355 to 359 km s^{-1} (magenta), and 360 to 365 km s^{-1} (red). The black asterisk marks the phase center position of this observation and black cross the location of the maser spots M 82_NE_1 (lower left) and M 82_NE_2 (upper left) that could be successfully followed over the four epochs.

5.2.2. Observed motions

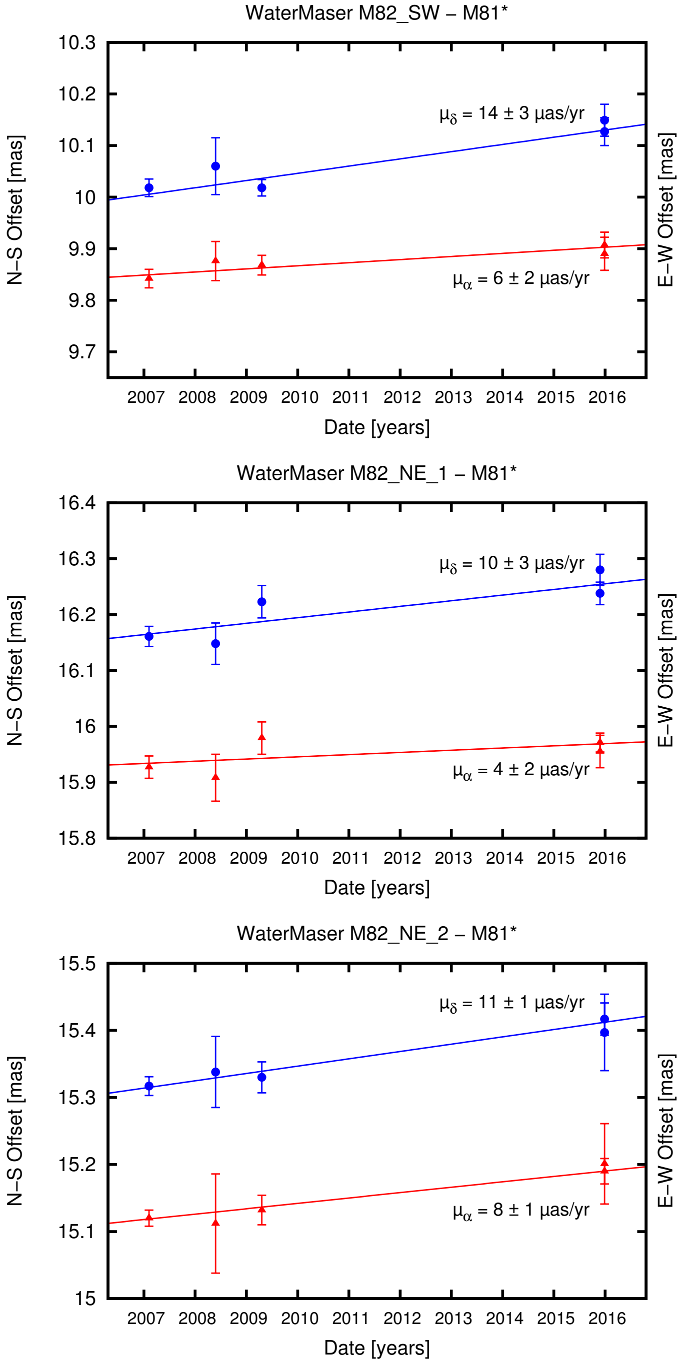

Figure 5.2.7.: The 22.2 GHz water maser proper motions. **Top** :The motion of maser feature M 82_SW, **middle** :The motion of maser feature M 82_NE_1 and **bottom** :The motion of maser feature M 82-NE_2, all relative to M 81*. For the three features, the East-West positions are marked with red triangles and North-South with blue circles. The lines show a rectilinear fit to the data points.

The positions of the maser feature M 82-SW shown in the Fig.5.2.7 (top) are fitted with a linear fit, that yields a proper motion of $6\pm2\,\mu$as yr^{-1} and $14\pm3\,\mu$as yr^{-1} towards east and north, respectively. The Fig.5.2.7 (middle) shows the fitted position of the maser feature M 82_NE_1, whose proper motion towards east and north is $4\pm2\,\mu$as yr^{-1} and $10\pm3\,\mu$as yr^{-1}, respectively. The position offsets of the maser feature M 82_NE_2 are shown in the Fig.5.2.7 (bottom), a fit to the data yields a value of $8\pm1\,\mu$as yr^{-1} towards the East and $11\pm1\,\mu$as yr^{-1} towards the North. In all of these cases, the motion of the masers relative to M 81* are consistent within the errors which allows for an estimate of the proper motion of M 82 galaxy. With the proper motion results almost in agreement for the three maser positions in right ascension and declination, the accuracy derived from the standard deviation is too small, and considered less representative.

5.3. Discussion

5.3.1. Space motion of M 82

The derived proper motion $\mathbf{v}_{\mathrm{prop}}$ of water maser in M 82 can be decomposed into a sum of three components, relative to a frame at rest at the center of the M 81 galaxy.

$$\mathbf{v}_{\mathrm{prop}} = \mathbf{v}_{\mathrm{pec}} + \mathbf{v}_{\mathrm{rot}} + \mathbf{v}_{\mathrm{M82}} \tag{5.3.1}$$

In equation 5.3.1, the first contribution, $\mathbf{v}_{\mathrm{pec}}$ is the peculiar motion of the masers relative to the circular galactic rotation. We assume $\mathbf{v}_{\mathrm{pec}}$ to be negligible for edge-on M 82 considering its fast rotation motion. The second contribution, $\mathbf{v}_{\mathrm{rot}}$ is the motion of the maser due to the internal galactic rotation in M 82. The last contribution $\mathbf{v}_{\mathrm{M82}}$ is the true proper motion of the M 82 galaxy relative to M 81*.

5.3.2. Rotation motion of M 82

The main contributor to the proper motion of M 82 relative to M 81 is the rotation motion ($\mathbf{v}_{rot}$) of M 82 galaxy. To derive the rotation of water masers in M 82, we will follow closely the procedure employed by Brunthaler (2004) in his thesis to derive the rotation velocity of masers in IC 10.

Let us consider a disk (see Figure 5.3.1, left), whose rotation can be described by the rotation vector ω. This vector is parallel to the galactic rotation axis and its length is equal to the rotation speed. An observer will see a projection of the disk on the sky (see Figure 5.3.1, right) and the orientation of this ellipse is given by two observables. (i) The inclination of the disk - the angle between the galactic rotation axis and the line of sight, i.e. 90°for an edge-on and 0° for a face-on galaxy. (ii) The position angle of the major axis - the angle between a line from the galaxy's center headed north and the east major axis, where east is on the left in astronomical maps.

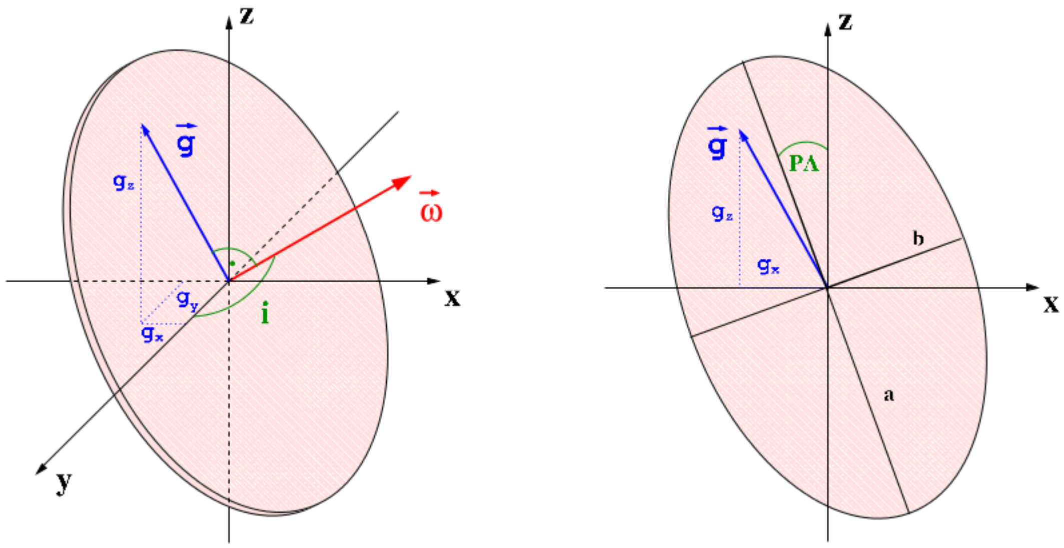

(a) A 3-dimensional orientation of a disk of a galaxy. The x and z axes are on the plane of the sky, and the y axis towards the observer. ω is the rotation vector and **g** points towards a point in the galaxy.

(b) A galaxy disk projection on the sky as seen by the observer. The observables are the major and minor axis of the ellipse (**a** and **b**) anf the position angle (PA) of the major axis. The inclination is then given by $\cos i = b/a$

Figure 5.3.1.: A galaxy disk orientation on the sky as seen by the observer. Image courtesy of A. Brunthaler - MPIfR

One can define a three dimensional Cartesian coordinate system (x,y,z) with the origin at the center of the disk. The x- and z-axes are in the direction of negative right ascension and positive declination, respectively. The y-axis points towards the observer. In this coordinate system, the rotation vector ω is related to the inclination i and the position angle PA by:

$$\omega = \omega_0 \begin{pmatrix} \cos \mathrm{PA} \sin \mathrm{i} \\ -\cos \mathrm{i} \\ \sin \mathrm{PA} \sin \mathrm{i} \end{pmatrix}, \tag{5.3.2}$$

where ω_0 is the rotation speed. One can now construct a vector **g** which lies in the plane of the disk and points from the origin towards the maser. The x- and z-components of **g** are given by the offset of the masers from the center of the disk on the sky.

The y-component of **g** is constrained by the fact that ω and **g** are orthogonal such that:

$$\omega . \mathrm{g} = \omega_{\mathrm{x}} \mathrm{g}_{\mathrm{x}} + \omega_{\mathrm{y}} \mathrm{g}_{\mathrm{y}} + \omega_{\mathrm{z}} \mathrm{g}_{\mathrm{z}} = 0 \tag{5.3.3}$$

This leads to

$$\mathrm{g}_{\mathrm{y}} = -\frac{(\omega_{\mathrm{x}} \mathrm{g}_{\mathrm{x}} + \omega_{\mathrm{z}} \mathrm{g}_{\mathrm{z}})}{\omega_{\mathrm{y}}} \tag{5.3.4}$$

hence, the absolute value of g is given by

$$|\mathrm{g}| = \sqrt{\mathrm{g}_{\mathrm{x}}^2 + \mathrm{g}_{\mathrm{y}}^2 + \mathrm{g}_{\mathrm{z}}^2}$$

The rotation velocity υ at the position **g** is now orthogonal to **g**, since it moves on a circular orbit. It is also orthogonal to ω, since it is on the plane of the galaxy. Therefore, υ is given by:

$$\upsilon = \frac{1}{|\mathrm{g}|} \omega \times \mathrm{g}. \tag{5.3.5}$$

M82 is almost an edge-on galaxy with a large inclination of the disk of the galaxy to the sky-plane of ~80° (Lynds and Sandage, 1963), a position angle of ~65° (de Vaucouleurs et al., 1991) and maser rotation speed, ω_0, is $130 \pm 30\,\mathrm{km\,s^{-1}}$.

The angular separation of maser M82_SW is 9.4 arcsec (~161 pc) west and 0.4 arcsec (~7 pc) south, while for maser M82_NE_1 and M82_NE_2 is 11 arcsec (~191 pc) east and 8 arcsec (~138 pc) north of the kinematic center. This corresponds to a rotation motion of $107 \pm 25\,\mathrm{km\,s^{-1}}$ in right ascension and $-59 \pm 14\,\mathrm{km\,s^{-1}}$ in declination for maser spot at the southwestern location. The rotation motion for masers at the northeastern location is $-113 \pm 26\,\mathrm{km\,s^{-1}}$ and $58 \pm 14\,\mathrm{km\,s^{-1}}$ in right ascension and declination, respectively. This translates to a relative rotation motion of $\dot{\alpha}_{rot}$=6.4±1.5 μas yr^{-1} and $\dot{\delta}_{rot}$= −3.5±0.8 μas yr^{-1} for the southwestern maser spot and $\dot{\alpha}_{rot}$=−6.7±1.5 μas yr^{-1} and $\dot{\delta}_{rot}$=3.4±0.8 μas yr^{-1} for the northeastern maser spot.

5.3.3. The proper motion of M 82

Correcting for the M 82 rotation motion contribution for the masers at the northeastern and southwestern location i.e.

- The southwestern location maser (M82_SW)

$$\begin{aligned} \dot{\alpha}_{\mathrm{M82-SW}} &= \dot{\alpha}_{\mathrm{prop}} - \dot{\alpha}_{\mathrm{rot}} & \dot{\delta}_{\mathrm{M82-SW}} &= \dot{\delta}_{\mathrm{prop}} - \dot{\delta}_{\mathrm{rot}} \\ &= 6(\pm 2) - 6.4(\pm 1.5) \ \text{ and } & &= 14(\pm 3) + 3.5(\pm 0.8) \\ &= -0.4 \pm 2.5\,\mu\mathrm{as\,yr}^{-1} & &= 17.5 \pm 3.0\,\mu\mathrm{as\,yr}^{-1} \end{aligned}$$

- The first northeastern location maser (M82_NE_1)

$$\begin{aligned} \dot{\alpha}_{\mathrm{M82-NE-1}} &= \dot{\alpha}_{\mathrm{prop}} - \dot{\alpha}_{\mathrm{rot}} & \dot{\delta}_{\mathrm{M82-NE-1}} &= \dot{\delta}_{\mathrm{prop}} - \dot{\delta}_{\mathrm{rot}} \\ &= 4(\pm 2) + 6.7(\pm 1.5) \ \text{ and } & &= 10(\pm 3) - 3.4(\pm 0.8) \\ &= 10.7 \pm 2.5\,\mu\mathrm{as\,yr}^{-1} & &= 6.6 \pm 3.0\,\mu\mathrm{as\,yr}^{-1} \end{aligned}$$

- The second northeastern location maser (M82_NE_2)

$$\begin{aligned} \dot{\alpha}_{\mathrm{M82-NE-2}} &= \dot{\alpha}_{\mathrm{prop}} - \dot{\alpha}_{\mathrm{rot}} & \dot{\delta}_{\mathrm{M82-NE-2}} &= \dot{\delta}_{\mathrm{prop}} - \dot{\delta}_{\mathrm{rot}} \\ &= 8(\pm 1) + 6.7(\pm 1.5) \ \text{ and } & &= 11(\pm 1) - 3.4(\pm 0.8) \\ &= 14.7 \pm 2\,\mu\mathrm{as\,yr}^{-1} & &= 7.6 \pm 1.3\,\mu\mathrm{as\,yr}^{-1} \end{aligned}$$

The proper motion of M 82 relative to M 81 is then given by by the averaged rotation motion correct proper motion of the three quasars. Hence, the average proper motion of the three maser features with its accuracy derived from the standard deviation of the fit results is $\dot{\alpha}_{\mathrm{M82}}$ =8.3±5.5 μas yr^{-1} (143 ± 95 km s^{-1}) and $\dot{\delta}_{\mathrm{M82}}$ =10.6±4.3 μas yr^{-1} (182 ± 74 km s^{-1}).

The reported systematic heliocentric velocity radial motions of M 81 and M 82 towards the Sun are −34±4 km s^{-1} and 203±4 km s^{-1}, respectively (de Vaucouleurs et al., 1991). The component of the M 82 radial motion about the M 81 center becomes 237±6 km s^{-1}. Therefore, the proper motion and the radial velocity component about M 81 give the three-dimensional space velocity of M 82. The derived total space velocity of M 82 becomes 331±120 km s^{-1} relative to M 81 galaxy.

5.3.4. Lower mass estimate of M 81

There have been attempts to estimate the mass of the M 81 group. For instance, Karachentsev and Kashibadze (2006) determined the mass from external Hubble field of velocities from the relation

$$M_T = \left(\frac{\pi^2}{8G}\right) \times R_0^3 \times T_0^{-2} = 1.46 \times 10^{12} \times R_0^3, \tag{5.3.6}$$

where G is the gravity constant and T_0 is the age of the universe (13.7±0.2 Gyr, Spergel et al., 2003). The radius of the zero-velocity surface relative to M 81, R_0, was estimated as 0.89±0.05 Mpc, and used to estimate the group mass M_T to be $(1.03\pm0.17)\times10^{12}\,M_\odot$. With this R_0, also the masses of M 81 and M 82 could be estimated by determining the mass ratios from varying the position of the center of mass between the two galaxies, resulting in $6.7\times10^{11}\,M_\odot$ and $3.6\times10^{11}\,M_\odot$, respectively. However, this method assumes 1) a spherically symmetric shape of the group potential well, 2) small random motions of the galaxies relative to the regular Hubble flow, and 3) a sufficiently high number density of galaxies for which radial velocities and distances are known with high accuracy.

From the assumptions, it is evident that the most reliable way of deriving masses is using orbits, which requires the knowledge of three-dimensional velocity vectors. Having estimated the proper motions and derived the space motions of M 81 and M 82, we can estimate the lower mass estimate of M 81. The separation distance of the centers is 38 kpc (∼37 arcmin), hence M 82 is deeply embedded in M 81's dark matter halo, which extends to ∼140 kpc. If we consider M 82 as bound to M 81's gravitational potential, its velocity must be smaller than the escape velocity and one can therefore deduce a lower limit on the mass of M 81. In the bound case, the kinetic energy is equal in magnitude to the potential energy and can be equated as

$$\frac{1}{2}\mathrm{mv}^2 = \mathrm{G}\frac{\mathrm{mM}}{\mathrm{R}}, \tag{5.3.7}$$

where v is the rotation speed in $\mathrm{km\,s^{-1}}$, R is the radius of the orbit in parsecs, m is the mass of the moving particle (M 82), M is the central mass (M 81) in Solar Masses, and G is the universal gravitational constant, $4.302\times10^{-3}\,\mathrm{pc\,M_\odot^{-1}\,(km/s)^2}$. Rearranging the equation, it becomes $\mathrm{M_{M81}} > \frac{\mathrm{v^2R}}{\mathrm{2G}}$. Using R=38 kpc and $\mathrm{v}=331\pm120\,\mathrm{km\,s^{-1}}$, we get a lower mass estimate of

$$\mathrm{M_{M81}} > (4.84 \pm 0.64) \times 10^{11}\,\mathrm{M_\odot}.$$

6. Radio supernova SN 2008iz

In the course of monitoring the water maser sources to derive the proper motion of M 82 presented in chapter 5, a bright new radio source appeared in one of the monitoring sessions. The source turned out to be a supernova. The supernova was discovered by sheer luck, more than one year after its explosion. Coincidentally, (i) the supernova exploded in a region of active star-formation which also host water maser sources that were being monitored. (ii) the supernova position is within the field of view of the VLBI telescope which is incredibly small ($\sim$few milliarcsec at 22 GHz). From these coincidences, it was possible to locate the supernova in our earlier VLBI observations. After its confirmation, a multi-frequency follow up programme with the VLA and VLBI telescopes was initiated to trace its radio evolution. In this chapter, we present the general information on the VLBA and VLA data, the structural evolution of the supernova from both the light-curve and the VLBI images, supernova size estimates from which we derive the shock wave deceleration parameter (m), spectral index evolution and the magnetic field estimates.

Note: This chapter is reproduced from a paper titled "Radio evolution of supernova SN 2008iz in M 82". The manuscript is already submitted and accepted for publication by the Astronomy and Astrophysics (A&A) Journal. Being the first author, I have adapted the manuscript as part of this thesis. The reference of the paper is Kimani et al.,2016, and the archive link is http://arxiv.org/pdf/1606.08742.pdf

6.1. Introduction

Radio-loud supernovae are rare events of which just a few dozen have been detected so far (Weiler et al., 2002). Most of them are relatively distant or fairly weak, making them difficult to study in great detail. To date, the best-known example is SN 1993J in M 81 (Martí-Vidal et al., 2011a,b and references therein), which has been studied extensively because to its proximity (3.63 Mpc, Freedman et al., 1994), environment (which allows for multi-wavelength studies) and galaxy orientation (M 81 is seen almost face-on). The discovery of SN 2008iz (Brunthaler et al., 2009a) offers the possibility of studying another supernova at a very similar distance in great detail and to make a comparison to SN 1993J. For instance, considering the peak 5 GHz radio luminosities, SN 2008iz at $L_{5GHz} \propto 24.4 \times 10^{26}$ ergs^{-1}Hz^{-1} is comparable to SN 1993J at $L_{5GHz} \propto 15.5 \times 10^{26}$ ergs^{-1}Hz^{-1} (van Dyk et al., 1994). The two supernovae are also comparable in the time they took to reach their peak after the explosion, with SN 2008iz taking ∼125 days while SN 1993J took 133 days (Weiler et al., 2007).

Supernova 2008iz was discovered in M 82, which is a nearby star-burst galaxy forming part of M 81 group. This galaxy harbours numerous bright radio supernova remnants with the current estimate at 50 supernovae (Muxlow et al., 1994; Beswick et al., 2006; Fenech et al., 2008; Kronberg et al., 2000; Weiler et al., 2002).

Supernova 2008iz was discovered in 2009 April as a bright radio transient (Brunthaler et al., 2009a,b). The explosion date of the supernova is estimated to be 2008 February 18±6 days (Brunthaler et al., 2009b; Marchili et al., 2010). The discovery was made at radio wavelengths with the VLA at 22 GHz (Brunthaler et al., 2009a) and confirmed with MERLIN (Muxlow et al., 2009; Beswick et al., 2009) and the Urumqi 25 meter telescope at 5 GHz (Marchili et al., 2010). Endeavours to make detections in other astronomical windows have never been successful. For instance, there are no detections in visible light and the X-Ray regimes (Brunthaler et al., 2009b). Varenius et al. (2015) also report the LOFAR (Low-Frequency Array for Radio Astronomy) non-detection at 154 MHz. However, a detection of the near-IR counterpart for SN 2008iz at ∼480 days was reported by Mattila et al. (2013) after careful analyses using image subtraction techniques and considering possible uncertainties caused by the differing filter response functions between the Gemini-North telescope and the HST. Overall, this makes it challenging to classify this supernova. Nevertheless, since no type Ia supernova has yet been detected in the radio regime in M 82 (Pérez-Torres et al., 2014), we can firmly say that SN 2008iz is a core collapse supernova, in agreement with both (Brunthaler et al., 2009b) and Mattila et al. (2013).

The position of supernova SN 2008iz is estimated to be $\alpha_{J2000} = 09^{h}55^{m}51^{s}.551 \pm 0^{s}.008$, $\delta_{J2000} = +69^{\circ}40'45''.792 \pm 0''.005$ (Brunthaler et al., 2009b) which is $2.5''$ (43 pc) south-west of the photometric center of M 82 based on the 2.2μm infrared emission peak (Weiß et al., 2001). The location of the supernova is heavily obscured by dust and gas, hiding the region from direct observations at optical wavelengths (Weiß et al., 2001). Brunthaler et al. (2010) made an estimate of the dust extinction towards SN 2008iz to be A_{υ} ∼24.4 mag, concluding that the supernova non-detections was because it exploded behind a large dusty interstellar cloud. However, using the same data and relations Mattila et al. (2013) obtained a total extinction of ∼48.9 mag suggesting that the authors may have missed to multiply the value of N(H_2) by 2 to convert to hydrogen nuclei before applying the extinction relation of Güver and Özel (2009). The near-IR detection could indicate that the supernova was located in the foreground with most of the H_2 column density behind the site of SN 2008iz (Mattila et al., 2013).

VLBI observations reveal the expansion of SN 2008iz to be self-similar with an expansion velocity of ~21 000 km s^{-1} over the first 430 days after the explosion, making it one of the fastest expanding radio supernovae, with an expansion index, m, of 0.89±0.03 (Brunthaler et al., 2010). The modeled light curve by (Marchili et al., 2010) shows that synchrotron self-absorption (SSA) is negligible, making free-free absorption (FFA) the most significant process during the supernova expansion.

Radio monitoring of SN 2008iz with VLA and VLBI has been ongoing on a regular basis since its discovery. We describe the monitoring and data reduction process in section 2. In section 3 we present multi-frequency radio observations from 36 to 2167 days after the explosion. In section 4 we discuss the variations of the spectral index α, equipartition minimum energy and magnetic fields, the evolution of the magnetic field evolution B_{eq} and its amplification. We present our summary in section 5.

6.2. Observations and Data Calibration

The radio monitoring campaign conducted with the VLA, at 1.4, 4.8, 8.4, 22 and 43 GHz to trace the evolution of the radio emission from SN 2008iz has been ongoing since its discovery in 2008. The first series of observations is archival and corresponds to the data published by (Brunthaler et al., 2009b, 2010). It consists of six observations (epochs 1 - 6 in table 6.1) obtained between 2008 March 24 (day 36) and 2009 September 19 (day 580). For details on the observations of those epochs, the reader is referred to their publications. For the later observations, the data was taken in the standard continuum observation mode with a total bandwidth of 128 MHz, each in dual circular polarisation. During these epochs, observations were done in VLA configurations A, AB, B and C. Flux density measurements were derived using calibrator 3C48. The flux calibrator was observed for a total time of 2 minutes in each observation. The observation used a switching cycle of six minutes, spending on average 1 minute on the phase calibrator J1048+7143 and 5 minutes on M 82. The cycles were repeated 5 times over the observations, yielding an integration time of ~25 minutes on M 82 at each frequency.

The last epoch of VLA observations on 2014 January 23 was obtained during a confirmation search of a newly discovered Type Ia supernova, SN 2014j at C and K-bands under the observation code TOBS0008 at configuration AB. The data was taken in the standard continuum observation mode with a total bandwidth of 128 MHz, each in dual circular polarisation. The flux calibrator 3C48 was observed for a total time of 3 minutes. The observation used a switching cycle of 9 minutes, spending an average time of 30 seconds on the phase calibrator J1048+7143 and 8 minutes on M 82. The cycle was repeated 4 times over the observation, yielding an integration time of ~32 minutes on M 82 at both frequencies.

The VLA observations in this work are matched by high resolution VLBI observations at 1.6, 4.8 and 8.4 GHz. These were taken with a network consisting of the Very Long Baseline Array (VLBA), the Green Bank 100 meter telescope and the Effelsberg 100 meter telescope leading to a maximum resolution of 4.3 milliarcseconds (mas) at 1.6 GHz, 1.2 mas at 4.8 GHz and 0.8 mas at 8.4 GHz. SN 2008iz was observed 15 times between 2009 October and 2013 January in dual polarisation. The total bandwidth of most datasets is 64 MHz, although two datasets have a bandwidth of 32 MHz and three have a bandwidth 260 MHz wide. The fluxes were calibrated using system temperature measurements and standard gain curves, and the AGN in M 81 (M81*) was used as a phase reference calibrator. The calibrator J1048+7143 was observed several times during each observation run, each time for 90 to 120 seconds. SN 2008iz and M 81* were observed in turns for 45 to 55 seconds at 1.6 GHz and ~80 seconds at 4.8, and 8.4 GHz during each observation run.

The VLA and VLBI data were reduced using standard packages within the AIPS (Astronomical Image Processing Software) of the National Radio Astronomy Observatory (NRAO). To ascertain the late time enhancement of flux values, which are much higher than expected from the supernova radio light curve, the VLA data was run using “CASA-EVLA_pipeline1.1.3[1]” of NRAO for all epochs after 2009 September 19. The results from both data reduction procedures are in agreement.

6.3. Results

Tables 6.1 and 6.2 contain the complete VLA and VLBI logs of radio flux measurements of SN 2008iz. The first column in each table lists the observation dates. The second column lists the number of days elapsed since explosion which is estimated to be 2008 February 18 (±6) (Marchili et al., 2010) while the rest of the columns lists the integrated/peak flux density or source size at different frequencies. To minimize the contribution of the diffuse emission in M 82 on the supernova measurements, we use only baselines longer than $30\,\mathrm{k}\lambda$ in the imaging. The AIPS task ‘JMFIT’ is used to determine the flux by fitting a 2D Gaussian to the identified compact supernova source. The flux errors of the VLA observations are derived by adding in quadrature the formal errors from the 2D Gaussian, a 5% systematic error, and a small random error derived as the difference between peak and integrated flux densities. The errors of the VLBI 1.6 GHz fluxes are derived in a similar way; adding in quadrature the formal errors from 2D Gaussian fit to the sources, and a 9% systematic error. However, the supernova is resolved at 4.8 and 8.4 GHz in the VLBI data, thus their integrated fluxes cannot be derived in the same way as for the other observations. In table 6.2, we list the peak intensities at 4.8 and 8.4 GHz.

---

[1] https://science.nrao.edu/facilities/vla/data-processing/pipeline/scripted-pipeline

Table 6.1.: The log of SN 2008iz integrated radio flux measurements observed with VLA.

Date	Age (t-t_0)	Configuration	$S_{1.4GHz}$ (mJy)	$S_{4.8GHz}$ (mJy)	$S_{8.4GHz}$ (mJy)	$S_{22.3GHz}$ (mJy)	S_{35GHz} (mJy)	S_{43GHz} (mJy)
2008/03/24	36	C	–	–	–	100±2	–	–
2008/05/03	76	C	–	–	–	88.4±0.2	–	–
2009/04/08	416	B	–	–	–	9.2±0.2	–	–
2009/04/27	435	B	55±6	30±5	14±3	6.2±0.7	–	2.5±0.4
2009/07/24	523	C	–	21±2	11±1	–	–	1.0±0.6
2009/09/19	580	B	–	14±2	6±2	5±2		1.8±0.5
2009/10/21	612	D	–	–	–	3±1	–	–
2010/10/20	976	C	–	–	–	2.4±0.3	–	1.1±0.2
2010/12/18	1035	C	–	–	10.1±0.9	2.8±0.3	–	1.7±0.4
2011/02/12	1091	B	–	10.2±0.6	7.7±0.7	3.5±0.1	–	0.9±0.2
2011/05/21	1189	AB	23±5	6±2	6.4±0.7	3.1±0.3	–	0.6±0.1
2011/07/30	1259	A	19±3	12.3±0.9	7.5±0.5	–	–	–
2011/08/01	1261	A	17±2	11±1	7.1±0.4	–	–	–
2011/08/09	1269	A	–	–	–	2.3±0.2	–	0.2±0.1
2012/02/02	1446	C	–	–	–	1.9±0.5	0.9±0.2	–
2012/08/25	1651	B	–	12±2	9±2	3.3±0.6	2.0±0.2	–
2012/11/21	1739	A	–	26±1	16.8±0.9	5.0±0.2	2.7±0.2	–
2014/01/23	2167	AB	–	41±7	–	6.5±0.6	–	–

Notes :The data on days 2008 March 24 to 2009 April 27 were already analysed by Brunthaler et al. (2009b) and Brunthaler et al. (2010).

Table 6.2.: The log of SN 2008iz radio flux and angular size measurements obtained from the VLBI observations.

Date	Age (t-t_0)	$S_{1.6GHz}$ (mJy)	$S_{1.6GHz}$ (mJy/b)	$S_{4.8GHz}$ (mJy/b)	$S_{8.4GHz}$ (mJy/b)	$\Theta_{R_{50\%}}$ 4.8GHz (mas)	$\Theta_{R_{50\%}}$ 8.4GHz (mas)
2009/10/04	595	64±6	57.9±0.5	3.02±0.04	0.83±0.04	1.8±0.2	1.7±0.2
2009/12/04	656	55±4	50.9±0.4	2.61±0.03	0.78±0.03	1.9±0.2	1.8±0.1
2010/02/06	720	42±8	34.6±0.2	2.09±0.03	0.59±0.03	2.0±0.2	2.0±0.1
2010/03/20	758	–	–	1.80± 0.03	–	2.3±0.2	–
2010/05/04	807	39±9	30.8±0.2	1.79±0.03	0.58±0.03	2.3±0.2	2.2±0.1
2010/05/29	828	–	–	1.71±0.03	–	2.4±0.2	–
2010/06/07	840	32±8	24.9±0.1	–	–	–	–
2010/07/02	866	35±8	26.5±0.2	4.56±0.05	1.34±0.05	–	2.4±0.2
2010/09/05	931	30±9	20.8±0.1	3.73±0.04	0.56±0.03	2.5±0.2	2.5±0.2
2010/11/19	1006	30±9	21.5±0.1	1.73±0.03	0.41±0.03	2.8±0.2	2.8±0.2
2011/01/07	1055	27±9	17.6±0.1	1.15±0.03	1.02±0.05	2.9±0.3	2.8±0.2
2011/03/18	1125	26±9	17.1±0.1	0.98±0.03	0.41±0.03	3.0±0.3	3.0±0.2
2011/05/12	1180	26±9	17.3±0.2	0.76±0.03	0.33±0.02	3.1±0.3	3.0±0.2
2011/08/14	1274	25±10	15.2±0.1	1.55±0.05	0.57±0.04	–	3.2±0.2
2011/08/14	1274	24±9	15.3±0.1	3.78±0.04	1.18±0.04	–	–
2011/09/23	1314	25±2	12.6±0.1	0.91±0.03	0.29±0.03	3.4±0.3	3.3±0.2
2011/09/23	1314	21±9	12.0±0.1	3.17±0.07	0.90±0.03	–	3.3±0.2
2011/12/19	1401	28±9	18.7±0.2	0.75±0.03	0.35±0.03	3.7±0.6	3.7±0.3
2012/08/25	1650	39±9	30.3±0.3	2.43±0.05	0.73±0.03	4.3±0.4	4.5±0.2
2013/01/28	1806	40±9	21.2±0.1	1.65±0.01	0.69±0.01	8.0±0.4	4.9±0.2

Notes: Both peak and integrated flux density values of our 1.6 GHz are displayed. The peak flux values are presented for the 4.8 GHz and 8.4 GHz measurements because the supernova SN 2008iz was resolved at these frequencies. The $\Theta_{R_{50\%}}$ are the angular sizes derived as the radius of the supernova ring at 50% of the peak intensity on the outside of the bright rim.

6.3.1. Light Curve

The light curve of SN 2008iz is well fit by a power-law of the form,

$$S = K_0 \left(\frac{t - t_0}{1\,day} \right)^{\beta} \tag{6.3.1}$$

especially in the well sampled optically thin regime, i.e. 5 and 22 GHz (see Fig. 6.3.1). K_0 is a flux scaling factor which does not change the overall behaviour of the fit, (t−t_0) is the time elapsed after the explosion date, while β is the flux decay index. The obtained fit results (see Fig. 6.3.1) with β and K_0 as free parameter at 5 GHz (100 – 1500 days) are

$K_{0\,5GHz}$= (6.29±2.22)×10^4 mJy and β=−1.22±0.07. The time range 0-100 days is excluded because the radio emission from the supernova shock wave was still within the optically-thick regime, while the last epochs of the data sets have their peak intensity higher than expected from the light curve. The obtained fit value at 22 GHz (50 – 1500 days) with both β and K_0 as free parameters yields $K_{0\,22GHz}$= (1.46±0.33)×10^4 mJy and β=−1.18±0.05. Considering the 5 GHz data set, which is better sampled over the time range than the one at 22 GHz, we adopt a β value of −1.22±0.07 to be more representative. Fitting the 22 GHz data with our adopted β value, we obtain the scaling parameter $K_{0\,22GHz}$ to be (1.73±0.10)×10^4 mJy. A fit to all frequencies (Fig. 6.3.2) using one single β value of -1.22±0.07 yields a different K_0 value for each frequency. The values of K_0 are $K_{0\,1.4GHz}$= (1.19±0.60)×10^5 mJy, $K_{0\,5GHz}$= (6.19±0.17)×10^4 mJy, $K_{0\,8.4GHz}$= (3.57±0.40)×10^4 mJy, $K_{0\,22GHz}$= (1.73±0.1)×10^4 mJy, and $K_{0\,43GHz}$= (3.77±0.52)×10^3 mJy. The derived scaling factor K_0 yields a normalised average spectrum that depends on frequency as shown in Fig.6.3.3.

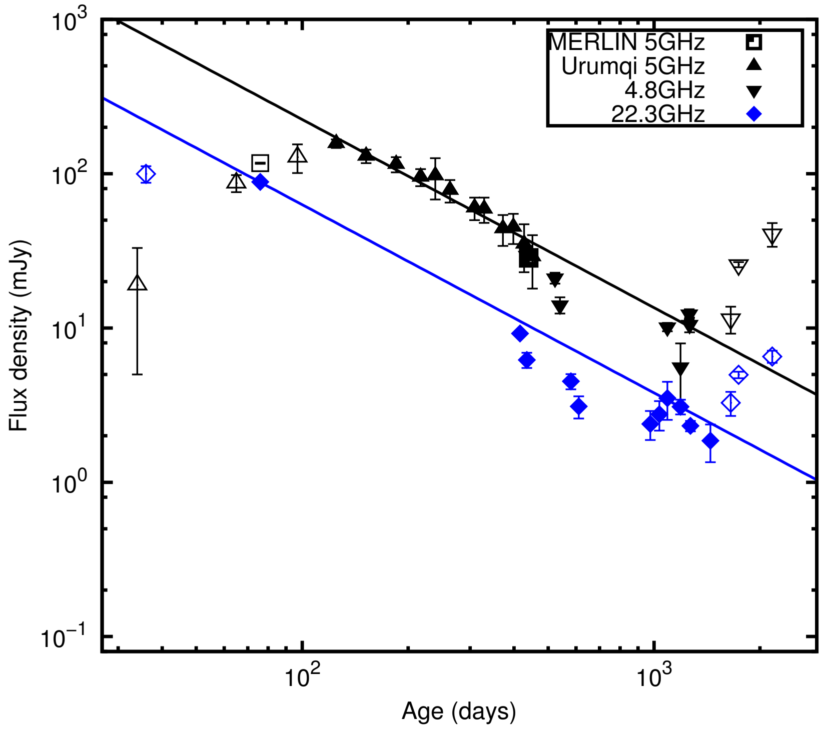

Figure 6.3.1.: Fits to the light curve of the optically-thin regime of SN2008iz at 5 and 22 GHz.β and K_0 (see equation 1) are derived from the fit to the data over the range of 100-1500 days for 5 GHz and 60-1500 days for 22 GHz. The fitted data are shown as filled symbols, while the data not used to fit are shown as open symbols. The MERLIN 5 GHz data were obtained by Beswick et al. (2009), and the Urumqi 5 GHz data by Marchili et al. (2010). The rest of the data are tabulated in Table 6.1.

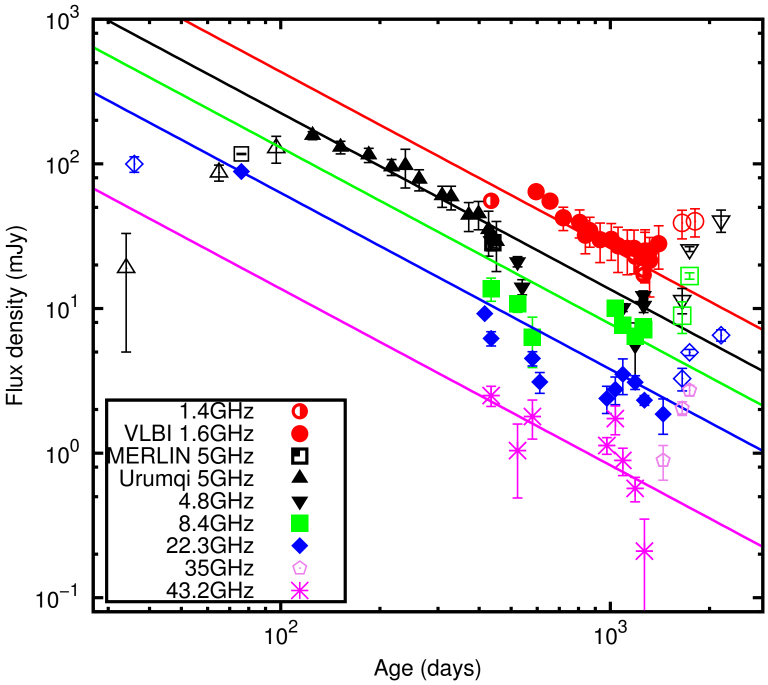

Figure 6.3.2.: A combined multi-frequency light curve for the optically-thin regime of SN 2008iz. The fitted data are shown as filled symbols, while the data not used to fit are shown as open symbols. The data sources are indicated in Fig 6.3.1, while the 1.6 GHz VLBI data are tabulated in Table 6.2.The lines represent simple power law fits to the data at the different frequencies as color coded in the legend.

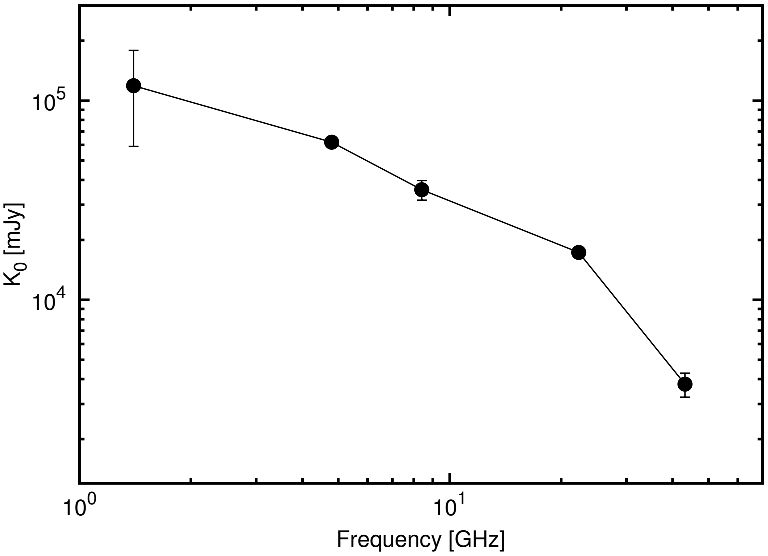

Figure 6.3.3.: The normalized average spectrum of the variation of K_0 with frequency for the optically-thin power-law model.

Although the simple power-law (equation 6.3.1) describes the optically-thin regime of the light curve very well, a complete fit to the supernova light curve model is not possible because we have data for only very few epochs in the optically-thick regime. For the complete radio light curve, we fit the simplified Weiler model (Weiler et al., 2007) described as

$$S_{(\nu)} = K_1 \left(\frac{\nu}{5\,GHz} \right)^{\alpha} \left(\frac{t - t_0}{1\,day} \right)^{\beta} e^{-\tau} \tag{6.3.2}$$

where K_1 is a scaling factor in Jy and α is the spectral index of the emission in the optically-thin regime. The exponent β is related to the flux density drop at late epochs, normally affected by both the spectral index, α, and the opacity, τ. The date of explosion is denoted as t_0 and t is the epoch of observation. The opacity of thermal electrons of the circumstellar medium (CSM) in equation 6.3.2 is modeled as

$$\tau = K_2 \left(\frac{\nu}{5\,GHz} \right)^{-2.1} \left(\frac{t - t_0}{1\,day} \right)^{\delta} \tag{6.3.3}$$

where K_2 is the scaling factor and δ is the absorption decline index related to the CSM radial density profile derived as $\delta = \alpha - \beta - 3$. The exponent -2.1 corresponds to the spectral dependence of FFA by thermal ionised gas in the radio regime.

To constrain the simplified Weiler model, we apply the best fit parameters of the model 6.3.2 and 6.3.3 obtained by (Marchili et al., 2010) at 5 GHz (i.e. K_1=$(2.14\pm0.04)\times10^5$ mJy, $\beta=-1.43\pm0.05$, t_0=18 Feb 2008, K_2=$(11.0\pm0.7)\times10^4$ mJy, $\delta=-2.65\pm0.10$) and from (Brunthaler et al., 2010) we obtain the spectral index, $\alpha=-1.08\pm0.08$. We fit all frequencies at the same time as shown in Fig.6.3.4 using β as a free parameter, for which a value of -1.41 ± 0.02 is determined.

The model fits satisfactorily the flux density decline from day 500 except for the 1.4 GHz observations that fall well below the model fit on Fig. 6.3.4. The lower flux densities at 1.4 GHz are also confirmed by a 3σ LOFAR non-detection limit of SN2008iz at a level of 0.41mJy/beam at the even lower frequency of 154 MHz (Varenius et al., 2015). The plausible explanations could be FFA from a dense foreground screen along the line of sight. Other effects, like low-frequency cut-off caused by Razin-Tsytovich effect could also help explain the lower 1.4 GHz flux and LOFAR non-detection. From the same figure, the observations at 43.2 GHz drop quite fast past ~1000 days. This drop is most likely related to synchrotron ageing of the emitting electrons in the shocked CSM.

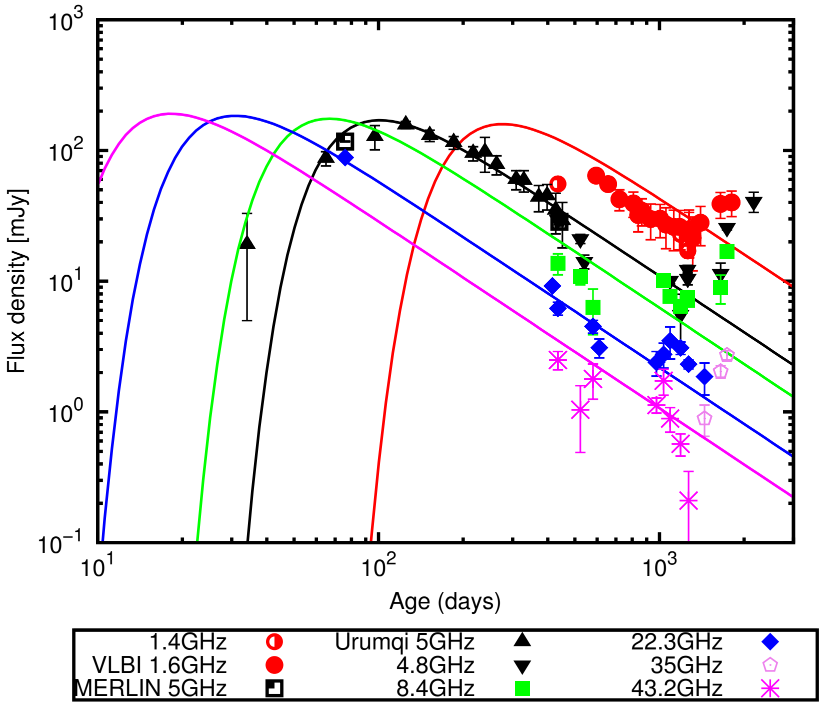

Figure 6.3.4.: The multi-frequency light curve of SN 2008iz. The MERLIN 5 GHz data is taken from Beswick et al. (2009), the Urumqi 5 GHz data from Marchili et al. (2010). The rest of the data are tabulated in table 6.1 and 6.2above. The black line represents a Weiler model fit to 5 GHz data obtained by Marchili et al. (2010) with Urumqi telescope. The other lines represent light curves calculated using the equations in the text for the other frequency data sets as color coded in the legend

6.3.2. SN 2008iz Size Estimate

Estimating the physical size of a supernova from a VLBI data is not a straight forward exercise. For a detailed discussion of the different methods applied in determining the supernova size, the reader is referred to Brunthaler et al., 2010. Typically, imaging of data is done using the beam size given by the antennas that worked for the considered data set and band. This will results to different resolutions of the structure of the supernova as it expands, which introduces systematic errors in the analysis. To avoid such errors, a dynamic beam is used. A dynamic beam scales the resolution of the later epochs to the resolution of the first epoch with respect to the size of the supernova shell size before imaging. The dynamic beam eliminates the systematic errors that would otherwise arise from the different resolutions with which the SNR was imaged while it expands. For detailed discussion on the VLBA imaging and size estimates of SN 2008iz see Sendlinger (2013) Masters thesis.

The deceleration of SN 2008iz is derived from the resolved VLBI images convolved with a dynamic beam at 4.8 and 8.4 GHz. To obtain the size of the supernova, we first measured the intensity in the concentric rings (of 0.25 mas width) using the AIPS task ‘IRING’. Examples of the intensity profiles for two observations are shown in Fig. 6.3.5 together with fits to the data. The center of the supernova had been confirmed from earlier observations to be stationary over the time span of our observations. We take the radius of the supernova ring at 50% (R$_{50\%}$) of the peak intensity since this is the real ring size times an unknown factor. This method is more reliable than taking the maximum of the ring as the radius due to position uncertainties at the turning point (see a more detailed description in Brunthaler et al., 2010).

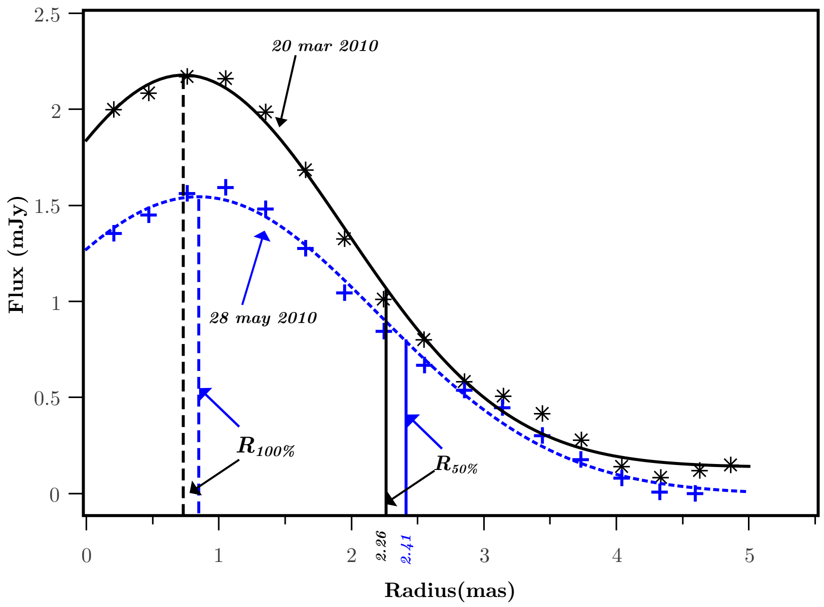

Figure 6.3.5.: The intensity of concentric rings of widths 0.25 mas in the images from 2010 March 20 and 2010 May 29. The vertical lines mark the position of the peak and the radius where the intensity is 50% of the peak level.

6.3.3. Deceleration of SN 2008iz

The VLBI images of SN 2008iz at 4.8 and 8.4 GHz are shown in Figs.6.3.7 and 6.3.8, respectively. All the images are phase referenced to M81 for consistency in their alignment. The SNR is resolved at these frequencies. We use natural weighting in order to reveal more information on the larger scale structures. The size and shape of the beam used for restoring the images is determined by the set of antennas that were employed for each of the the considered data set. For instance, the resolution of images Figs.6.3.7 e, f and 6.3.8 e and h is lower because some telescopes especially the Effelsberg 100 meter telescope have not taken part in the observations.

The images show that the supernova expansion starts with a shell like structure that gets more and more asymmetric, Overall, we see expansion with similar velocities into all directions. During the later epochs, the emission distribution breaks up and shows substructures in the southern part of the ring. There, the ring is much brighter than in its other parts, indicating a denser surrounding medium along the southern direction.

The deceleration of SN 2008iz is derived from the images convolved with a dynamic beam at 4.8 and 8.4 GHz VLBI as described in section 6.3.2. We fit a power-law of the form

$$\mathrm{R_{50\%} = c_y(t - t_0)^m} \tag{6.3.4}$$

to the size evolution of SN 2008iz, where c_y is a scaling factor, (t-t_0) is the time elapsed after the explosion date and m is the deceleration index. We derive values of c_y=(7.5±0.9)× 10^{-6} arcsec/day and m=0.86±0.02. The errors are obtained from the post-fit covariance matrix. The size evolution and deceleration of SN 2008iz are displayed in Fig. 6.3.6. Also shown are two 22 GHz data points from Brunthaler et al. (2010) that were included in the analysis. The last two data points were excluded from the fit since we know from the light curve that there is a change in the surrounding medium of SN 2008iz at around 1400 days after the explosion that is not caused by internal processes.

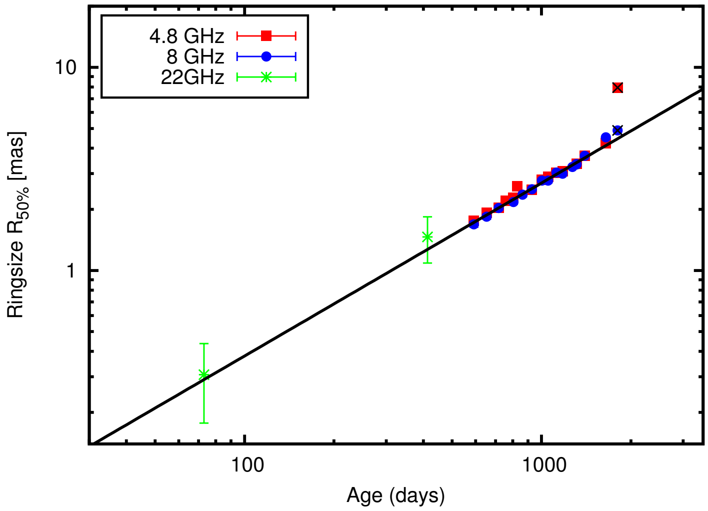

Figure 6.3.6.: The expansion curve of SN 2008iz. The two data points at 22 GHz were taken from Brunthaler et al. (2010), while the last two data points (overlaid with a black ‘x’ symbol) were excluded from the fit.

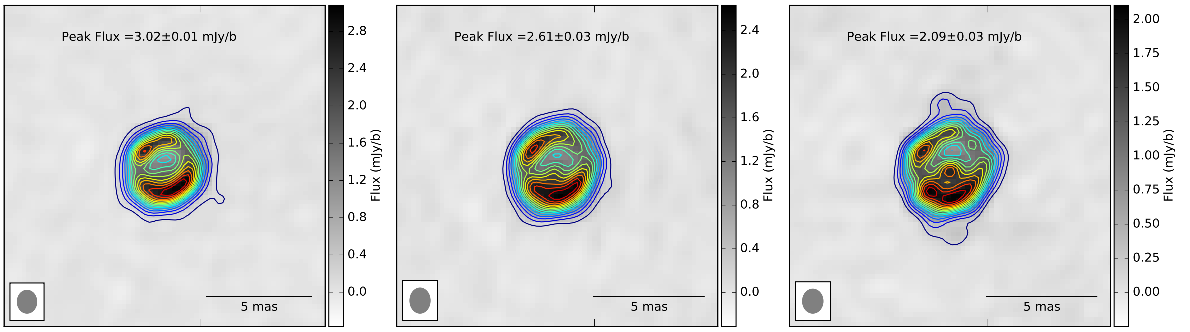

(a) Day 595 (b) Day 656 (c) Day 720

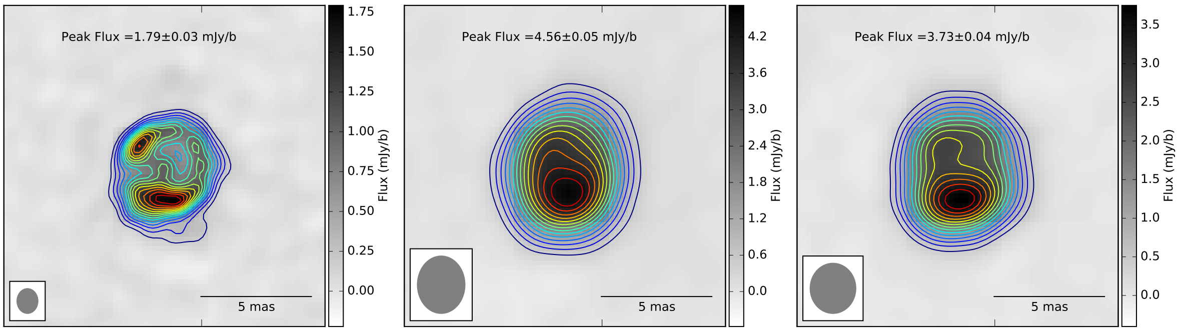

(d) Day 807 (e) Day 866 (f) Day 931

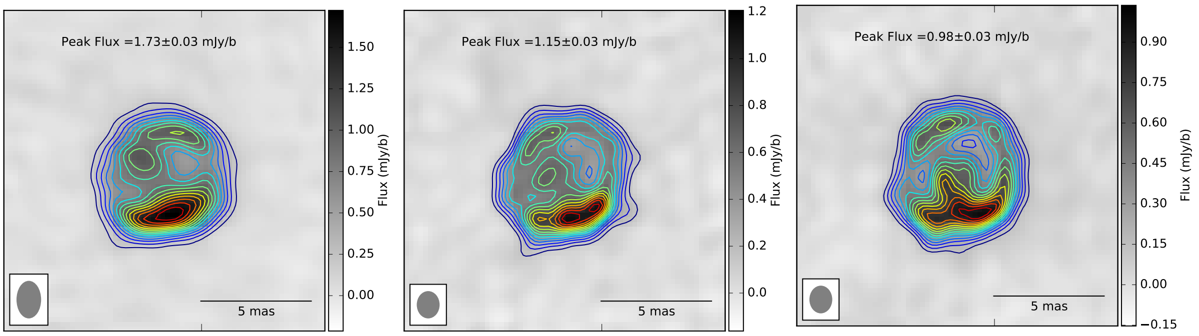

(g) Day 1006 (h) Day 1055 (i) Day 1125

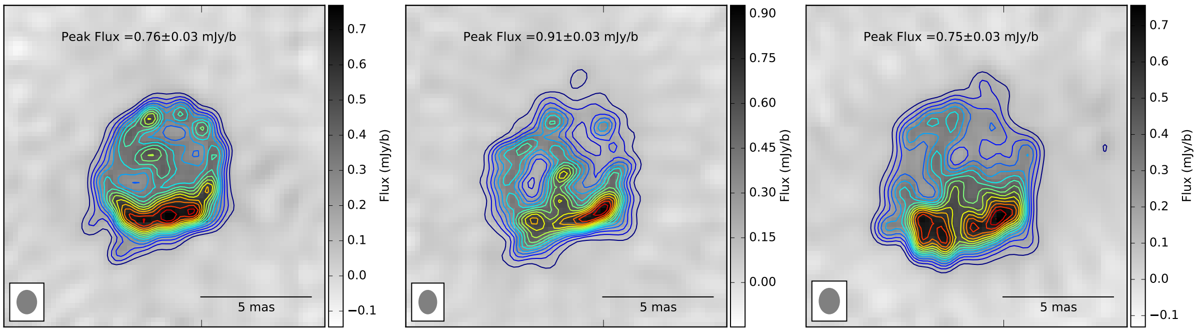

(j) Day 1180 (k) Day 1314 (l) Day 1401

Figure 6.3.7.: Continued

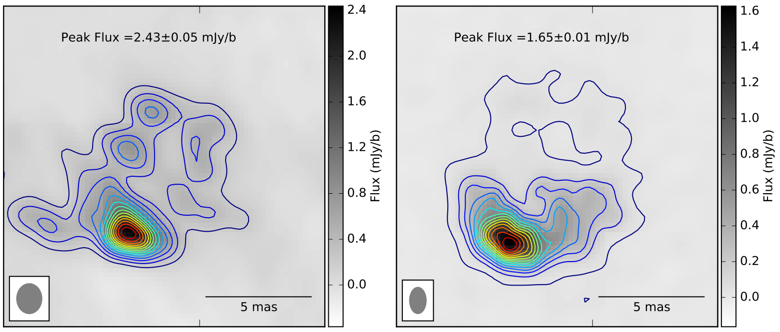

(m) Day 1650 (n) Day 1806

Figure 6.3.7.: The natural weighted VLBI images of the expanding shell produced by supernova SN 2008iz at 4.8 GHz. They cover the observation periods between 2009 October and 2013 January as summarized in Table 6.2. The figures show the 4.8 GHz linear gray scale images overlaid with their contour maps that scale to the peak intensity at each epoch (listed in each panel). All image contours correspond to 6% of the peak intensity (lowest contour) and subsequent increases by 6%. The images have been convolved with the natural weighting beam, shown at the bottom left of each panel.

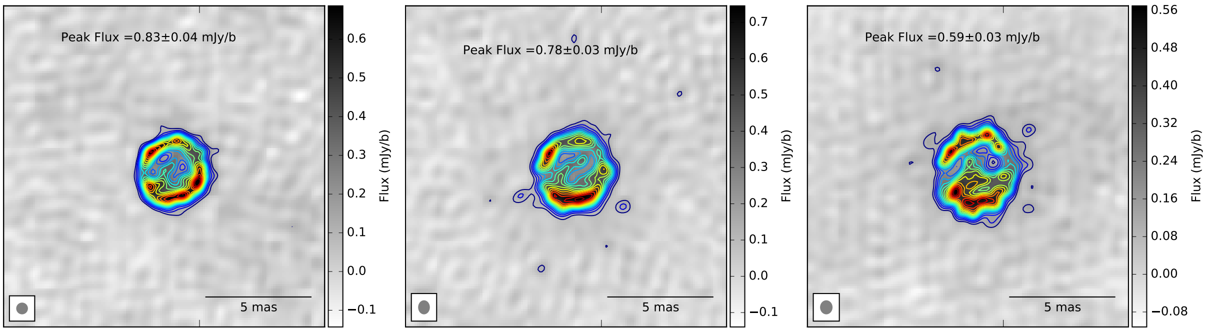

(a) Day 595 (b) Day 656 (c) Day 720

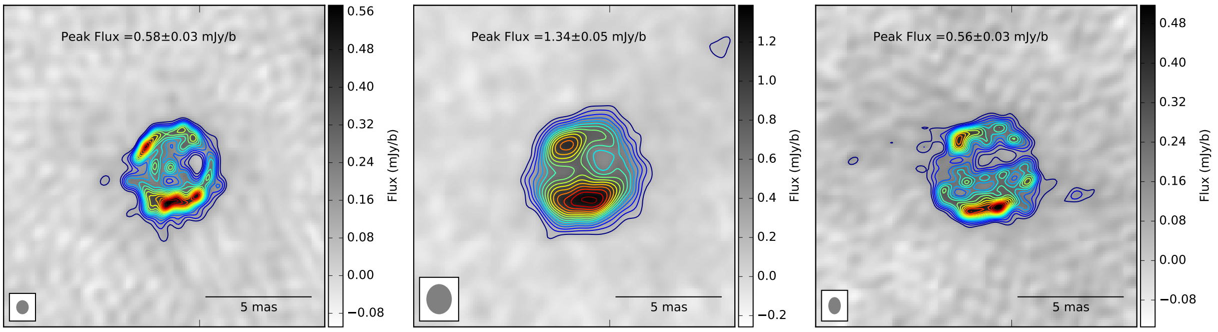

(d) Day 807 (e) Day 866 (f) Day 931

Figure 6.3.8.: Continued

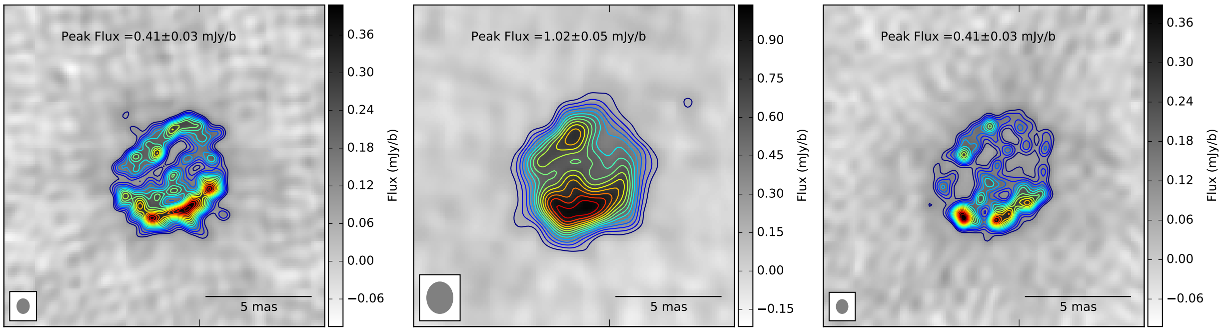

(g) Day 1006 (h) Day 1055 (i) Day 1125

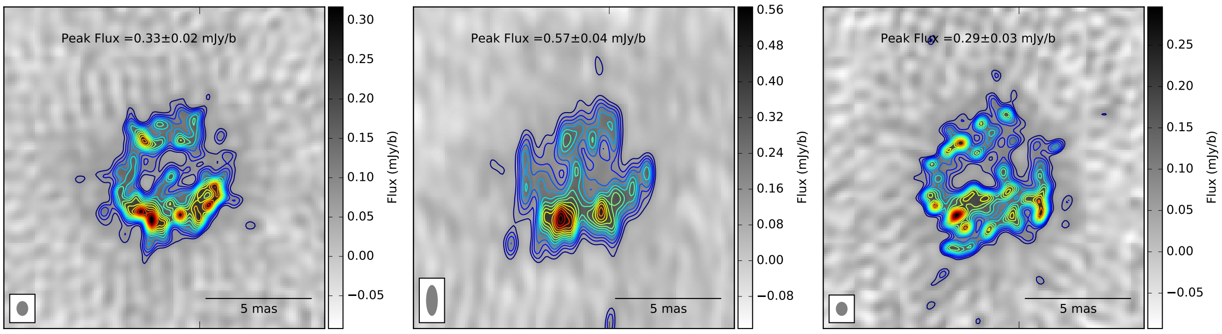

(j) Day 1180 (k) Day 1274 (l) Day 1314

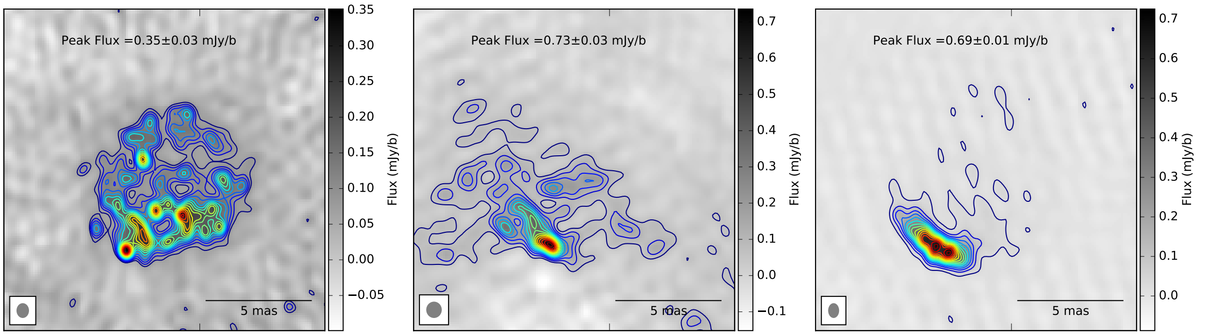

(m) Day 1401 (n) Day 1650 (o) Day 1806

Figure 6.3.8.: The natural weighted VLBI images of the expanding shell produced by supernova SN 2008iz at 8.4 GHz. They cover the observation periods between 2009 October and 2013 January as summarized in Table 6.2. The figures show the 8.4 GHz linear gray scale images overlaid with their contour maps that scale to the peak intensity at each epoch (listed in each panel). All image contours correspond to 6% of the peak intensity (lowest contour) and subsequent increases by 6%. The images have been convolved with the natural weighting beam, shown at the bottom left of each panel.

6.4. Discussion

6.4.1. Flux-density flare at later date

A zoom into the light curve at the higher frequencies (see Fig.6.4.1) uncovers excess emission from the supernova after t=970 days and after t=1400 days. We note that the extra emission after t=970 days is detected at 8.4, 22.3 and 43.2 GHz while the enhancement at t=1400 days is detected at 4.8, 8.4, 22 and 35 GHz. The later flare after time $\geq$ 1400 days is also confirmed with our very well sampled VLBI 1.6 GHz results. The extra emission increases the total flux density of the supernova by a factor of $\sim$2 at t=970 days, lasting for about 240 days. The second flare increases the total flux density by a factor of $\sim$4, without showing signs of flux decline so far, i.e., in 2014 January. This calls for a continuation of the monitoring to determine how long the second flare lasts.

The source is obviously optically-thin at all frequencies during the flares and its spectral index remains steep (see section 6.4.2). Weiler et al. (2002) indicate that a supernova whose radio emission preserves its spectral index while deviating from the standard model is showing evidence for a change in the conditions of the CSM that its remnant expands into. We therefore examine the changes in the density of the CSM as the explanation to the observed flares. According to Chevalier (1982), radio luminosity is related to the average CSM density ($\rho_{csm} \propto \dot{\mathrm{M}}/\mathrm{w}$) through

$$\mathrm{L} \propto \left(\frac{\dot{\mathrm{M}}}{\mathrm{w}}\right)^{(\gamma-7+12\mathrm{m})/4} \tag{6.4.1}$$

where the relativistic particle index $\gamma=1-2\alpha$, $\alpha=-1.08\pm0.08$ and expansion index $m=0.86\pm0.02$. For SN 2008iz, $\mathrm{L} \propto (\dot{M}/\mathrm{w})^{1.62}$. Consequently, for the radio emission to double its flux in the first flare, the CSM density must have increased by a factor of 1.5, while for the increase by factor of 4 in second flare, the CSM density must have tripled. However, the VLBI images of the remnant of SN 2008iz do not show a spherically-symmetric density enhancement. This suggests that the shock wave is encountering dense inhomogeneities in the CSM.

The late flare (day 1400), may also be related to the transition of the front shock from the CSM bubble into the ISM. This would enhance the magnetic field and increase the emission at all frequencies. However, we obtain the size of the shock on day 1400 is $\sim$0.06 pc (3.6 mas), which is very small compared to the supernova remnant sizes measured by Batejat et al. (2011) of $\sim$0.4 pc in Arp 220 at the transition. Were the flare related to the transition, this indicates the presence of a very dense ISM for the pressure balance to hold at the bubble boundary of SN 2008iz. Thus we require an ISM with a density higher than the characteristic one in Arp 220 of 10^4cm^{-3} to explain the light curve of SN 2008iz at late stages, in the frame of the ISM interaction model.

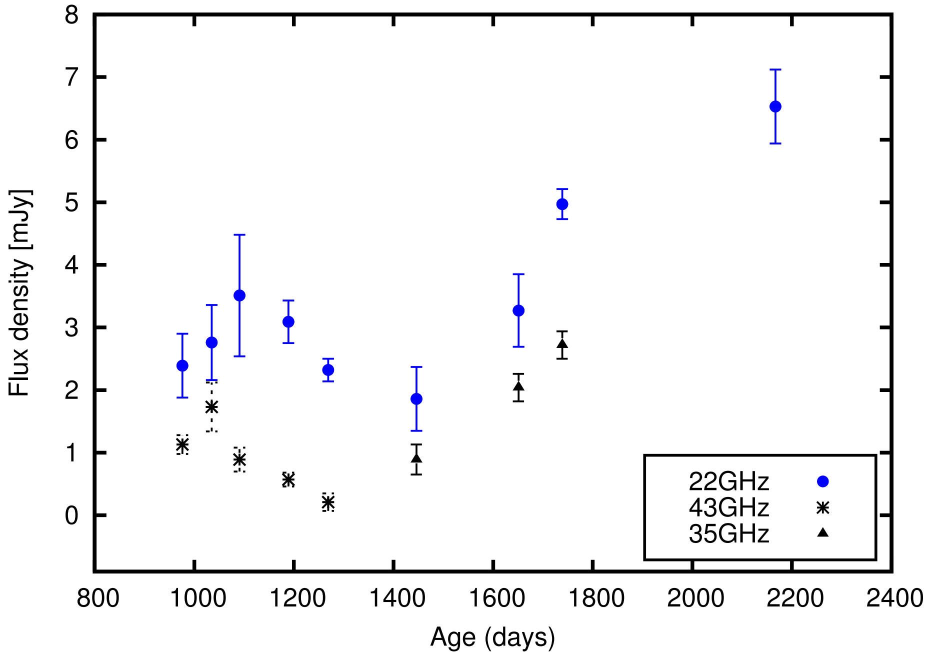

Figure 6.4.1.: A zoom into our higher frequency light curve for a period between t=800 to t=2400 days. The flux density enhancement at t≥1400 days was detected in both VLA and VLBA results at all frequencies.

6.4.2. Evolution of spectral index

Figure 6.4.2 shows the best fit radio spectral index, α, for SN 2008iz from ∼430 days up to 2167 days. To obtain the radio spectral index we fit a simple power-law spectrum of the form ($S = S_0\nu^{\alpha}$) to our VLA data for all the epochs except for epoch 2009 April 27 which was best fit with a broken power-law of the form

$$S = S_0 \left(\frac{\nu}{\nu_0}\right)^{\alpha} \left(1 - e^{-\left(\frac{\nu}{\nu_0}\right)^{\delta-\alpha}}\right) \tag{6.4.2}$$

as presented by Brunthaler et al. (2010). We fit this expression to our data with the S_0 and α are left as free parameters. For epochs with two or three frequency data points only, i.e. 2010 October 20, 2010 December 18, 2011 July 30 and 2011 August 01, a systematic error of 30% was added to the fit error to account for the low data statistics. This causes the data points for those epochs to have slightly larger error bars compared to the epochs with more frequency data points whose errors are derived directly from the post-fit covariance matrix. The observed spectral index does not show signs of evolution and remains steep, i.e. $\alpha{\sim}-1$ throughout the period. This steepness seems to persist persist longer than in the the case of SN 1993J, whose spectral index evolution shows flattening at all frequencies beginning at an age ~970 days (Alberdi and Marcaide, 2005, Martí-Vidal et al., 2011b, Weiler et al., 2007)

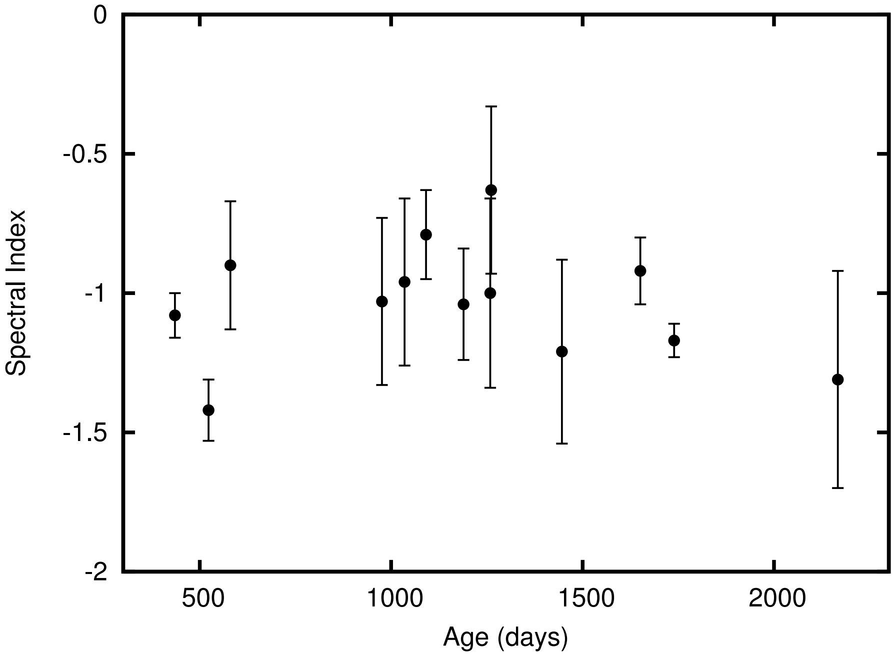

Figure 6.4.2.: The spectral index, α, for SN 2008iz obtained from fitting a simple power law fit to the radio continuum data at each epoch. The spectral index remains steep, near $\alpha = -1$.

6.4.3. Equipartition total minimum Energy and Magnetic field

For sources of radio synchrotron emission, energy equipartition between the particles and the magnetic field is usually postulated (Pacholczyk, 1970). The total minimum energy content ($\mathrm{E_{min}}$) and magnetic field ($\mathrm{B_{eq}}$) in SN 2008iz can be expressed as given in relations 6.4.3 and 6.4.4

$$E_{min} = c_{13}(1+k)^{4/7}\phi^{3/7}R^{9/7}L^{4/7} \tag{6.4.3}$$

and

$$B_{eq} = 4.5^{2/7}c_{12}^{2/7}(1+k)^{2/7}\phi^{-2/7}R^{-6/7}L^{2/7} \tag{6.4.4}$$

where parameters c_{12} and c_{13} are 9.3×10^7 and 3.3×10^4 respectively (Pacholczyk, 1970) for spectral index, $\alpha\sim-1$. The filling factor, ϕ, the ratio of the inner and outer radii of the emitting region, is estimated as 0.3 (Marchili et al., 2010). R is the source radius in cm derived from our VLBI data $R_{50\%}$, which predicts m=0.86±0.02 and $c_y=(7.5\pm0.9)\times10^{-6}$ arcsec/day in agreement with previous derivations from Brunthaler et al. (2010) of m=0.89±0.03. L is the integrated radio luminosity in $\mathrm{erg\,s^{-1}}$ between the radio synchrotron cutoff frequencies $\nu_{\rm min}=10^7$ Hz and $\nu_{\rm max}=10^{11}$ Hz. k is the ratio between the relativistic heavy particle energy density to the relativistic electron energy density. The parameter k is dependent on masses of the particles, and varies from $m_p/m_e\approx1$ to $m_p/m_e\approx2\times10^3$ (Marchili et al., 2010). With varying value of k, we cannot compute a single value of total minimum energy and equipartition magnetic field, but can only give a range of possibilities (see table 6.3). The derived E_{min} values are in the range of $\sim10^{46}$ – $\sim10^{48}$ erg. Our results of B_{eq} at 2008 May 3, which range between 0.25 G and 1.78 G, are comparable to the values derived byMarchili et al. (2010) at 5 GHz of 0.3 G and 2.1 G and also on 2009 April 8 between 0.04 G and 0.27 G, compared to 0.04 G and 0.31 G respectively. Figure 6.4.3 shows the magnetic field evolution as the supernova ages derived from the integrated 22.3 GHz flux densities from day ∼36 to ∼2200 after the explosion. From this figure, we notice that the magnetic fields at each epoch scale with time, showing a hint of flattening in the time $\geq$ day 1300. This flattening corresponds to the flux-density flare events when the shock interacts with dense CSM. However, assuming a constant k value, the magnetic field generally decreases according to $B\propto t^{-1}$ on the full time range.

Considering the equipartition between fields and particles, the B_{eq} range between (37 – 266) mG on 2009 April 8 (day 416) is expected to explain the observed level of radio emission. The choice of the radius which is $\sim7.2\times10^{16}$ cm, allows for a comparison with other supernovae at about the same point of expansion. The energy density of the magnetic field in the remnant is postulated to be lower than the kinetic energy density (i.e. $\rho_{csm}\upsilon_{csm}^2/2 \gtrsim B_{csm}^2/8\pi$), such that

$$B_{csm} \lesssim \frac{(\dot{M}\upsilon_w)^{1/2}}{r} = 2.5\left(\frac{\dot{M}}{10^{-5}M_\odot\,yr^{-1}}\right)^{1/2}\left(\frac{\upsilon_w}{10\,km\,s^{-1}}\right)^{1/2}\left(\frac{r}{10^{16}cm}\right)^{-1}\,mG. \quad (6.4.5)$$

Using a mass-loss of the progenitor of SN2008iz of $\sim3.69\times10^{-5}M_\odot yr^{-1}$(Marchili et al., 2010), a standard pre-supernova wind velocity υ_w of $10\,km\,s^{-1}$, and a standard CSM density profile of $\rho_{wind}\propto r^{-2}$, we obtain B_{csm}= 0.67 mG, which is a factor of about 55 – 400 times smaller than the equipartition field. This indicates that the magnetic field inferred for SN 2008iz cannot originate solely from compression of the existing circumstellar magnetic field, which is predicted to increase the field only by a factor of 4 (Dyson and Williams, 1980). Large amplification factors of the magnetic field have also been found for other radio supernova: for SN 2001gd an amplification factor in the range of 50-350 was determined (Pérez-Torres et al., 2005); the SN 1993J amplification factor of a few hundred (Fransson and Björnsson, 1998; Pérez-Torres et al., 2001); for SN 1986J values in the range of 40–300 (Pérez-Torres et al., 2002); for SN 1979C in the range of 50 – 400 (Pérez-Torres et al., 2005); and between 37 and 260 for SN 2004et (Martí-Vidal et al., 2007). Thus, if equipartition between fields and particles holds, amplification mechanisms other than compression of the circumstellar magnetic field need to be invoked to explain the level of radio emission from the supernova, such as turbulent amplification due to Rayleigh-Taylor instability (Chevalier, 1982; Chevalier and Blondin, 1995).

Table 6.3.: The SN 2008iz derived equipartition total minimum energy and magnetic fields.

Date (yy/mm/dd)	Days After 18-2-2008	Radius (cm)	Luminosity (ergs^{-1})	B$_{eq}$ $(G)_{k=1}$	B$_{eq}$ $(G)_{k=2000}$	E$_{min}$ $(ergs^{-1})_{k=1}$	E$_{min}$ $(ergs^{-1})_{k=2000}$
2008/03/24	36	0.88×10^{16}	142.6×10^{35}	0.444	3.197	1.58×10^{46}	0.82×10^{48}
2008/05/03	76	1.67×10^{16}	126.6×10^{35}	0.248	1.784	3.35×10^{46}	1.74×10^{48}
2009/04/08	416	7.22×10^{16}	13.2×10^{35}	0.037	0.266	6.05×10^{46}	3.14×10^{48}
2009/04/27	435	7.51×10^{16}	8.9×10^{35}	0.032	0.230	5.08×10^{46}	2.63×10^{48}
2009/09/19	580	9.61×10^{16}	6.5×10^{35}	0.024	0.170	5.83×10^{46}	3.02×10^{48}
2009/10/21	612	10.07×10^{16}	4.4×10^{35}	0.020	0.146	4.96×10^{46}	2.57×10^{48}
2010/10/20	976	15.04×10^{16}	3.4×10^{35}	0.013	0.096	7.16×10^{46}	3.71×10^{48}
2010/12/18	1035	15.82×10^{16}	4.0×10^{35}	0.013	0.097	8.39×10^{46}	4.35×10^{48}
2011/02/12	1091	16.55×10^{16}	5.0×10^{35}	0.014	0.099	10.10×10^{46}	5.23×10^{48}
2011/05/21	1189	17.82×10^{16}	4.4×10^{35}	0.012	0.090	10.32×10^{46}	5.35×10^{48}
2011/08/09	1269	18.85×10^{16}	3.3×10^{35}	0.011	0.079	9.42×10^{46}	4.88×10^{48}
2012/02/02	1446	21.09×10^{16}	2.7×10^{35}	0.009	0.068	9.70×10^{46}	5.03×10^{48}
2012/08/25	1651	23.64×10^{16}	4.7×10^{35}	0.010	0.072	15.42×10^{46}	7.99×10^{48}
2012/11/21	1739	24.72×10^{16}	7.1×10^{35}	0.011	0.078	20.67×10^{46}	10.71×10^{48}
2014/01/23	2167	29.90×10^{16}	9.1×10^{35}	0.010	0.071	30.23×10^{46}	15.66×10^{48}

Notes :The luminosity is derived from the 22.2 GHz integrated flux values, while the radius is derived from the VLBI results by assuming a constant expansion index m=0.86±0.02 and c_y=(7.5±0.9)$\times10^{-6}$ arcsec/day.

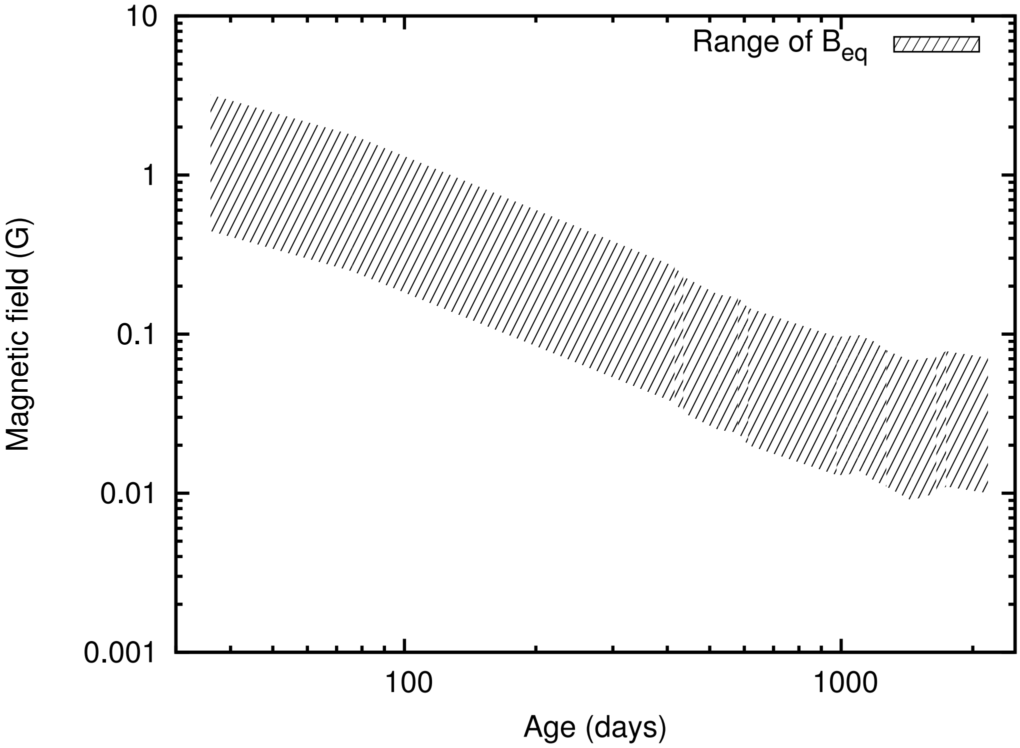

Figure 6.4.3.: The 22 GHz evolution of the magnetic field in the synchrotron emitting plasma of SN 2008iz with time. The magnetic field evolution is roughly consistent with $B \propto t^{-1}$ assuming a fixed *k* value and show signs of flattening past day ≈970.

7. Summary

In this thesis, we have demonstrated some powerful scientific applications of multi-epoch multi-frequency Very Long Baseline Interferometry (VLBI) and Very Large Array (VLA) radio observations. The main focus was;

- obtaining the proper motion of M 81 relative to the Milky Way galaxy,
- obtaining the proper motion of M 82 relative to M 81,
- deriving an orbital lower mass estimate to the mass of M 81, and
- studying the evolution of radio supernova SN 2008iz in M 82.

The first part of this work falls under a broader project that is aimed at measuring the 3-dimensional velocities of galaxies in the local universe, a necessary step towards a better kinematic model of the local volume. This was started by obtaining proper motion of M 33 and IC 10 in the Local Group (Brunthaler et al., 2005b, 2007). The next target was galaxies beyond the Local Group with priority given to the nearest group (M 81 group). This work presents the results of the first-ever relative proper motion measurement of galaxies outside of the local group.

The kinematics study of M 81 group, at a distance of 3.6 Mpc, required us to attain μas astrometry precision for a possible detection of proper motion. Such high accuracy is only achieved by the use of high resolution VLBI phase-referencing technique. This technique requires the availability of either a compact radio source or strong maser emission in the target source and, additionally, compact extra-galactic radio sources that serve as an ideal reference frame (see section 2.3.1). M 81 is known to harbour an extremely compact radio source at its nucleus (M 81*), and has a number of bright background quasar sources within its proximity. M 82 is known to host several strong water maser sources, within a range of 70 to 363 $\mathrm{km\,s^{-1}}$. Observations were done using the VLBA antennas, the Green Bank 100 m telescope, the Effelsberg 100 m telescope and the phased 27 VLA antennas. The inclusion of non-VLBA antennas, which have the largest collecting area, was to increase the sensitivity of the array in order to detect as many maser features as possible. Throughout the observations, M 81* was used as the phase-referencing source with all the target sources being within a degree. The small angular separation of the sources in the sky reduces significantly the systematic sources of error when determining the relative positions. The observations that were conducted at K-band (22 GHz) involved rapid switching between the phase-calibrator M 81*, source (M 82), and three background quasars (0945+6924, 0948+6848, and 1004+6936), over a total observing time of 12 hours per epoch. The switching time between sources was 50 seconds, following the sequence M 81* – M 82 – M 81* – 0945+6924 – M 81* – 0948+6848 – M 81* – M 82 – M 81* – 1004+6936 – M 81*. To estimate the amount of zenith delay error, we used geodetic-block data that comprised of 13–18 strong quasars at different elevation in the sky, that were observed at the beginning, in the middle, and at the end of the main observation. The data was edited and calibrated using ParselTongue run Python-based script called "BeSSeL-master.2.2.0.py" which follows the standard technique in Astronomical Image Processing System (AIPS).

7.1. Proper motion of M 81

To obtain the μas proper motion measurements of M 81 relative to the Milky Way galaxy, we used M 81* and three background quasars (0945+6924, 0948+6848, and 1004+6936). These three background quasars were assumed to be stationary in the sky given their large distance, which makes the inverse of their averaged motion to describe the motion of M 81. At the beginning, the observations were conducted for three consecutive years (i.e. 2007 – 2009), once per year at 8.4, 15.3 and 22.2 GHz. These three epochs of data enabled us to determine the time dependent stability of the structure of M 81*, and also confirm if its brightness peak position varied with frequency. We obtained the difference in the position offsets of quasars at 8.4 and 15 GHz against their 22 GHz offsets. A plot of the averaged position offsets of the brightness peak at each epoch and frequency are only in one direction (see Fig. 4.2.1). This is a result of the frequency dependence of the brightness peak of M 81*, with the position of the core located towards the south-western direction with increasing frequency in agreement with Bietenholz et al. (2004). This shows that the phase-referencing source is stable, hence we dropped the 8.4 and 15 GHz observations in the subsequent epochs.

On 2015 December 21 and 27, the observations were conducted at 22.2 GHz. This epoch allowed for an interpolation of 8 years at that frequency. We obtained the position offsets of the three quasars relative to the phase-reference source M 81*. By fitting a rectilinear motion to the positions, the proper motion of the quasars were derived. The east-west proper motion were in agreement in all quasars within the errors. However, the north-south motion for quasar 0948+6848 was unusually high compared to the other two. From the morphological structure (see Fig. 4.2.3), it was evident that quasar 0948+6848 hosts a south-north jet structure, whose internal jet motion must have been detected. The proper motion of quasar 0948+6848 was excluded when deriving the M 81 galaxy proper motion because our measurement was contaminated. The rectilinear fit errors were considered non-representative due to the low number statistics. We therefore derived the accuracies from the standard deviation of the fit results. We averaged the observed proper motion of the two quasars to obtain the relative proper motion of M 81 as μ_α=0±5.7 μas yr^{-1} and μ_δ=−22.5±2.1 μas yr^{-1} at 22.2 GHz. Correcting for the peculiar motion of the Sun and the rotation of the Milky Way of −10.2±0.6 μas yr^{-1}in right ascension and 2.0±0.5 μas yr^{-1} in declination, we obtain M 81 proper motion relative to the Milky Way of $\dot{\alpha}_{\rm M81} = 10.2 \pm 5.7\,\mu{\rm as\,yr^{-1}}(\sim 179 \pm 100\,{\rm km\,s^{-1}})$ and $\dot{\delta}_{\rm M81} = -24.5 \pm 2.2\,\mu{\rm as\,yr^{-1}}(\sim -429 \pm 39\,{\rm km\,s^{-1}})$.

From these results, the proper motion of M 81 relative to the Milky Way is generally towards the southern direction (see Fig. 7.2.1). With the radial motion of M81 towards the Milky Way reported as 73±6 km s^{-1} (de Vaucouleurs et al., 1991), we derive the total space velocity of M 81 relative to the MW as 471±108 km s^{-1}.

7.2. Proper motion of M 82

The water masers in M 82 were observed in four epochs spanning over eight years at 22.2 GHz. From these observations, we detected several water maser spots in the velocity range of 100 to 362 km s^{-1}. However, only three water components were followed successfully over the four epochs of observation. These H_2O masers are located at the opposite sides of the galaxy dynamic center, at a projected distance of ∼160 pc (9.4″) and ∼240 pc (13.6″) for south-western and north-eastern positions, respectively. We obtained the position offsets of the maser spots relative to M 81*, and then fitted a rectilinear motion to the derived positions to obtain the proper motion of the maser sources. Correcting for the internal rotation motion of M 82 using the values derived from the south-western maser components of 6.4±1.5 μas yr^{-1} and −3.5±0.8 μas yr^{-1} in right ascension and declination, and north-eastern maser components of −6.7±1.5 μas yr^{-1} and 3.4±0.8 μas yr^{-1} in right ascension and declination, respectively, we obtained a proper motion of $\dot{\alpha}_{\rm M82} = 8.3 \pm 5.5\,\mu{\rm as\,yr^{-1}}(\sim 143 \pm 95\,{\rm km\,s^{-1}})$ and $\dot{\delta}_{\rm M82} = 10.6 \pm 4.3\,\mu{\rm as\,yr^{-1}}$ $(\sim 182 \pm 74\,{\rm km\,s^{-1}})$.

From these results, the proper motion of M 82 relative to M 81 is generally towards the north-eastern direction (see Fig. 7.2.1). With a derived radial motion of M 82 towards M81 being 237±6 km s^{-1}, we obtain its total space velocity relative to M 81 galaxy as $331 \pm 120\,{\rm km\,s^{-1}}$.

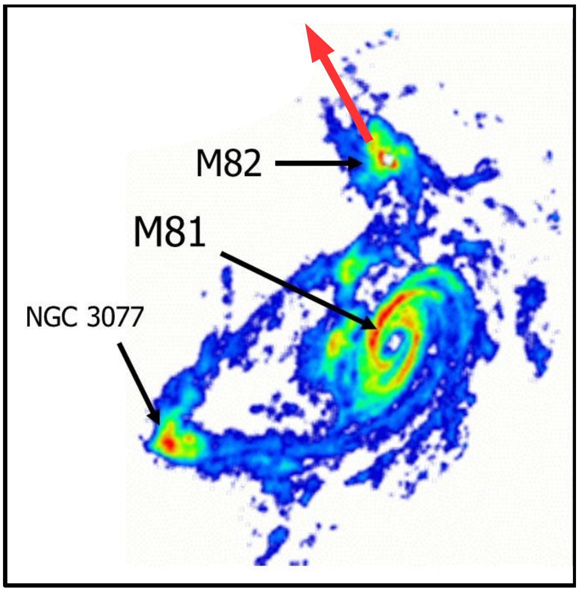

(a) The illustration shows the proper motion of M 82 relative to M 81 galaxy. M 82 motion is 143±95 km s^{-1} towards the east and 182±74 km s^{-1} towards the north.

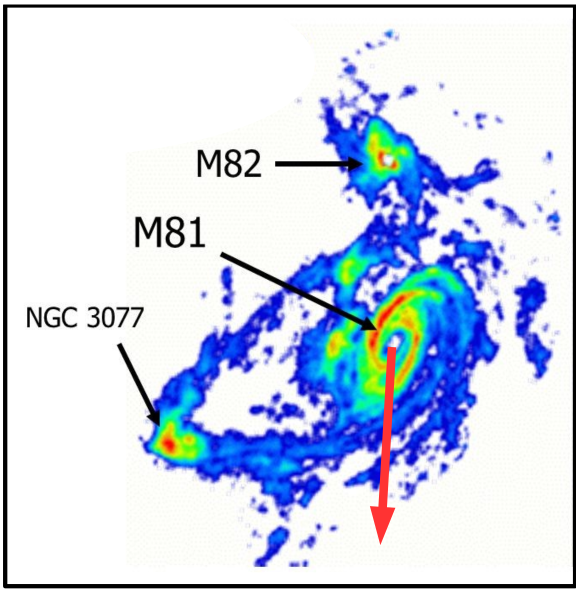

(b) The illustration shows the proper motion of M 81 relative to the Milky Way. M 81 motion is 179±100 km s^{-1} towards the east and −429±39 km s^{-1} towards the north.

Figure 7.2.1.: The images show M 81 group 21 cm HI line emission overlaid with arrows that indicate the proper motions of M 81 and M 82. The arrows are not vectors, they indicate the general direction of the galaxy motion.

7.3. Lower mass estimate of M 81

There have been attempts to derive the mass of galaxies in M 81 group. The challenge persist because only the radial velocities of galaxies in the group are known. To circumvent this challenge, different techniques have been devised where only line-of-sight velocities are required. However, these techniques are based on some serious assumptions, which include orbital eccentricities, accurate projected separation relative to main galaxy, and small velocity dispersions. Given the uncertainties introduced by these assumptions, it is evident that the most reliable way of deriving masses is by using orbits, which require the knowledge of three-dimensional velocity vectors, obtained from proper motion measurements.

Having estimated the proper motions and derived the space motions of M 81 and M 82, we can estimate the lower mass limit of M 81. At a distance of 38 kpc (~37 arcmin) from M 81 center, M 82 is deeply embedded in the M 81's dark matter halo, which extends to ~140 kpc. If we consider M 82 as bound to M 81's gravitational potential, its velocity must be smaller than the escape velocity, thus we can deduce the orbital lower limit on the mass of M 81 to be $(4.8 \pm 0.6) \times 10^{11}\,\mathrm{M}_\odot$.

7.4. Supernova SN 2008iz

The second part of this work involved the study of supernova SN 2008iz, which was discovered by chance in the course of proper motion observations. We have presented multi-epoch multi-frequency VLA and VLBI radio results from its monitoring campaign. We fitted two models to the data, a simple time power-law ($S \propto t^{\beta}$) and a simplified Weiler model, yielding decline indices, β, of -1.22 ± 0.07 (days 100-1500) and -1.41 ± 0.02 (days 76-2167), respectively. The late time radio light curve evolution shows flux-density flares at ~970 and ~1400 days which are a factor of ~2 and ~4 higher than the expected flux, respectively. The later flare, besides being brighter, does not show signs of decline, at least from the results examined so far (2014 January 23; day 2167). The flaring activity is attributed to increase in the number density of shocked circumstellar medium (CSM) electrons as the expanding shock wave encounters a clumpy denser medium. The late flare may also be attributed to the transition of the front shock from the CSM bubble into the interstellar medium (ISM), although a very dense ISM ($>10^4\,\mathrm{cm}^{-3}$) would be required, which is consistent with SN 2008iz being deeply buried within the center of M 82.

The 1.4 GHz flux density values fall below the supernova model fit (see Fig. 6.3.4), a phenomena confirmed by 3σ LOFAR non-detection limit at 154 MHz level of 0.41 mJy/beam. The low flux values could be attributed to free-free absorption (FFA) from a dense foreground screen along the line of sight or a low-frequency cut-off caused by Razin-Tsytovich effect.

The spectrum for SN 2008iz for the period from ∼430 to 2167 days after the supernova explosion shows no signs of evolution and remains steep ($\alpha \sim -1$). This is different from the well-studied SN 1993J, whose spectral index evolution shows α flattening of the spectrum at all frequencies, beginning at an age ∼970 days.

From the 4.8 and 8.4 GHz VLBI images, the supernova expansion is seen to start with a shell-like structure, reflecting an expansion with similar velocities into all direction that gets more and more asymmetric at later stages. Finally, in later epochs the structure breaks up, with bright structures dominating the lower part of the ring, which serves as an indication of a denser surrounding medium along the southern direction. This structural evolution differs significantly from SN 1993J, which remains circularly symmetric over 4000 days after the explosion. From the size evolution of the SN 2008iz derived from the 4.8 and 8.4 GHz VLBI images, a deceleration parameter, m, of 0.86 ± 0.02 and an expansion velocity of $(12.1 \pm 0.2) \times 10^3\,\mathrm{km\,s^{-1}}$ are derived for the time range between 73 and 1400 days.

From the energy equipartition between fields and particles, we estimate the minimum total energy in relativistic particles and the magnetic fields during the supernova expansion. On 2009 April 8, $E_{min} \propto 3.15 \times 10^{46} - 1.63 \times 10^{48}$ erg, which corresponds to an average equipartition magnetic field of $B_{min} \propto 37 - 266$ mG. We derive the average magnetic field in the circumstellar wind of $B_{csm} = 0.67$ mG at a radius from the center of the supernova explosion of $\sim 7.2 \times 10^{16}$ cm. Since the supernova shock compression could only enhance the magnetic field by a factor of 4, powerful amplification mechanisms must be at play in SN 2008iz to account for the derived magnetic field amplification of 55 – 400 that is responsible for the synchrotron radio emission.

A. Appendix

Summary of the VLBA results

Table A.1.: A summary for the continuum sources VLBA 22.2 GHz results

Year	Name	Peak Flux [mJy/b]	$\triangle\alpha$ [mas]	$\triangle\delta$ [mas]	Beam Size [mas]	PA [°]
2007	M81	83.8±0.64	0.005±0.002	0.006±0.002	0.36×0.27	52
	0945+6924	8.7±0.36	0.972±0.011	-0.154±0.013	0.58×0.40	166
	0948+6848_core	11.4±0.41	-1.031±0.004	-6.227±0.005	0.51×0.41	11
	0948+6848_jet	3.4±0.25	0.723±0.016	0.481±0.019	1.09×0.79	26
	1004+6936	22.9±0.62	-1.455±0.005	0.544±0.007	0.59×0.38	7
2008	M81	84.1±0.22	0.003±0.003	0.002±0.003	0.72×0.66	56
	0945+6924	4.8±0.01	0.975±0.006	-0.130±0.007	0.86×0.49	144
	0948+6848_core	21.7±0.19	-1.061±0.004	-6.206±0.004	0.80×0.72	147
	0948+6848_jet	2.4±0.12	0.691±0.080	0.490±0.053	1.88×1.17	76
	1004+6936	12.4±0.12	-1.407±0.003	0.573±0.004	0.97×0.69	27
2009	M81	86.0±0.33	0.002±0.001	0.002±0.001	0.57×0.49	51
	0945+6924	4.6±0.15	0.952±0.007	-0.145±0.009	0.92×0.56	151
	0948+6848_core	27.4±0.14	-1.043±0.007	-6.175±0.010	0.71×0.46	169
	0948+6848_jet	4.1±0.14	0.681±0.033	0.589±0.053	1.03×0.61	155
	1004+6936	14.7±0.22	-1.430±0.003	0.586±0.005	0.75×0.53	171
2015_1	M81	75.3±0.12	0.005±0.001	0.001±0.001	0.60×0.47	53
	0945+6924	3.2±0.10	0.935±0.007	0.045±0.004	0.91×0.73	167
	0948+6848_core	1.4±0.10	-0.926±0.033	-5.934±0.042	0.88×0.59	6
	0948+6848_jet	4.3±0.10	0.800±0.025	1.120±0.033	0.92×0.62	3
	1004+6936	20.0±0.18	-1.398±0.003	0.759±0.015	0.73×0.40	153
2015_2	M81	75.2±0.12	0.004±0.003	0.003±0.002	0.57×0.47	49
	0945+6924	3.2±0.11	0.954±0.011	0.065±0.012	0.76×0.56	164
	0948+6848_core	1.5±0.11	-0.930±0.011	-5.918±0.010	0.92×0.62	8
	0948+6848_jet	4.3±0.11	0.804±0.025	1.119±0.034	0.89×0.62	4
	1004+6936	20.1±0.19	-1.406±0.015	0.728±0.008	0.74×0.52	153

Table A.2.: A summary for the continuum sources VLBA 15.3 GHz results

Year	Name	Peak Flux [mJy/b]	$\triangle\alpha$ [mas]	$\triangle\delta$ [mas]	Beam Size [mas]	PA [°]
2007	M81	82.3±0.13	0.011±0.002	0.007±0.001	1.19×0.58	42
	0945+6924	11.4±0.15	0.858±0.006	-0.177±0.009	1.28×0.47	36
	0948+6848_core	7.3±0.15	-1.064±0.010	-6.236±0.014	1.22×0.48	37
	0948+6848_jet	5.8±0.08	0.650±0.006	0.186±0.008	1.58×0.75	31
	1004+6936	22.2±0.12	-1.452±0.002	0.523±0.002	1.21×0.51	36
2008	M81	86.8±0.43	0.002±0.002	0.003±0.002	0.54×0.36	60
	0945+6924	4.4±0.20	0.864±0.012	-0.171±0.008	0.64×0.44	89
	0948+6848_core	16.8±0.23	-1.071±0.004	-6.181±0.002	0.58×0.40	81
	0948+6848_jet	11.3±0.12	0.645±0.010	0.385±0.013	1.35×1.08	167
	1004+6936	13.6±0.23	-1.454±0.004	0.591±0.004	0.56×0.44	121
2009	M81	113.9±0.23	0.003±0.002	0.002±0.001	0.53×0.44	51
	0945+6924	6.7±0.21	0.845±0.008	-0.135±0.009	0.81×0.67	177
	0948+6848_core	32.1±0.33	-1.064±0.003	-6.146±0.004	0.77×0.62	18
	0948+6848_jet	6.2±0.20	0.647±0.013	0.502±0.017	1.11×0.83	17
	1004+6936	22.7±0.20	-1.442±0.003	0.566±0.003	0.78×0.63	14

Table A.3.: A summary for the continuum sources VLBA 8.4 GHz results

Year	Name	Peak Flux [mJy/b]	$\triangle\alpha$ [mas]	$\triangle\delta$ [mas]	Beam Size [mas]	PA [°]
2007	M81	81.1±0.24	0.009±0.002	0.011±0.002	0.74×0.66	34
	0945+6924	10.8±0.12	0.769±0.006	-0.207±0.008	0.74×0.51	145
	0948+6848_core	5.7±0.07	-1.092±0.003	-6.219±0.004	0.71×0.51	145
	0948+6848_jet	8.4±0.05	0.637±0.002	0.249±0.003	1.16×0.85	10
	1004+6936	20.2±0.10	-1.514±0.001	0.404±0.002	0.77×0.51	153
2008	M81	80.5±0.54	0.022±0.003	0.011±0.002	0.99×0.50	63
	0945+6924	5.4±0.22	0.748±0.013	-0.194±0.012	0.89×0.83	170
	0948+6848_core	10.2±0.16	-1.064±0.007	-6.212±0.004	0.78×0.60	74
	0948+6848_jet	16.5±0.09	0.614±0.006	0.224±0.007	1.32×1.06	12
	1004+6936	11.9±0.28	-1.529±0.011	0.432±0.016	0.82×0.66	153
2009	M81	99.3±0.28	0.016±0.002	0.007±0.002	0.78×0.65	50
	0945+6924	6.2±0.10	0.743±0.005	-0.176±0.005	0.86×0.84	107
	0948+6848_core	21.8±0.14	-1.079±0.002	-6.156±0.002	0.80×0.76	10
	0948+6848_jet	17.4±0.12	0.571±0.003	0.322±0.004	1.33×0.94	19
	1004+6936	22.5±0.16	-1.493±0.005	0.434±0.006	0.84×0.80	131

Supernova SN 2008iz spectral indices

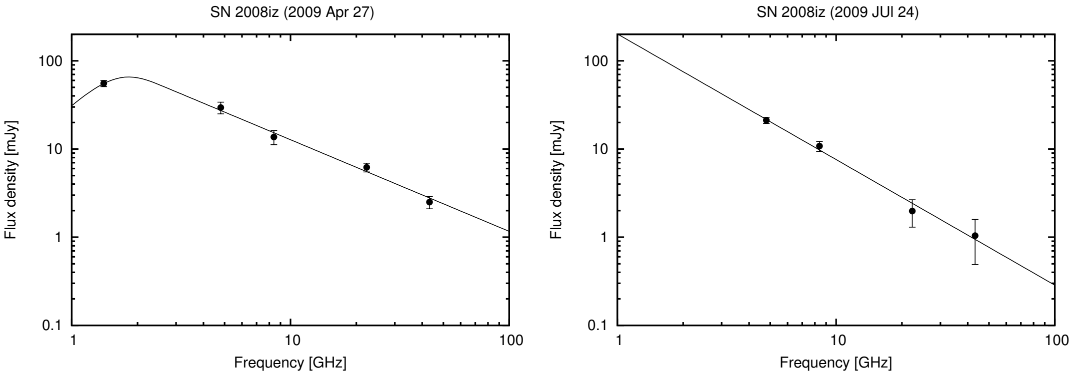

(a) The 2009 Apr. 27 observations (b) The 2009 July 24 observations

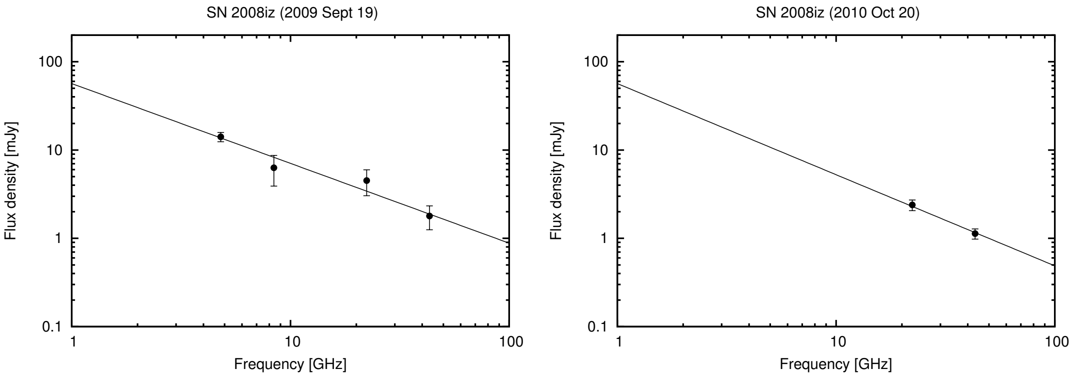

(c) The 2009 Sept. 19 observations (d) The 2010 Oct. 20 observations

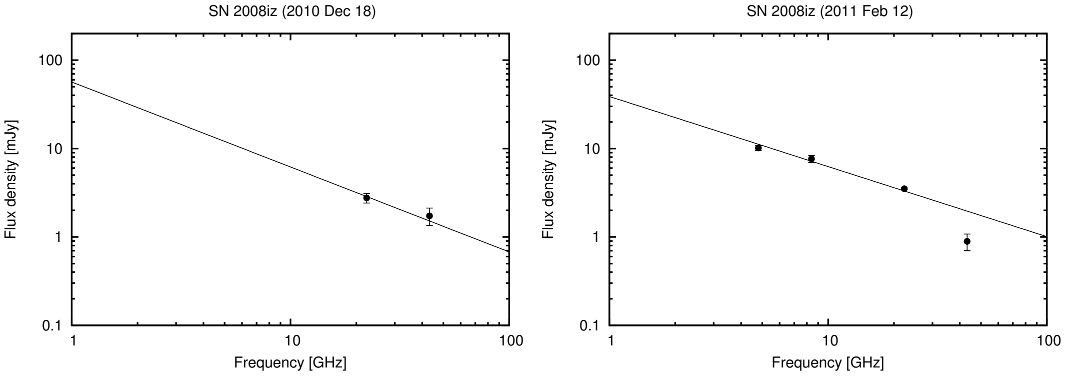

(e) The 2010 Dec. 18 observations (f) The 2011 Feb. 12 observations

Figure A.0.1.: Contd next page

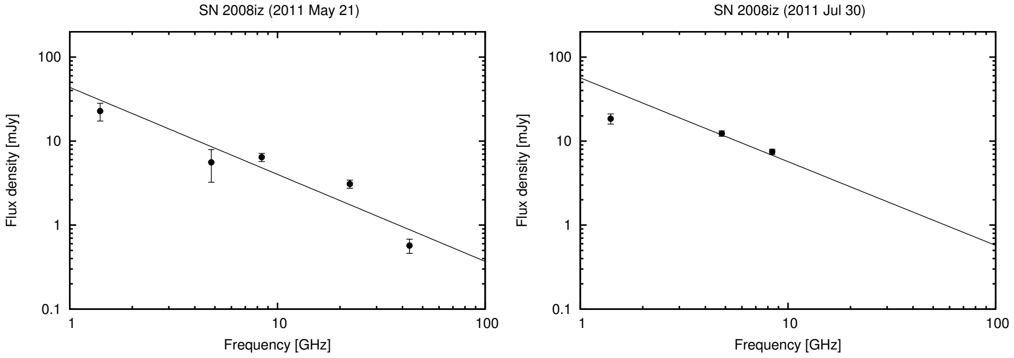

(g) The 2011 May 21 observations

(h) The 2011 July 30 observations

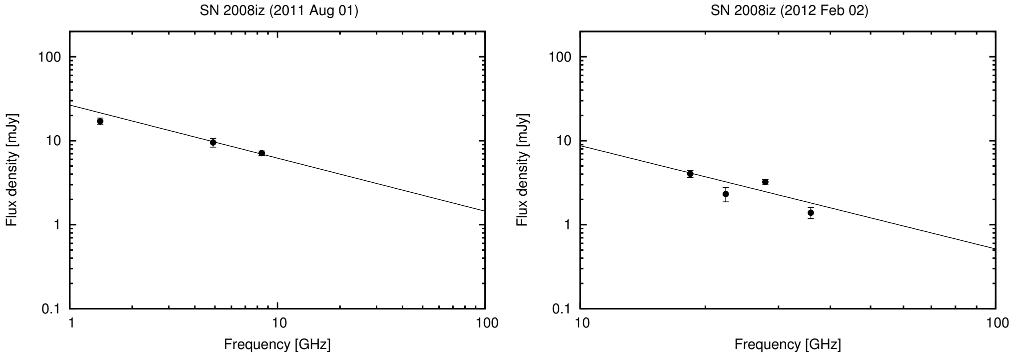

(i) The 2011 Aug. 01 observations

(j) The 2012 Feb. 02 observations

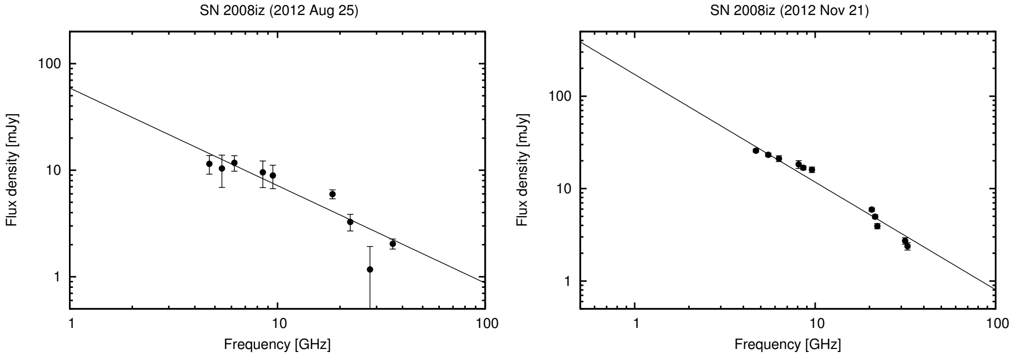

(k) The 2012 Aug. 25 observations

(l) The 2012 Nov. 21 observations

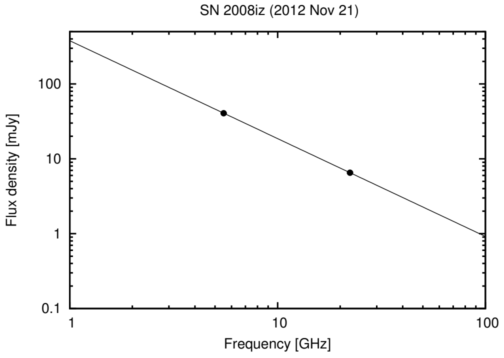

(m) The 2012 Nov. 21 observations

Figure A.0.1.: The SN 2008iz spectral index fits at different supernova evolution time.

B. Appendix

Acronyms & Abbreviations

AGN	....	Active Galactic Nucleus
ALMA	....	Atacama Large Millimeter/submillimeter Array
AU	....	Astronomical Unit (1 AU = 1.496×10^{11} m)
BeSSel	....	Bar and Spiral Structure Legacy Survey
CO	....	Carbon Monoxide
COSMOS	....	Cosmic Evolution Survey
FFA	....	Free-Free Absorption
FIRST	....	Faint Images of the Radio Sky at Twenty-cm
GOODS	....	Great Observatories Origins Deep Survey
ISM	....	Interstellar Stellar Medium
JVLA	....	Jansky Very Large Array
LOFAR	....	Low-Frequency Array for Radio astronomy
Ly_α	....	Lyman-alpha emission line
LSR	....	Local Standard of Rest
MERLIN	....	Multi-Element Radio Linked Interferometer Network
$\mathrm{M}_\odot$	....	Solar Mass (1 $\mathrm{M}_\odot$ = 1.98892×10^{30} kg)
M 81	....	Messier catalog source 81
M 81*	....	M81 radio core
M 82	....	Messier catalog source 82
Mg II	....	Magnesium II line
NRAO	....	National Radio Astronomy Observatory
NaI	....	Sodium Iodide line
pc	....	parsec (1 pc = 3.086×10^{16} m)
SKA	....	Square Kilometer Array
Sgr A*	....	Sagittarius A*
SMBH	....	Super Massive Black Hole
SSA	....	Synchrotron Self Absorption
VVDS	....	VIMOS-VLT Deep Survey
VLA	....	Very Large Array
VLBA	....	Very Long Baseline Array
VLBI	....	Very Long Baseline Interferometry
β	....	Power-law decline
μas	....	Micro arc-seconds

Acknowledgements

There comes a point in life when one realizes how quickly time goes by, and how quickly it has gone. Then it really speeds up exponentially. Well, the exponential part is here for me. It's been quite a ride. And a fun ride too! This thesis attests to the fact. Of course, I would not have come to this point if it was not for the constant support and help of quite a number of people. The first one on the list is you, Andreas. You have the intelligence and mastery, yet are warm and approachable - I must admit I felt so insignificant at times when I listened to you. But you always gave me the room, time, and freedom that I needed, while still softly pushing me in the right direction. I especially value your constant availability, with an open office door. You never checked on your watch whenever I popped in your office. It has been a pleasure having you as my advisor!

I would like to thank my thesis committee members, Professor Dr. Karl M. Menten, Professor Dr. Pavel Kroupa, Dr. Andreas Brunthaler and Dr. Christian Henkel. You all continually and convincingly conveyed a spirit of adventure in regard to research during your guidance. I cherished this meetings, because I never felt "stupid" even when wrong.

The members of the mm and sub-mm department have contributed immensely to my personal and professional time at MPIfR. The group has been a source of friendships as well as good advice and collaboration. Especially Dr. Bo Zhang and Dr Rosie Chen with whom I shared the office, thank you so much for always having a moment to chat. I may not remember everything we talked about but I remember what it made me feel. Dr. Hans-Rainer besides your well written and helpful on-line AIPS tutorial guide, you were always available whenever I was in need of your help.

As the norm for every Ph.D. student, one needs to find a way to stay sane, to take your mind off the work. For me this was easy because I have you, Veronica and little Ian. Thank you Veronica for never failing to ask how the day was and constantly showing interest in AIPS, proper motion and visibilities – I bet all this meant nothing to you, but you showed some interest anyway. I thank you both for all the love and encouragement. You kept refreshing my batteries and put things back into perspective.

To my dear parents, I thank you for always believing in me and supporting whatever I decided I would like to do. Your words of advice and encouragement have been renewed constantly in my mind, giving me the confidence and strength to keep the pursuit.

I can't end the list without expressing my gratitude and deepest appreciation to Karl, for accepting me as a Ph.D student. You believed in me and gave me a chance together with my family. To Hashim Nadir, you are my great inspiration and a mentor. Petri Vaisanen and Kartik Sheth, I can't thank you enough.

Lastly, I praise God, the almighty for providing me this opportunity and granting me the capability to proceed successfully.

Bibliography

Alberdi, A. and Marcaide, J. M. (2005). Imaging of SN 1993J. In *IAU Colloq. 192: Cosmic Explosions, On the 10th Anniversary of SN1993J*, page 13.

Appleton, P. N., Davies, R. D., and Stephenson, R. J. (1981). *MNRAS*, 195:327–352.

Asaki, Y., Sudou, H., Kono, Y., Doi, A., Dodson, R., Pradel, N., Murata, Y., Mochizuki, N., Edwards, P. G., Sasao, T., and Fomalont, E. B. (2007). *PASJ*, 59:397–418.

Backer, D. C. (1994). Sgr A* - Miniature, Quiescent AGN? page 149.

Batejat, F., Conway, J. E., Hurley, R., Parra, R., Diamond, P. J., Lonsdale, C. J., and Lonsdale, C. J. (2011). *ApJ*, 740:95.

Baudry, A. and Brouillet, N. (1996). *A&A*, 316:188–195.

Baudry, A., Brouillet, N., and Henkel, C. (1994). *A&A*, 287:20–31.

Beasley, A. J. and Conway, J. E. (1995). VLBI Phase-Referencing. volume 82 of *Astronomical Society of the Pacific Conference Series*, page 327.

Beswick, R. J., Muxlow, T. W. B., Pedlar, A., Fenech, D., Fender, R., and Maccarone, T. (2009). *The Astronomer's Telegram*, 2060:1.

Beswick, R. J., Riley, J. D., Marti-Vidal, I., Pedlar, A., Muxlow, T. W. B., McDonald, A. R., Wills, K. A., Fenech, D., and Argo, M. K. (2006). *MNRAS*, 369:1221–1228.

Bietenholz, M. F., Bartel, N., and Rupen, M. P. (2000). *ApJ*, 532:895–908.

Bietenholz, M. F., Bartel, N., and Rupen, M. P. (2004). *ApJ*, 615:173–180.

Bietenholz, M. F., Bartel, N., Rupen, M. P., Conway, J. E., Beasley, A. J., Sramek, R. A., Romney, J. D., Titus, M. A., Graham, D. A., Altunin, V. I., Jones, D. L., Rius, A., Venturi, T., Umana, G., Weiler, K. W., van Dyk, S. D., Panagia, N., Cannon, W. H., Popelar, J., and Davis, R. J. (1996). *ApJ*, 457:604.

Bower, G. A., Wilson, A. S., Heckman, T. M., and Richstone, D. O. (1996). *AJ*, 111:1901.

Bower, G. C., Falcke, H., Sault, R. J., and Backer, D. C. (2002). *ApJ*, 571:843–855.

Brunthaler, A. (2004). *Proper Motions in the local Group*. PhD thesis, Max-Planck Institute for Radioastronomy.

Brunthaler, A., Bower, G. C., and Falcke, H. (2006). *A&A*, 451:845–850.

Brunthaler, A., Martí-Vidal, I., Menten, K. M., Reid, M. J., Henkel, C., Bower, G. C., Falcke, H., Feng, H., Kaaret, P., Butler, N. R., Morgan, A. N., and Weiß, A. (2010). *A&A*, 516:A27.

Brunthaler, A., Menten, K. M., Reid, M. J., Henkel, C., Bower, G. C., and Falcke, H. (2009a). *The Astronomer's Telegram*, 2020:1.

Brunthaler, A., Menten, K. M., Reid, M. J., Henkel, C., Bower, G. C., and Falcke, H. (2009b). *A&A*, 499:L17–L20.

Brunthaler, A., Reid, M. J., and Falcke, H. (2005a). Atmosphere-Corrected Phase-Referencing. volume 340 of *Astronomical Society of the Pacific Conference Series*, page 455.

Brunthaler, A., Reid, M. J., Falcke, H., Greenhill, L. J., and Henkel, C. (2005b). *Science*, 307:1440–1443.

Brunthaler, A., Reid, M. J., Falcke, H., Henkel, C., and Menten, K. M. (2007). *A&A*, 462:101–106.

Chatterjee, S., Cordes, J. M., Vlemmings, W. H. T., Arzoumanian, Z., Goss, W. M., and Lazio, T. J. W. (2004). *ApJ*, 604:339–345.

Chevalier, R. and Blondin, J. M. (1995). *ApJ*, 444:312–317.

Chevalier, R. A. (1982). *ApJ*, 258:790–797.

Churchwell, E., Witzel, A., Huchtmeier, W., Pauliny-Toth, I., Roland, J., and Sieber, W. (1977). *A&A*, 54:969–971.

Dalcanton, J. J., Williams, B. F., Seth, A. C., Dolphin, A., Holtzman, J., Rosema, K., Skillman, E. D., Cole, A., Girardi, L., Gogarten, S. M., Karachentsev, I. D., Olsen, K., Weisz, D., Christensen, C., Freeman, K., Gilbert, K., Gallart, C., Harris, J., Hodge, P., de Jong, R. S., Karachentseva, V., Mateo, M., Stetson, P. B., Tavarez, M., Zaritsky, D., Governato, F., and Quinn, T. (2009). *ApJS*, 183:67–108.

de Cea del Pozo, E., Torres, D. F., and Rodriguez Marrero, A. Y. (2009). *ApJ*, 698:1054–1060.

de Mello, D. F., Smith, L. J., Sabbi, E., Gallagher, J. S., Mountain, M., and Harbeck, D. R. (2008). *AJ*, 135:548–554.

de Vaucouleurs, G., de Vaucouleurs, A., Corwin, Jr., H. G., Buta, R. J., Paturel, G., and Fouqué, P. (1991). *Third Reference Catalogue of Bright Galaxies.*

Dehnen, W. and Binney, J. J. (1998). *MNRAS*, 298:387–394.

Devereux, N., Ford, H., Tsvetanov, Z., and Jacoby, G. (2003). *AJ*, 125:1226–1235.

Dinescu, D. I., Girard, T. M., van Altena, W. F., and López, C. E. (2005a). *ApJL*, 618:L25–L28.

Dinescu, D. I., Keeney, B. A., Majewski, S. R., and Girard, T. M. (2004). *AJ*, 128:687–699.

Dinescu, D. I., Martínez-Delgado, D., Girard, T. M., Peñarrubia, J., Rix, H.-W., Butler, D., and van Altena, W. F. (2005b). *ApJL*, 631:L49–L52.

Dyson, J. and Williams, D. (1980). *Physics of the Interstellar Medium.* Manchester University Press.

Elvis, M. and van Speybroeck, L. (1982). *ApJL*, 257:L51–L55.

Fenech, D. M., Muxlow, T. W. B., Beswick, R. J., Pedlar, A., and Argo, M. K. (2008). *MNRAS*, 391:1384–1402.

Fomalont, E. B. (1999). Image Analysis. volume 180 of *Astronomical Society of the Pacific Conference Series*, page 301.

Fomalont, E. B. and Perley, R. A. (1999). Calibration and Editing. volume 180 of *Astronomical Society of the Pacific Conference Series*, page 79.

Fransson, C. and Björnsson, C.-I. (1998). *ApJ*, 509:861–878.

Freedman, W. L. (2000). *PhysRep*, 333:13–31.

Freedman, W. L., Hughes, S. M., Madore, B. F., Mould, J. R., Lee, M. G., Stetson, P., Kennicutt, R. C., Turner, A., Ferrarese, L., Ford, H., Graham, J. A., Hill, R., Hoessel, J. G., Huchra, J., and Illingworth, G. D. (1994). *ApJ*, 427:628–655.

Gaffney, N. I., Lester, D. F., and Telesco, C. M. (1993). *ApJ*, 407:L57–L60.

Goetz, M., Downes, D., Greve, A., and McKeith, C. D. (1990). *A&A*, 240:52–69.

Gomez, J. C., Athanassoula, L., Fuentes, O., and Bosma, A. (2004). Determination of Initial Conditions of M81 Triplet Using Evolution Strategies. volume 314 of *Astronomical Society of the Pacific Conference Series*, page 629.

Greenhill, L. J., Moran, J. M., Reid, M. J., Menten, K. M., and Hirabayashi, H. (1993). *ApJ*, 406:482–488.

Güver, T. and Özel, F. (2009). The relation between optical extinction and hydrogen column density in the Galaxy. *MNRAS*, 400:2050–2053.

Hagiwara, Y. (2007). *AJ*, 133:1176–1186.

Henkel, C., Guesten, R., Downes, D., Thum, C., Wilson, T. L., and Biermann, P. (1984). *A&A*, 141:L1–L3.

Henkel, C., Peck, A. B., Tarchi, A., Nagar, N. M., Braatz, J. A., Castangia, P., and Moscadelli, L. (2005). *A&A*, 436:75–90.

Herrnstein, J., Moran, J., Greenhill, L., Inoue, M., Nakai, N., Miyoshi, M., and Diamond, P. (1997). A 4% Geometric Distance to NGC 4258 from Proper Motions in the Nuclear Water Maser. volume 29 of *Bulletin of the American Astronomical Society*, page 1252.

Ho, L. C., Filippenko, A. V., and Sargent, W. L. W. (1996). *ApJ*, 462:183.

Ho, L. C., van Dyk, S. D., Pooley, G. G., Sramek, R. A., and Weiler, K. W. (1999a). *AJ*, 118:843–852.

Ho, L. C., van Dyk, S. D., Pooley, G. G., Sramek, R. A., and Weiler, K. W. (1999b). Discovery of Radio Outbursts in the Active Nucleus of M81. *AJ*, 118:843–852.

Högbom, J. A. (1974). *A&AS*, 15:417.

Hubble, E. P. (1926). *ApJ*, 63:236–274.

Ishisaki, Y., Makishima, K., Iyomoto, N., Hayashida, K., Inoue, H., Mitsuda, K., Tanaka, Y., Uno, S., Kohmura, Y., Mushotzky, R. F., Petre, R., Serlemitsos, P. J., and Terashima, Y. (1996). *PASJ*, 48:237–248.

Jackson, N., Battye, R. A., Browne, I. W. A., Joshi, S., Muxlow, T. W. B., and Wilkinson, P. N. (2007). *MNRAS*, 376:371–377.

Johnson, D. R. H. and Soderblom, D. R. (1987). *AJ*, 93:864–867.

Jones, B. F., Klemola, A. R., and Lin, D. N. C. (1994). *AJ*, 107:1333–1337.

Jones, T. W. and Odell, S. L. (1977). *A&A*, 61:291–293.

Kallivayalil, N., van der Marel, R. P., Alcock, C., Axelrod, T., Cook, K. H., Drake, A. J., and Geha, M. (2006). *ApJ*, 638:772–785.

Karachentsev, I. D. and Kashibadze, O. G. (2006). *Astrophysics*, 49:3–18.

King, A. L., Miller, J. M., Bietenholz, M., Gültekin, K., Reynolds, M. T., Mioduszewski, A., Rupen, M., and Bartel, N. (2016). Discrete knot ejection from the jet in a nearby low-luminosity active galactic nucleus, M81*. *Nature Physics*, 1.

Kirsten, F. (2014). *Pulsar astrometry with VLBI and beyond*. PhD thesis, Argelander-Institute for Astronomy.

Kronberg, P. P., Sramek, R. A., Birk, G. T., Dufton, Q. W., Clarke, T. E., and Allen, M. L. (2000). *ApJ*, 535:706–711.

Kulessa, A. S. and Lynden-Bell, D. (1992). *MNRAS*, 255:105–118.

Legg, M. P. C. and Westfold, K. C. (1968). *ApJ*, 154:499.

Liu, J.-C., Zhu, Z., and Hu, B. (2011). *A&A*, 536:A102.

Lynds, C. R. and Sandage, A. R. (1963). *ApJ*, 137:1005.

Macquart, J.-P. and Melrose, D. B. (2000). *Phys. Rev.*, 62:4177.

Marcaide, J. M., Alberdi, A., Bartel, N., Clark, T. A., Corey, B. E., Elosegui, P., Gorenstein, M. V., Guirado, J. C., Kardashev, N., Popov, M., Preston, R., Ratner, M. I., Rioja, M. J., Rogers, A. E. E., and Shapiro, I. I. (1992). *A&A*, 258:295–301.

Marchili, N., Martí-Vidal, I., Brunthaler, A., Krichbaum, T. P., Müller, P., Liu, X., Song, H.-G., Bach, U., Beswick, R., and Zensus, J. A. (2010). *A&A*, 509:A47.

Markoff, S., Nowak, M., Young, A., Marshall, H. L., Canizares, C. R., Peck, A., Krips, M., Petitpas, G., Schödel, R., Bower, G. C., Chandra, P., Ray, A., Muno, M., Gallagher, S., Hornstein, S., and Cheung, C. C. (2008). *ApJ*, 681:905–924.

Martí-Vidal, I., Marcaide, J. M., Alberdi, A., Guirado, J. C., Lara, L., Pérez-Torres, M. A., Ros, E., Argo, M. K., Beswick, R. J., Muxlow, T. W. B., Pedlar, A., Shapiro, I. I., Stockdale, C. J., Sramek, R. A., Weiler, K. W., and Vinko, J. (2007). *A&A*, 470:1071–1077.

Martí-Vidal, I., Marcaide, J. M., Alberdi, A., Guirado, J. C., Pérez-Torres, M. A., and Ros, E. (2011a). *A&A*, 526:A142.

Martí-Vidal, I., Marcaide, J. M., Alberdi, A., Guirado, J. C., Pérez-Torres, M. A., and Ros, E. (2011b). *A&A*, 526:A143.

Martí-Vidal, I., Marcaide, J. M., Alberdi, A., Pérez-Torres, M. A., Ros, E., and Guirado, J. C. (2011c). *A&A*, 533:A111.

Matsushita, S., Kawabe, R., Kohno, K., Matsumoto, H., Tsuru, T. G., and Vila-Vilaró, B. (2005). *ApJ*, 618:712–722.

Mattila, S., Fraser, M., Smartt, S. J., Meikle, W. P. S., Romero-Cañizales, C., Crockett, R. M., and Stephens, A. (2013). *MNRAS*, 431:2050–2062.

Mayya, Y. D. and Carrasco, L. (2009). M82 as a Galaxy: Morphology and Stellar Content of the Disk and Halo. volume 37 of *Revista Mexicana de Astronomia y Astrofisica, vol. 27*, pages 44–55.

Mayya, Y. D., Carrasco, L., and Luna, A. (2005). *ApJL*, 628:L33–L36.

Mould, J. R., Huchra, J. P., Freedman, W. L., Kennicutt, Jr., R. C., Ferrarese, L., Ford, H. C., Gibson, B. K., Graham, J. A., Hughes, S. M. G., Illingworth, G. D., Kelson, D. D., Macri, L. M., Madore, B. F., Sakai, S., Sebo, K. M., Silbermann, N. A., and Stetson, P. B. (2000). *APJ*, 529:786–794.

Muxlow, T. W. B., Beswick, R. J., Pedlar, A., Fenech, D., Argo, M. K., Ward, M. J., and Zezas, A. (2009). *The Astronomer's Telegram*, 2073:1.

Muxlow, T. W. B., Pedlar, A., Wilkinson, P. N., Axon, D. J., Sanders, E. M., and de Bruyn, A. G. (1994). *MNRAS*, 266:455.

Niell, A. E. (1996). *J. Geophys. Res.*, 101:3227–3246.

Pacholczyk, A. G. (1970). *Radio astrophysics. Nonthermal processes in galactic and extragalactic sources*. harvard.

Pacholczyk, A. G. (1977). *Oxford Pergamon Press International Series on Natural Philosophy*, 89.

Pedreros, M. H., Costa, E., and Méndez, R. A. (2006). *AJ*, 131:1461–1470.

Peimbert, M. and Torres-Peimbert, S. (1981). *ApJ*, 245:845–856.

Pérez-Torres, M. A., Alberdi, A., and Marcaide, J. M. (2001). *A&A*, 374:997–1002.

Pérez-Torres, M. A., Alberdi, A., Marcaide, J. M., Guerrero, M. A., Lundqvist, P., Shapiro, I. I., Ros, E., Lara, L., Guirado, J. C., Weiler, K. W., and Stockdale, C. J. (2005). *MNRAS*, 360:1055–1062.

Pérez-Torres, M. A., Alberdi, A., Marcaide, J. M., Guirado, J. C., Lara, L., Mantovani, F., Ros, E., and Weiler, K. W. (2002). *MNRAS*, 335:L23–L28.

Pérez-Torres, M. A., Lundqvist, P., Beswick, R. J., Björnsson, C. I., Muxlow, T. W. B., Paragi, Z., Ryder, S., Alberdi, A., Fransson, C., Marcaide, J. M., Martí-Vidal, I., Ros, E., Argo, M. K., and Guirado, J. C. (2014). *ApJ*, 792:38.

Piatek, S., Pryor, C., Bristow, P., Olszewski, E. W., Harris, H. C., Mateo, M., Minniti, D., and Tinney, C. G. (2005). *AJ*, 130:95–115.

Piatek, S., Pryor, C., Bristow, P., Olszewski, E. W., Harris, H. C., Mateo, M., Minniti, D., and Tinney, C. G. (2006). *AJ*, 131:1445–1460.

Piatek, S., Pryor, C., Olszewski, E. W., Harris, H. C., Mateo, M., Minniti, D., Monet, D. G., Morrison, H., and Tinney, C. G. (2002). *AJ*, 124:3198–3221.

Piatek, S., Pryor, C., Olszewski, E. W., Harris, H. C., Mateo, M., Minniti, D., and Tinney, C. G. (2003). *AJ*, 126:2346–2361.

Pietrzyński, G., Graczyk, D., Gieren, W., Thompson, I. B., Pilecki, B., Udalski, A., Soszyński, I., Kozłowski, S., Konorski, P., Suchomska, K., Bono, G., Moroni, P. G. P., Villanova, S., Nardetto, N., Bresolin, F., Kudritzki, R. P., Storm, J., Gallenne, A., Smolec, R., Minniti, D., Kubiak, M., Szymański, M. K., Poleski, R., Wyrzykowski, Ł., Ulaczyk, K., Pietrukowicz, P., Górski, M., and Karczmarek, P. (2013). *NAT*, 495:76–79.

Pooley, G. (2011). Radio flare in M81. *The Astronomer's Telegram*, 3621.

Ramaty, R. (1969). *ApJ*, 158:753.

Rayner, D. P., Norris, R. P., and Sault, R. J. (2000). *MNRAS*, 319:484–496.

Reid, M. J. and Brunthaler, A. (2004). *ApJ*, 616:872–884.

Reid, M. J. and Brunthaler, A. (2005). The Proper Motion of Sgr A*. volume 340 of *Astronomical Society of the Pacific Conference Series*, page 253.

Reid, M. J., Menten, K. M., Brunthaler, A., Zheng, X. W., Dame, T. M., Xu, Y., Wu, Y., Zhang, B., Sanna, A., Sato, M., Hachisuka, K., Choi, Y. K., Immer, K., Moscadelli, L., Rygl, K. L. J., and Bartkiewicz, A. (2014). Trigonometric Parallaxes of High Mass Star Forming Regions: The Structure and Kinematics of the Milky Way. *ApJ*, 783:130.

Reid, M. J., Readhead, A. C. S., Vermeulen, R. C., and Treuhaft, R. N. (1999). *ApJ*, 524:816–823.

Reuter, H.-P. and Lesch, H. (1996). *A&A*, 310:L5–L8.

Rickett, B. J. (1986). *ApJ*, 307:564–574.

Roberts, J. A. and Komesaroff, M. M. (1965). *Icarus*, 4:127–156.

Ros, E. and Pérez-Torres, M. Á. (2012). *A&A*, 537:A93.

Sandage, A. and Brucato, R. (1979). *AJ*, 84:472–475.

Schödel, R., Krips, M., Markoff, S., Neri, R., and Eckart, A. (2007). *A&A*, 463:551–557.

Scholz, R.-D. and Irwin, M. J. (1994). Absolute Proper Motions of the Dwarf Spheroidal Galaxies in Draco and Ursa Minor. volume 161 of *IAU Symposium*, page 535.

Schweitzer, A. E., Cudworth, K. M., Majewski, S. R., and Suntzeff, N. B. (1995). *AJ*, 110:2747.

Sendlinger, K. (2013). The expansion of supernova 2008iz observed with vlbi. Master's thesis, Max-Planck Institute for Radioastronomy.

Seyfert, C. K. (1943). *ApJ*, 97:28.

Sofue, Y. (1998). *PASJ*, 50:227–231.

Sollima, A., Gil de Paz, A., Martinez-Delgado, D., Gabany, R. J., Gallego-Laborda, J. J., and Hallas, T. (2010). *A&A*, 516:A83.

Spergel, D. N., Verde, L., Peiris, H. V., Komatsu, E., Nolta, M. R., Bennett, C. L., Halpern, M., Hinshaw, G., Jarosik, N., Kogut, A., Limon, M., Meyer, S. S., Page, L., Tucker, G. S., Weiland, J. L., Wollack, E., and Wright, E. L. (2003). *ApJS*, 148:175–194.

Steinmetz, M. (1996). Simulating Galaxy Formation. page 479.

Telesco, C. M., Joy, M., Dietz, K., Decher, R., and Campins, H. (1991). *ApJ*, 369:135–146.

Thompson, A. R. (1999). Fundamentals of Radio Interferometry. volume 180 of *Astronomical Society of the Pacific Conference Series*, page 11.

Thompson, A. R., Moran, J. M., and Swenson, G. W. (1986). *Interferometry and synthesis in radio astronomy*.

van der Marel, R. P., Anderson, J., Bellini, A., Besla, G., Bianchini, P., Boylan-Kolchin, M., Chaname, J., Deason, A., Do, T., Guhathakurta, P., Kallivayalil, N., Lennon, D., Massari, D., Meyer, E., Platais, I., Sabbi, E., Sohn, S. T., Soto, M., Trenti, M., and Watkins, L. (2014). Local Group and Star Cluster Dynamics from HSTPROMO: The Hubble Space Telescope Proper Motion Collaboration. volume 480 of *Astronomical Society of the Pacific Conference Series*, page 43.

van Dyk, S. D., Weiler, K. W., Sramek, R. A., Rupen, M. P., and Panagia, N. (1994). *ApJ*, 432:L115–L118.

van Maanen, A. (1923). *ApJ*, 57:264–278.

Varenius, E., Conway, J. E., Martí-Vidal, I., Beswick, R., Deller, A. T., Wucknitz, O., Jackson, N., Adebahr, B., Pérez-Torres, M. A., Chyży, K. T., Carozzi, T. D., Moldón, J., Aalto, S., Beck, R., Best, P., Dettmar, R.-J., van Driel, W., Brunetti, G., Brüggen, M., Haverkorn, M., Heald, G., Horellou, C., Jarvis, M. J., Morabito, L. K., Miley, G. K., Röttgering, H. J. A., Toribio, M. C., and White, G. J. (2015). *A&A*, 574:A114.

Weiler, K. W., Panagia, N., Montes, M. J., and Sramek, R. A. (2002). *ARA&A*, 40:387–438.

Weiler, K. W., Williams, C. L., Panagia, N., Stockdale, C. J., Kelley, M. T., Sramek, R. A., Van Dyk, S. D., and Marcaide, J. M. (2007). *ApJ*, 671:1959–1980.

Weiß, A., Neininger, N., Hüttemeister, S., and Klein, U. (2001). *A&A*, 365:571–587.

Wilkinson, M. I. and Evans, N. W. (1999). *MNRAS*, 310:645–662.

Wrobel, J. M. (1999). Using the Very Long Baseline Array. volume 31 of *Bulletin of the American Astronomical Society*, page 922.

Yun, M. S. (1999). Tidal Interactions in M81 Group. volume 186 of *IAU Symposium*, page 81.

Yun, M. S., Ho, P. T. P., and Lo, K. Y. (1994). *Nat*, 372:530–532.